HIGH-PERFORMANCE SUPERELASTIC MATERIALS FOR SEISMIC APPLICATIONS

A Thesis

Presented to

the faculty of the School of Engineering and Applied Science

University of Virginia

---

in partial fulfillment
of the requirements for the degree

Master of Science

by

Farzad Shafiei Dizaji

May 2019

APPROVAL SHEET

This Thesis
is submitted in partial fulfillment of the requirements
for the degree of
Master of Science

Author Signature: 

This Thesis has been read and approved by the examining committee:

Advisor: Osman E. Ozbulut

Committee Member: Jose Gomez

Committee Member: Devin K. Harris

Committee Member: _____

Committee Member: _____

Committee Member: _____

Accepted for the School of Engineering and Applied Science:

Craig H. Benson, School of Engineering and Applied Science

May 2019

HIGH PERFORMANCE SUPERELASTIC MATERIALS FOR SEISMIC APPLICATIONS

ABSTRACT

This study proposes a super-elastic memory alloy re-centering damper device and investigates its performance in improving the response of steel frame structures subjected to multi-level seismic hazard. The proposed super-elastic memory alloy re-centering damper (SMARD) count on high performance shape memory alloy (SMA) bars for re-centering capability and employs friction springs to augment its deformation capacity. First of all, this study explores the super-elastic response of NiTiHfPd SMAs under various conditions and illustrates their application into seismic applications. In order to collect experimental data, uniaxial tests are conducted on super-elastic NiTiHfPd SMAs in the temperature range of -55 ºC to +25 ºC, and at the loading frequencies of 0.05 Hz to 1 Hz with four different strain amplitudes. The effects of loading rate and temperature on super-elastic characteristics of NiTiHfPd SMAs are examined. Then, a four-story moment resisting frame with and without supplementary SMA damping elements is designed and modeled. Nonlinear response history analyses are conducted to assess the performance of NiTiHfPd SMAs in mitigating seismic response and limiting residual drifts of steel frames subjected to strong ground motions. The results indicate that the residual story drifts can significantly be reduced when the steel buildings are designed with SMA-bracing systems. It is also found that changing temperature between -35 °C and +25 °C does not affect the performance of NiTiHfPd SMA bracing systems. Additionally, an analytical model of six-story and nine-story steel special moment frame buildings with installed SMARDs in developed to determine the dynamic response of the building. Finally, nonlinear response time history analyses are conducted to assess the behavior of controlled and uncontrolled buildings under 44 ground motion records. Results show that SMARDs can enormously mitigate dynamic response of steel frame structures at different seismic hazard levels and at the same time enhance their post-earthquake functionality.

DEDICATION

To my loving father and mother my sister and my brothers,
for their endless support and words of inspiration

ACKNOWLEDGMENTS

I would like to acknowledge everyone who played a role in my academic accomplishments. First of all, I would like to express my sincere gratitude to my advisor, Dr. Osman Ozbulut, for providing his invaluable guidance, comments and suggestions throughout my study. I appreciate enormously his constant guidance and inspiration for my program. I would like to thank my committee members, Dr. Devin Harris, Dr. Jose Gomez, for their inspiration, support and feedback throughout my study. I also would like to thank Dr. Haluk E. Karaca and his research team from the department of mechanical engineering at The University of Kentucky for providing us with the experimental data. Moreover, I would like to acknowledge the support I received from the Department of Civil and Environmental Engineering in pursuing graduate study at The University of Virginia.

NOMENCLATURE

Abbreviations

AISC	American Institute of Steel Construction
ANSI	American National Standards Institute
ASCE	American Society of Civil Engineers
ASTM	American Society for Testing and Materials
CBF	Concentrically Braced Frames
DBE	Design-based Earthquake
FE	Finite Element
FEMA	Federal Emergency Management Agency
HS	High Strength
HDRB	High Damping Rubber Bearing
LRB	Lead Rubber Bearing
MCE	Maximum Considered Earthquake
MIDR	Maximum Inter-story Drift Ratio
MRDR	Maximum Residual Drift Ratio
MTS	Material Testing System
NEHRP	National Earthquake Hazards Reduction Program
OpenSees	Open System for Earthquake Engineering Simulation
PEER	Pacific Earthquake Engineering Research Center
PFA	Peak Floor Acceleration
PGA	Peak Ground Acceleration
PGV	Peak Ground Velocity
RBS	Reduced Beam Section

RHD	Reusable Hysteric Damper
RSMAD	Re-centering Shape Memory Alloy Damper
SC-BRB	Self-centering Buckling-restrained Brace
SDC	Seismic Design Category
SFDB	Self-centering Friction Damping Brace
SE	Superelasticity
SEI	Structural Engineering Institute
SMA	Shape Memory Alloy
SMA-LRB	SMA-based Lead Rubber Bearing
SMARB	SMA Supplemented Rubber Bearing
SME	Shape Memory Effect
SMRF	Special Moment Resisting Frame
SRB	SMA-based Rubber Bearing
SSMAFD	Superelastic Shape Memory Alloy Friction Damper
SMARD	Superelastic Memory Alloy Re-centering Damper
SVD	Superelastic Viscous Damper

Symbols

δ	Design Displacement
γ	Ratio of Post-transformation Hardening Stiffness to Initial Stiffness
A_f	Austenite Finish Temperature
Al	Aluminum
A_s	Austenite Start Temperature
Be	Beryllium
Cu	Copper
D_{max}	Maximum Cyclic Displacements
D_{min}	Minimum Cyclic Displacements

E_D	Energy Dissipated per Cycle
E_S	Maximum Strain Energy for the Same Cycle
F_a	Forward Activation Force
Fe	Iron
F_{max}	Maximum Forces
F_{min}	Minimum Forces
FNCATB	Fe-Ni-Co-Al-Ta-B
kJ	Kilo Jule
K	Elastic Spring Coefficient
k_1	Initial Stiffness
k_2	Post-activation Stiffness
k_s	Equivalent Stiffness
M_d	Austenite Stabilization Temperature
M_f	Martensite Finish Temperature
M_L	Local Magnitude
Mn	Manganese
M_s	Martensite Start Temperature
M_w	Moment Magnitude
MPa	Mega Pascal
Nb	Niobium
Ni	Nickel
NiTi	Nickel Titanium
NiTiHfPd	Nickel Titanium Hafnuim Palladium
Pd	Palladium
Hf	Haffnium
$S_a (T_1)$	Spectral Acceleration at the Fundamental Period
Si	Silicon
T	Temperature
Ta	Tantalum
Ti	Titanium
Zn	Zinc

β	Ratio of Forward to Reverse Activation Force
σ	Stress
ε	Strain

Table of Contents

LIST OF TABLES

LIST OF FIGURES

1 Introduction

1.1 Background and Motivation

To mitigate the adverse effects of dynamic environmental hazards such as earthquakes, strong winds, and hurricanes and to achieve a more resilient design under dynamic loads, various passive, active and semi-active control devices have been proposed and developed [1]. The most widely tested and commonly implemented strategies have been passive devices as they are reliable, require no external power, and never destabilize the structure. However, designing buildings with passive systems to provide performance improvement over all ranges of earthquake and wind excitation is a challenging task.

A number of passive energy dissipation systems have been developed to mitigate damaging effects of natural hazards on structures [2]. Passive energy dissipation devices can be grouped into two main categories: hysteretic devices and rate-dependent devices. Examples of hysteretic devices include metallic yielding devices and friction devices. Energy dissipation in hysteretic devices depends primarily on relative displacements within the device. These devices add initial stiffness until yielding or slip occurs and provide hysteretic energy dissipation. However, they do not provide sufficient damping at small vibrations caused by wind excitation or frequent seismic events while increase the forces and accelerations on the structure due to high stiffness. Furthermore, metallic devices usually have a limited number of working cycles and may require replacement after a strong event and friction devices may lead to permanent deformations if no restoring force mechanism is provided. Examples of rate-dependent devices include fluid viscous dampers and viscoelastic dampers. The energy dissipation capacity of these devices depends on the velocity across the device [2]. The viscous damper can provide high force and damping capabilities while the viscoelastic dampers have low force and displacement capacity. In general, rate-dependent devices can dissipate energy at all magnitudes of motion but do not possess the same capacity for energy dissipation as hysteretic devices [3]. Note that these devices also do not have self-centering property to return the structure to its original position.

Numerous efforts have been carried out to develop new structural systems that can provide stable energy dissipation with full self-centering capabilities [4]. Due to its inherent and excellent re-centering ability, high corrosion and fatigue resistance, several researchers have proposed shape memory alloy (SMA)-based seismic protection systems including, but not limited to, SMA-based

bracing systems [5-7]; SMA-based dampers [8-11]; and SMA-based isolation systems [12-16]. Among various SMA compositions, the NiTi alloy has been the most widely studied material for SMA-based dampers. Since NiTi SMAs does not have sufficient energy dissipation capacity to render the use of SMAs as the sole damping device, damping in those devices was supplemented through pre-tensioning SMA elements [17], incorporating a frictional device [18-20], energy absorbing steel struts [21], viscoelastic device [22-23], or buckling-restrained braces [24].

A recently developed class of SMAs that consists of NiTiHfPd provides large energy dissipation and high stresses [25] and can overcome the deficiency of currently available SMAs. Figure 1-1 presents typical strain-stress diagrams of NiTi and NiTiHfPd SMAs at room temperature. It can be seen that the area captured within the hysteresis loop, which signifies the dissipated energy, for NiTiHfPd is considerably larger than that of NiTi. The strength of NiTiHfPd is also significantly higher than that of NiTi. Thus, the required cross-sectional area of the SMA elements to develop the design force of a damping device will be considerably smaller for NiTiHfPd. A chevron configuration bracing system as well as a vibration control device based on NiTiHfPd will avoid employing additional energy dissipation unit and/or requiring large quantities of material due to high energy dissipation capabilities and strength of NiTiHfPd. This study discusses experimental characterization of NiTiHfPd SMAs, friction springs and conceptual design of a simple but efficient NiTiHfPd SMA-based energy dissipating and re-centering device, which avoids extra fabrication and material costs.

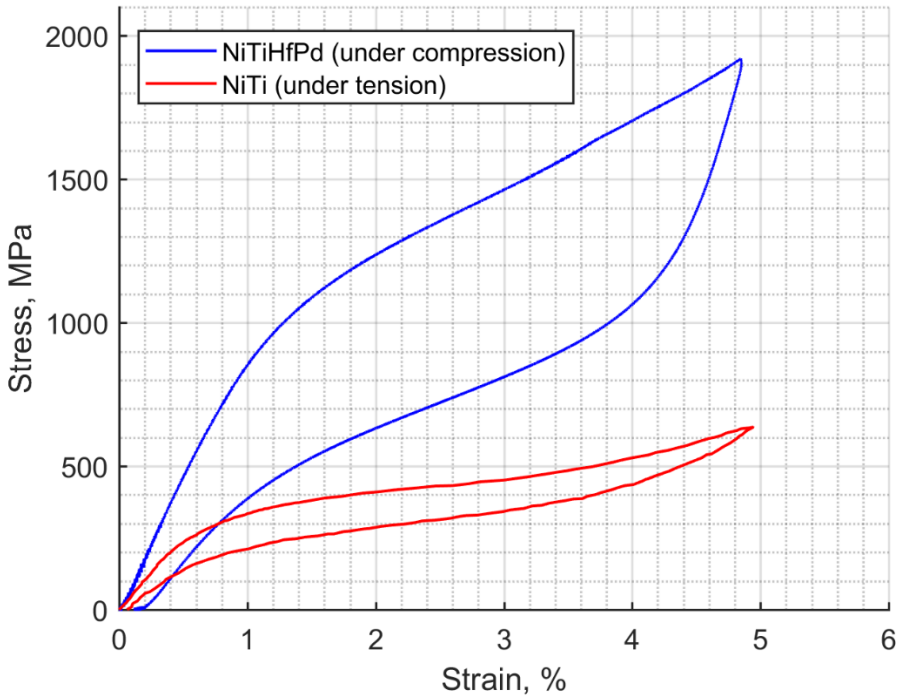

Figure 1-1 Strain-stress diagrams for NiTi and NiTiHfPd at room temperature and loading frequency of 1.0 Hz

1.2 Research Objectives

The goal of this research work is first to investigate a new SMA material, namely NiTiHfPd alloy, and its applications in seismic protection systems. The performance of NiTiHfPd SMAs in mitigating seismic response and limiting residual drifts of steel frames as chevron configuration in bracing systems subjected to strong ground motions is assessed. Moreover, the objective of this study is to investigate design and characterize a passive structural control device, and evaluate its performance under multi-level seismic hazards. The device, named the superelastic memory alloy re-centering damper (SMARD), combines the energy-dissipating and re-centering capacity of friction spring with the excellent re-centering properties of SMA bars in a single device that demonstrates an improved response. The advantageous attributes of the proposed device include very high force capacity; large deformation capacity; excellent re-centering ability; ultra-high damping capacity; passive nature; and need for no special maintenance or replacement throughout the life-cycle.

1.3 Thesis organization

A chapter-by-chapter overview of this thesis is provided as follows:

Chapter 1 introduces the motivation for this study, describes the research objectives as well as the organization of the thesis.

Chapter 2 presents an overview of shape memory alloys especially new SMA material named as NiTiHfPd and a review of the application of SMAs into civil structures germane to this study.

Chapter 3 includes compression experimental test results are conducted to evaluate the effects of temperature, strain rate, and strain amplitude on mechanical behavior of superelastic NiTiHfPd. Also, experimental test results are performed to discover the properties of the friction springs. Furthermore, OpenSees simulations are run in order to find their proper parameters for future analytical simulations.

Chapter 4 illustrates the performance of the four story building using NiTiHfPd SMA bracing systems as well as the effect of the temperatures on the behavior of the four story building.

Chapter 5 explores the effectiveness of the proposed passive structural control device in designing two steel frame buildings under multi-level earthquake events.

Chapter 6 discusses the main conclusions and makes some recommendations for further research.

2 Literature review

2.1 Introduction

Over the past two decades, the development of material in conjunction with the progress of adaptive and intelligent structure systems has received increasing attention among structural engineers. Shape memory alloys (SMAs) are a class of smart materials that can exhibit a stable flag-shaped hysteretic behavior. They have been studied as promising materials to develop innovative devices and systems in structural engineering. Although nickel-titanium alloys were discovered initially in the 1960s and commercialized under the trade name Nitinol, the first use of SMAs in structural applications was initiated in the early 1990s as a new material for seismic isolation devices [26]. Since then, countless researchers have carried out extensive investigations to explore the implementation of SMA-based systems for different structural applications. Shape memory alloys (SMAs) have emerged as a smart material that can be used in passive vibration control devices for energy dissipating and re-centering purposes. However, the quantity of equivalent viscous damping provided by superelastic NiTi SMA wires or bars is not sufficient to render the use of SMAs as the sole damping device implemented in a tall structure subjected to severe dynamic loadings. A recently developed class of SMAs that consists of NiTiHfPd provides large energy dissipation and high stresses [25] and can overcome the deficiency of currently available SMAs. This section intend in providing a comprehensive review of shape memory alloys and the application of SMA-based devices, highlighting their characteristics, mechanical behavior, and the structural application of shape memory alloys in civil engineering.

2.2 Shape memory alloy characteristics

2.2.1 SMA Summarization

Shape Memory Alloy (SMA) is an alloy that exhibits very distinctive behavior when it is deformed and then heated. SMAs belong to a class of shape memory materials (SMMs), which have the ability to ‘memorise’ or retain their previous form when subjected to certain stimulus such as thermomechanical or magnetic variations. SMAs have drawn significant attention and interest in recent years in a broad range of commercial applications, due to their unique and superior properties; this commercial development has been supported by fundamental and applied research studies.

SMAs have beneficial characteristics for various fields, especially structural application, to modify the performance of structures, owing to their unique properties. SMAs have the ability to recover large shape changes by the application of stress, temperature, or magnetic field [27-29]. Superelasticity (SE) and shape memory effect (SME) are the two unique phenomena of SMAs where large shape changes could occur through stress and temperature cycling, respectively [30-31]. These marvelous properties are associated to phase transformations in crystal structures of SMA materials. The force required in these transformations can be either temperature-induced (shape memory effect) or stress-induced (superelasticity). The vital crystal structures of SMAs are distinguished by their dual-phase microstructure: the austenite phase and the martensite phase. These beneficial characteristic and reduction in cost over the last decade of SMA production have attracted the attention of countless researchers in scientific communities interested in developing seismic protection devices based on these properties. A large number of alloys have been investigated for shape-memory behavior. Compared to Fe-based and Cu-based SMAs, NiTi alloys have received the most interest because of their excellent physical and mechanical properties, which include good fatigue life, oxidation and corrosion resistance, high ductility, and strain [32, 44]. However, NiTi alloys have some drawbacks such as low transformation temperatures (TTs) (<100 °C) and low strength [32, 45]. A new type of SMA material were studied in order to address drawbacks of NiTi named as NiTiHfPd [46-47]. Therefore, the development of the new SMA materials can contribute to the extensive application of shape memory alloys in structural applications due to the benefits of significant cost savings and unique adaptive characteristics.

2.2.2 SMA Microstructure

The SMA microstructure exists in two stable phases, which have different crystal structures. The austenite phase is stable at high temperature and low stress with a body-centric atomic structure, while the martensite phase is stable at low temperatures and high stress with a parallelogram structure. The martensite structure can change its position by moving twin boundaries, while the austenite structure deforms by generation of dislocation. Consequently, the martensite phase is weaker and provides lower yield strength than that of the austenite phase. The unique properties of SMAs are related to phase transformations between two distinct ordered atomic structures. In addition, the martensite can exist in either of two crystal structures: twinned and de-twinned.

Figure 2-1 illustrates different phases of shape memory alloy microstructure in 2D representation. The driving force for solid-to-solid phase transformations between these two phases can be induced either thermally or mechanically. The key effects of phase transformations between the austenite and the martensite assist in explaining the two fundamental characteristics of SMAs: superelasticity and the shape memory effect. These two behaviors depend on the four characteristic temperatures at which phase transformation occurs.

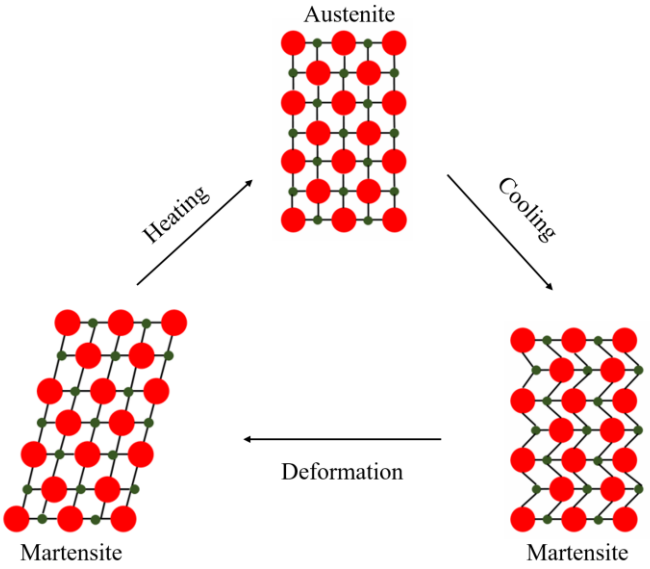

Figure 2-1 Illustration of different phase transformations of the SMA in the Shape Memory Effect cycle Bottom left corner depicts the detwinned martensite and the bottom right depicts the twinned martensite

In the stress-free state, the phase transformations of SMA materials can occur at four characteristic temperatures: (i) the austenite start temperature *As*, where the material starts to transform from twinned martensite to austenite, (ii) austenite finish temperature *Af*, where the material is completely transformed to austenite, (iii) martensite start temperature *Ms*, where austenite begins to transform into twinned martensite, (iv) martensite finish temperature *Mf*, where the transformation to martensite is completed.

2.2.3 Shape memory effect

Shape memory effect is a promising characteristic of SMAs that occurs when the material is deformed below *Mf*, recovering its original shape after being deformed through a thermal heating up to above *Af*. Figure 2-3 illustrates the shape memory effect in relation to the temperature and

deformation variation. In their low-temperature phase ($T < Mf$), the SMAs show a phenomenon to indicate the shape memory effect, illustrating the build-up of residual stress fields.

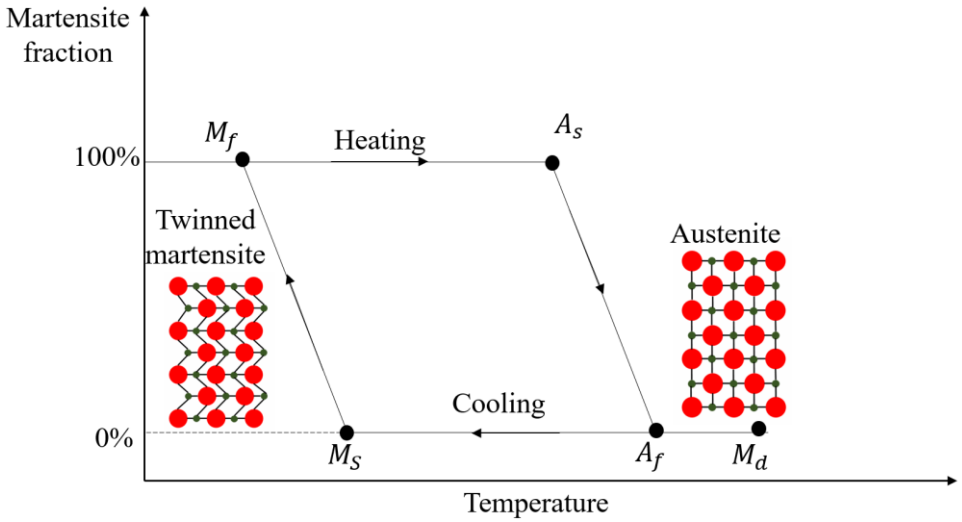

Figure 2-2 SMA microstructure representation of shape memory effect and superelasticity

When SMA is cooled from its parent phase austenitic to the temperature below *Mf*, the SMA exhibits its twinned martensite phase through self-accommodation. This twined martensite phase can be easily changed by the application of external stress. After the application of external stress to the twinned martensite phase, SMA material reorients into the detwinned martensite phase in order to accommodate the resulting strain, if the applied stress is above the critical level. During the detwinning process of the martensite crystal structure, the stress remains almost constant until the material reaches the complete detwinned phase. Upon the release of the stress, the detwinned structure of the material remains in its deformed position. When the deformed material is heated to a temperature above *Af*, the reverse phase transformation from the martensite to the austenite can occur and the material can regain its initial position, indicating complete shape recovery. Finally, the cooling of the SMA material causes the austenite crystal structure to transform into the low symmetry twinned orientation. This process is commonly known as the shape memory effect. This phenomenon can be better displayed in the combined stress-strain temperature diagram as shown in Figure 2-4.

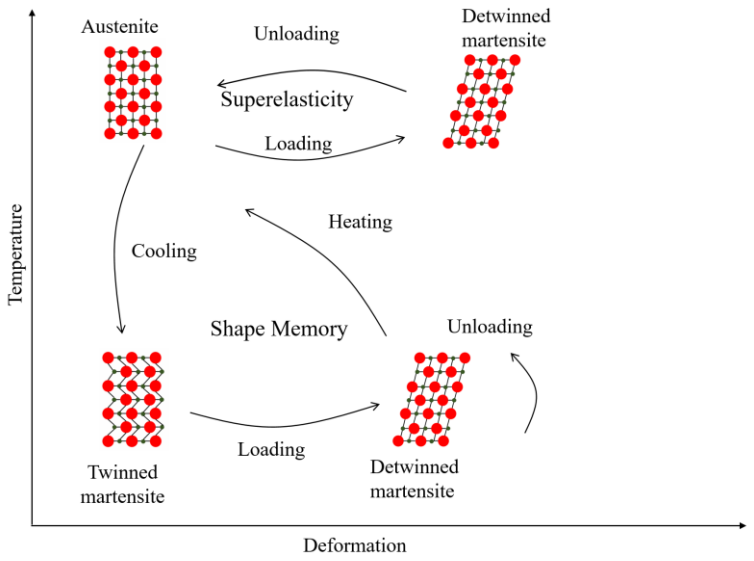

Figure 2-3 Temperature and deformation relationship of SMA microstructure for shape memory effect and superelasticity

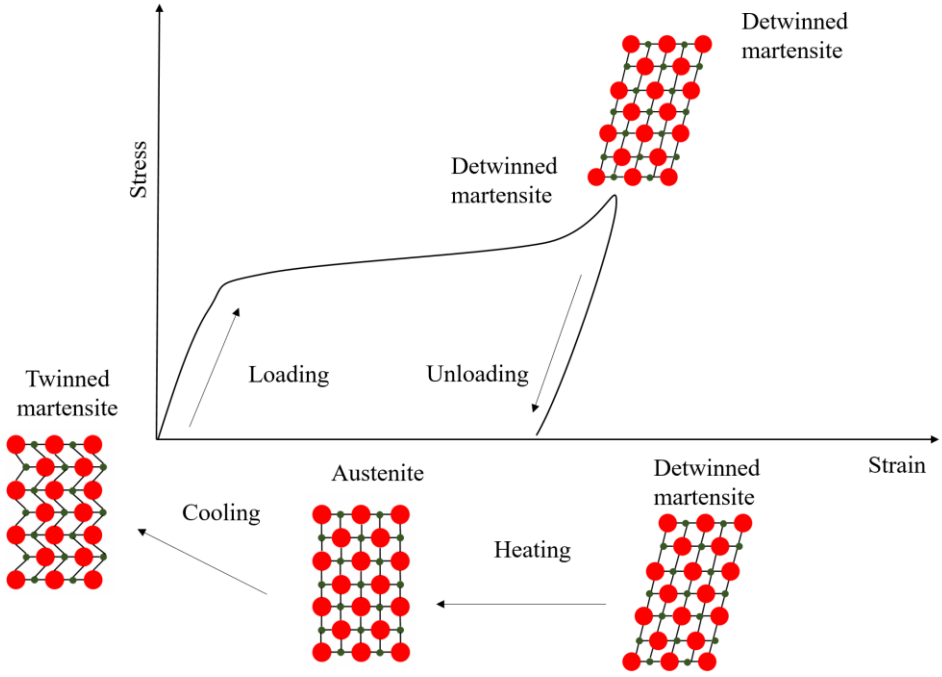

Figure 2-4 Stress-strain relationship for shape memory effect

2.2.4 Superelastic effect

When a unidirectional stress is applied to an austenitic specimen (Figure 2-5) at a temperature greater than *Af*, there is a critical value whereupon a transformation from austenitic to detwinned martensite occurs. As deformation proceeds in isothermal condition, the stress remains almost constant until the material in fully transformed. Further straining causes the elastic loading of the

detwinned martensite. Upon unloading, since martensite is unstable without stress at temperature greater than *Af*, a reverse transformation takes place, but at a lower stress level than during loading so that a hysteretic effect is produced. If the material temperature is greater than *Af*, the strain attained during loading is completely and spontaneously recovered at the end of the unloading. This remarkable process gives rise to an energy absorption capacity with zero residual strain, which is termed superelasticity (or pseudo elasticity). If the material temperature is less than *Af*, only a part of stress-induced martensite re-transforms into austenitic. A residual strain is then found at the end of unloading, which can be recovered by heating above *Af*. This phenomenon is generally referred to as partial superelasticity. Figure 2-5 shows a typical superelastic stress-strain response of SMAs. The superelastic thermo-mechanical behavior starts from temperatures above austenite finish temperature (Af) where the material is fully austenite (point A) and continues in loading by an applied force to make the detwinned martensite crystal form (point B). During this (forward) transformation from austenite to martensite the transformation strain is generated. Upon unloading, the generated strain is fully recovered in the (backward) transformation and the original form is achieved (point C). The stress-temperature-crystalline structure cycle of such behavior is shown on the transformation plot in Figure 2-6.

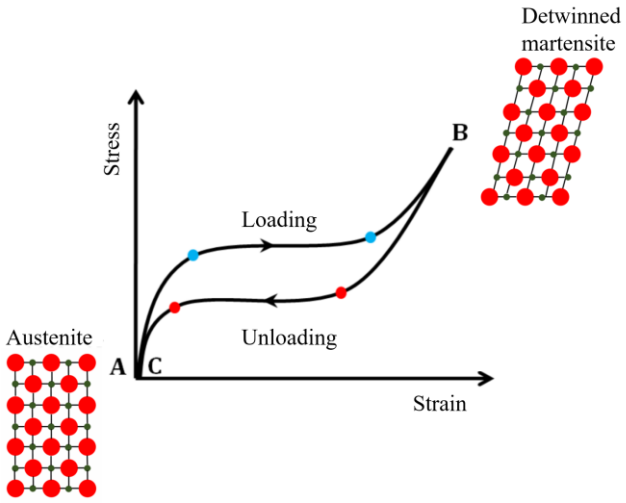

Figure 2-5 Stress-strain relationship for superelastic SMAs

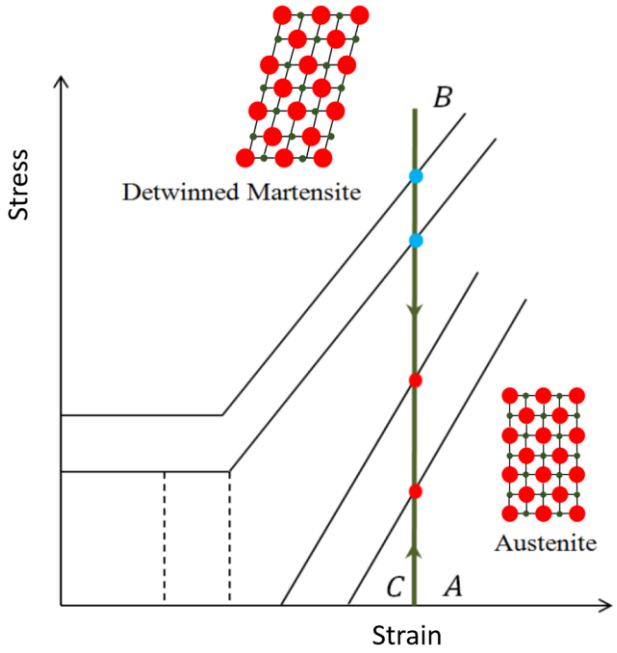

Figure 2-6 Superelasticity in phase diagram

2.2.5 Shape memory alloy compositions

Nowadays, a vast range of SMA compositions has been developed and investigated to improve the characteristics of SMAs and the performance of structures in various engineering applications. The NiTi-based alloys have been the most commonly used and commercially available SMAs due to their superior thermo-mechanical properties, reliability, biocompatibility, and excellent strain recovery. In order to reduce the cost of SMA materials, researchers have developed different compositions of SMAs. The three paramount types of SMA systems that have been most explored over the last two decades are NiTi-based, copper *(*Cu*)*-based, and iron (Fe)-based SMAs. Recently, NiTiHfPd SMAs that possess ultra-high strength and superior superelasticity have been developed [46-47].

2.2.5.1 NiTi based SMAs

Since NiTi shape memory alloys (SMAs) present unique super-elasticity and shape memory effect and good biological compatibility and wear resistance, they have been widely used in the areas of aeronautic, civil, microelectronic, and biomedical engineering. The nickel titanium (NiTi) alloys,

alternatively recognized as Nitinol, have been extensively investigated and employed in different engineering applications, due to such strategic properties as large recovery strain, excellent superelasticity, and superior corrosion resistance. Three major advantages of NiTi SMAs are high stress capacity up to 700 MPa, recoverable stress of about 90% of the yield strength, and a large recovery strain of about 6-8%. The distinct characteristics of NiTi derive from the presence of an almost equiatomic composition of nickel and titanium: 49-51 atomic % of Ni to avoid undesirable phase transformation and decreasing transformation temperature. By adjusting their composition, NiTi alloys can be used in engineering structures for superelastic, shape memory, and damping applications at the ambient temperatures.

2.2.5.2 Copper based SMAs

In an effort to lower the cost of SMAs, numerous researchers have explored to produce Cu-based SMAs for engineering applications. Although Cu-based SMAs cannot provide excellent shape memory properties like NiTi SMAs, they have lower production costs and are easier to fabricate. Since Cu-based SMA systems can be easily produced utilizing liquid metallurgy and power metallurgy routs, they are cost-effective. In addition, the Cu-based SMAs exhibit lower strain rate effects and have larger operating temperature ranges compared to NiTi SMAs [48]. The Cu-based SMAs usually have lower recoverable strain and lower transformation stress than NiTi SMAs. The main Cu-based SMAs include the binary alloys Cu-Zn and Cu-Al. In these alloys, a third alloying element can be introduced to produce Cu-based SMAs with desirable transformation temperature or microstructure. Several compositions of Cu-based SMAs have been developed, such as Cu-Zn-Al, Cu-Al-Be, and Cu-Al-Mn.

2.2.5.3 Iron based SMAs

The Fe-based SMAs are recognized as the third predominant studied group of SMAs. These SMAs are also called shape memory steel (SMS) and include Fe-Pd, Fe-Mn-Si, Fe-Mn-Al, Fe-Ni-C, and Fe-Ni-Co-Ti. These SMA compositions have been produced in an attempt to lower the cost and study their suitability for large-scale engineering applications. For example, a Fe-Ni-Co-Al-Ta-B SMA indicating superelastic strain of about 13% and very high tensile stress is introduced [49].

Similarly, Omori et al. (2011) developed Fe-Mn-Al-Ni showing superelastic strain over 6%, which revealed good superelastic behavior at room temperature. Because these Fe-based SMAs have been developed to conduct laboratory testing for research only, they have not yet been made commercially available.

2.2.5.4 NiTiHfPd based SMAs

NiTi SMAs have been studied and employed in a variety of applications due to their superior shape memory properties, corrosion resistance, biocompatibility, ductility, etc. However, they have certain limitations that restrict their functionality for some applications. Alloying is one of the most effective ways to engineer properties and overcome these problems. For instance, an SMA material with good damping capacity needs to have large mechanical hysteresis and transformation strain at high-stress levels to be employed as dampers. While the mechanical hysteresis and damping capacity of binary NiTi alloys has been reported to be 200-400 MPa and 16 $J.cm^{-3}$ respectively [50], with the addition of Nb it can be increased to 500-600 MPa and 38 $J.cm^{-3}$ [49]. The addition of elements like Zr, Hf, and Pd also has been studied to improve strength, wear resistance and damping capacity of SMAs. Due to its low cost, medium ductility and higher work output, the addition of Hf to NiTi binary found to be the promising [51-52]. Single crystalline NiTiHfPd alloy has been reported to show huge mechanical hysteresis of up to 1270MPa, superelastic response under extremely high-stress levels (2.5GPa), and damping capacity of 44 J cm^{-3} [25, 53] Even polycrystalline NiTiHfPd alloys can generate high work outputs of 32-35 J cm^{-3} (up to 120 ºC), which are considerably higher than NiTi and Ni. The ultra-high-strength, and the exceptional damping capacity and practical ability to demonstrate superelastic behavior at room temperature makes NiTiHfPd SMAs a promising candidate for applications that require high damping demand.

2.2.5.5 Comparison of different compositions in SMAs

The comparison of the modulus of elasticity and recovery strain of three SMA systems is enlightened in Figure 2-7 (a-b). It can be seen that Cu-based SMAs have lower modulus of elasticity compared to the other two SMA systems. The Fe-Ni-Co-Al-Ta-B SMAs show very high recovery strain, while Fe-Mn-Al-Ni exhibits the relatively high modulus of elasticity. Also, the

comparison of different types of NiTi based alloys is shown in Figure 2-7. What's more, In Figure 2-7(c), the maximum work output levels of various NiTi-based SMA are shown as a function of their typical operating temperature range. It is observed that NiTiHfPd alloys can generate higher work outputs of 32-35 J cm^{-3} (up to 120 °C) compared with other NiTi-based SMA, though upper temperature capability is somewhat limited. Table 2-1 also summarizes the comparative advantages of three major SMA systems: NiTi-based, Cu-based, and Fe-based SMA.

Beside the high work output, NiTiHfPd polycrystals have considerable damping capacity, which in simple terms is the ability to repeatedly disperse unwanted energy from a system. Damping capacity is related to the mechanical hysteresis and transformation strain and can be determined by calculating the area between the forward and reverse transformations in the superelastic stress–strain curves, as depicted schematically in Figure 2-8(a).

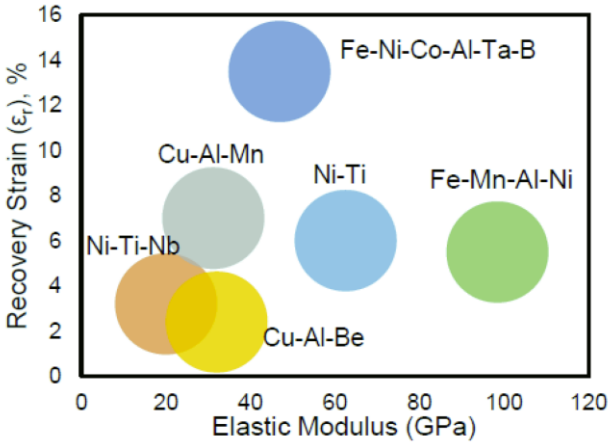

(a)

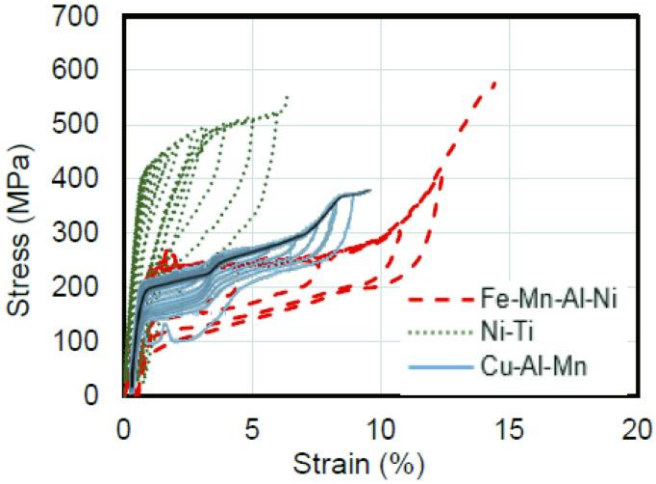

(b)

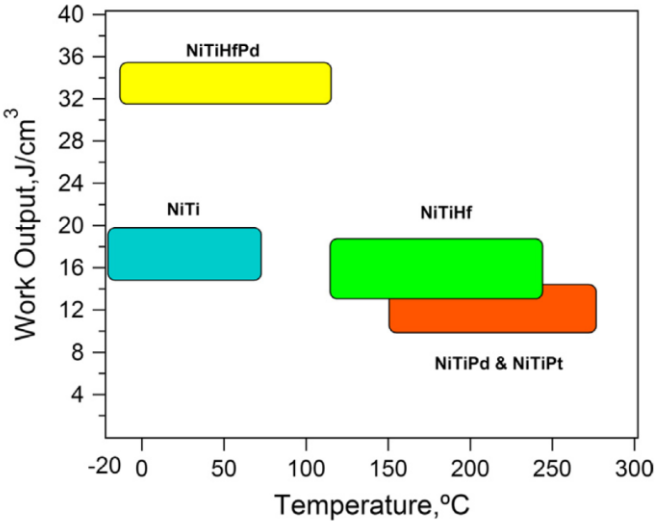

(c)

Figure 2-7 (a) Comparison of elastic modulus and recovery strain, (b) comparison of hysteretic response of different SMAs [54] and (c) A comparison of work outputs for typical NiTi-based SMA [46].

High hysteresis and high transformation strain result in more energy dissipation from a system. Damping capacities of selected NiTi based alloys are compared in Figure 2-8 (b) as a function of operating stress levels (critical stress for forward transformation).

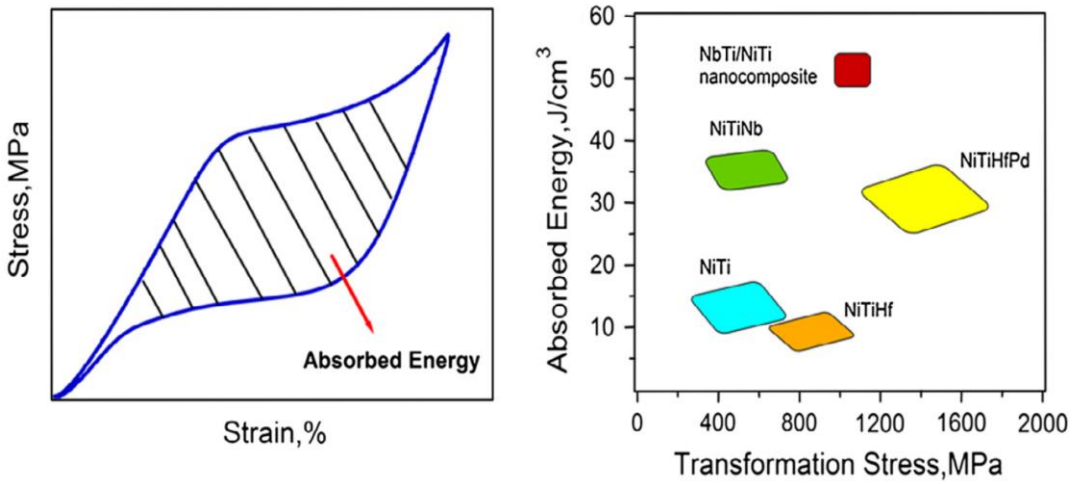

(a) (b)

Figure 2-8 (a) Calculation of the absorbed energy during a superelastic stress–strain cycle. (b) Damping capacity as a function transformation stress for various NiTi-based SMA [46]

The high damping capacity (30-34 J cm^{-3}) of the present alloy stems from its outstanding mechanical hysteresis and good superelastic strain, approaching 4% (Figure 2-9). In addition to damping applications, dissipation mechanisms due to the martensitic transformation allow SMA to be used in applications that require wear resistance [55]. In particular, properties such as high strength, high hardness, corrosion resistance and the ability to be used with conventional lubricants [56], combined with this superb damping capacity and wear resistance, open these types of materials to vast variety of applications.

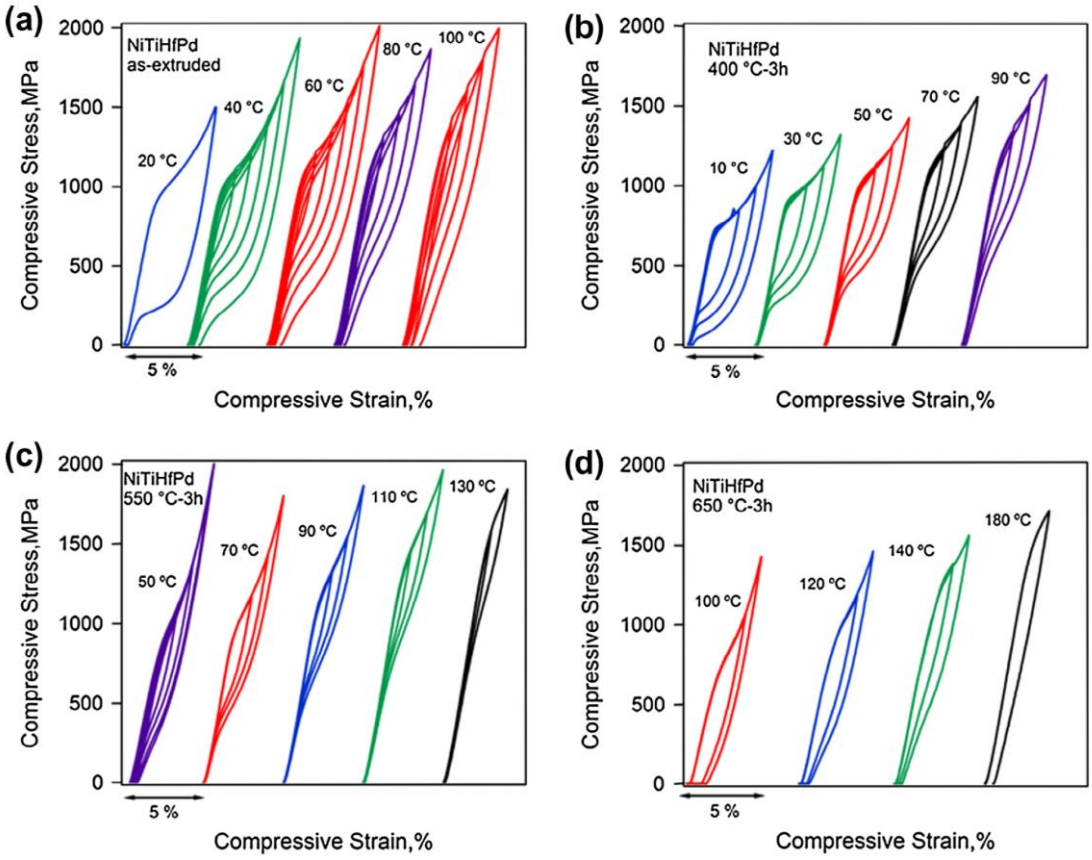

Figure 2-9 Isothermal stress–strain curves for polycrystalline NiTiHfPd: (a) as-extruded, (b) aged at 400 °C for 3 h, (c) aged at 550 °C for 3 h, and (d) aged at 650 °C for 3 h demonstrating superelastic behavior [46]

Table 2-1 Comparative advantages of three shape memory alloy compositions

Property	NiTi-based	Cu-based	Fe-based
Modulus of Elasticity	Moderate	Low	High
Shape memory effect	High	Moderate	Low
Maximum recoverable strain	8%	5%	<5%
Production cost	High	Low	Low
Fabrication	Low	Good	Moderate
Workability	Moderate	Low	Good
Processing	Demanding	Easy	Easy

2.3 Mechanical Behavior of NiTi based Shape Memory Alloys

Since most of the seismic applications of SMAs rely on the superelastic effect of the SMAs, the mechanical properties of the superelastic SMAs are discussed in this section. The sensitivity of these properties to various factors such as temperature, strain rate, cyclic loading, and thermomechanical treatment is also examined. The superelastic SMAs that are considered for civil engineering applications includes the NiTi alloy and the Cu-based alloys. In past decades, many research studies have investigated the mechanical behavior of superelastic NiTi SMAs through experimental testing. The following subsections provide the review of the influence of cyclic loading, strain rate, and temperature on the hysteretic behavior of the NiTi SMAs, in addition to the general characteristics of NiTi SMAs.

2.3.1 General Characteristics of NiTi based SMAs

NiTiHfPd shape memory alloys have appealing mechanical characteristics such as considerable energy dissipation capacity, excellent re-centering ability, high strength, good fatigue resistance and high corrosion resistance. However, there are a number of parameters that influence the mechanical properties of the NiTiHfPd SMAs. Therefore, a complete understanding of the mechanical behavior of the NiTiHfPd is required before employing it in seismic applications. A number of researchers have conducted experimental testing to explore the mechanical behavior of NiTi SMAs in different shapes and forms, such as bars, wires, or cables. However, there have been more studies on SMA wires than any other form of SMAs. That can be attributed to the easier

manufacturing process and lower cost of SMA wires. In addition, most of the previous studies indicated that the SMA wires have better superelastic characteristics compared to SMA bars. Some researchers investigated the cyclic behavior of both SMA bars and wires [57-59]. They revealed that SMA wires and bars with a variation in diameter from 1.8 mm to 25.4 mm exhibited satisfactory re-centering capabilities; however, SMA wires showed higher strength and damping capacity compared to the larger SMA bars. Other researchers demonstrated that both bars and wires can provide good superelastic properties by adopting suitable chemical composition, deformation processing, and heat treatment [60-61]. Damping capacity represents the ability of a material to absorb or release the vibrational energy of a structure by converting the mechanical energy into heat energy. The damping capacity of SMAs is related to the hysteretic movement of the martensite variant interfaces [62-64]. The equivalent viscous damping ratio of SMA material can be calculated as a function of cyclic strain level. One study investigating the damping capacity of SMA materials reported that the equivalent viscous damping attained its maximum value at 4-5% strain level and decreased after that strain level [59].The study also indicated that the equivalent viscous damping of SMAs wires is higher compared to SMA bars, with a damping ratio of 4-8% for wires and 2-4% for bars. Furthermore, the results showed that the damping capacity is inversely proportional to the bar diameter: the lower the bar diameter, the higher its damping capacity. In another study of the superelastic NiTi bar and wires, the NiTi wires demonstrated a higher equivalent viscous damping of 5.3% for the 0.254 mm diameter wires, while the NiTi bars of 12.7 mm diameter showed a 2.7% equivalent viscous damping under the quasi-static tension loading [65]. In another study, it was reported that the equivalent viscous damping of a 12.7 mm diameter SMA bar was approximately 30% higher than that of a 19.1 mm diameter bar [61]. It was also shown that residual displacements slightly increased with larger diameter SMA bars. New SMA bar exposes higher equivalent viscous damping compare to NiTi bars and wires which made it to be more considered in structural applications. A few research have carried out to investigate he mechanical characteristics of superelastic NiTiHfPd SMAs. The following discussion outlines the effects of cyclic loading, strain-rate and temperature on the behavior of the NiTiHfPd SMA.

2.3.1.1 Cyclic loading of NiTi based SMAs

Earthquake events induce cyclic deformations. To comprehend the cyclic behavior of NiTi SMAs under seismic events, numerous researchers have conducted experimental tests to characterize the cyclic behavior of SMAs under repeated cyclic loading with incremental strain levels. In order to investigate the influence of repeated loading and fatigue, some researchers have tested superelastic SMA bars and wires under cyclic loading conditions. The test results showed that the residual strain increases while the loading plateau stress level and hysteric loops decrease with an increasing number of loading cycles [57, 59, 66]. After recognizing the variations in the forward phase transformation stress level, some researchers investigated the influence of training cycles on NiTi elements to achieve stabilization in the hysteric behavior. Particularly, applying training loading cycles (approximately 20 cycles) on NiTi elements provides a stable flag-shaped hysteric behavior with enhanced re-centering capabilities [58,65,67]. Interestingly, the maximum variation on the cyclic behavior was observed between the first and second cycles, which was caused by small levels of localized slip [59]. Figure 2-10 displays the cyclic tensile test result of NiTi wires having 2 mm diameter, indicating the stress-strain curve with the variation in cyclic behavior in forward transformation [68].

An experimental test results of the large-diameter NiTi bars of 12.7, 19.1, and 31.8 mm, is presented by [61] while another researcher demonstrated the real-scale test results of large size superelastic SMA bars with diameter varying from 8 mm to 30 mm [69]. Similarly, another researcher reported the cyclic properties of superelastic SMA bars and wires having varying sizes, from 1.8 mm wires to 25.4 mm diameter, to demonstrate the influence of bar size and loading history on the behavior and properties of superelastic SMAs [59]. Furthermore, other researches also reported the fundamental cyclic behavior of superelastic NiTi wires [70-72]. These test results showed that the hysteresis loops of both SMA wires and bars experience similar degradation under cyclic load.

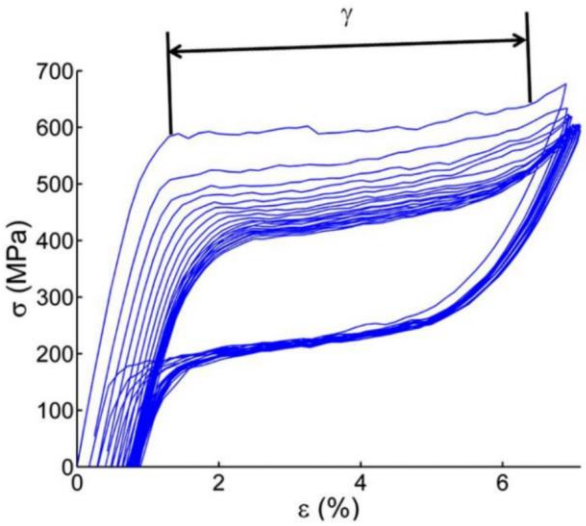

Figure 2-10 Results of cyclic tensile tests on NiTi wires [68]

Recently, researchers have reported experimental test results of NiTiHfPd SMA bars, relatively new structural elements that demonstrate numerous desirable qualities, superior performance than those of large-section NiTi bars, NiTi cables and adaptive functionality. Additionally, NiTiHfPd SMA bars generally exhibit many of the advantages of classical wire cables and leverage the excellent mechanical properties of thin SMA wires in developing large force tension elements. By adopting the recently developed, highly optimized manufacturing process for NiTiHfPd bars, SMA bars can expedite the application of SMAs in infrastructure applications due to their superior mechanical properties, large force capacities, and maybe lower cost over SMA bars. Figure 2-11 shows the hysteric cyclic behavior of a single NiTiHfPd bars exhibiting a restoring stress and very good re-centering capability after 3 cycles up to 6% strain.

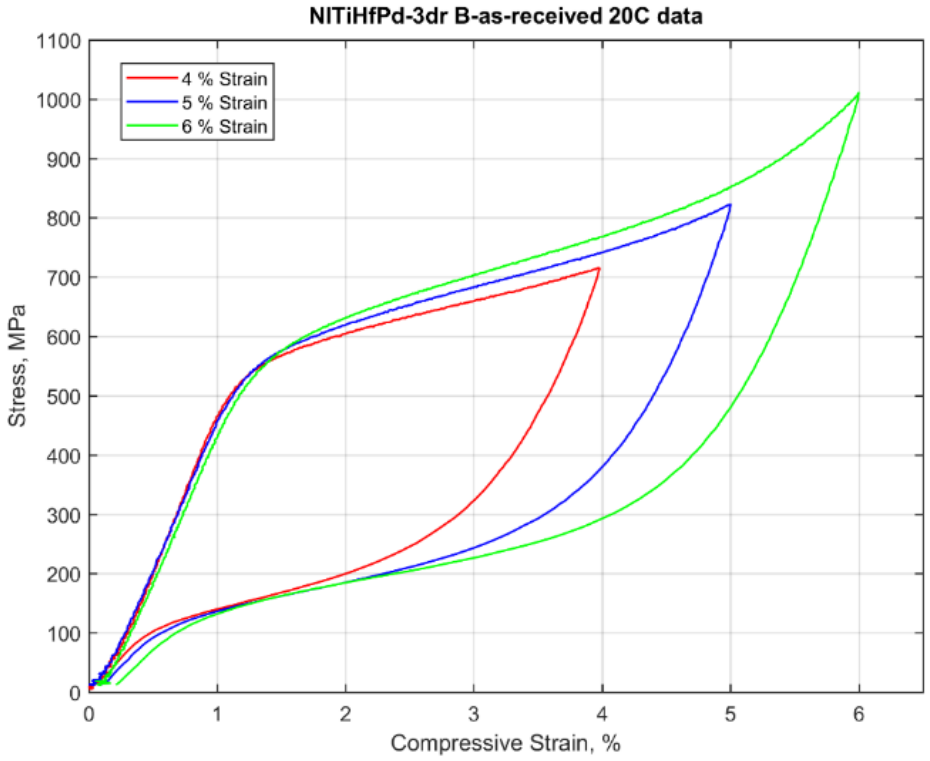

Figure 2-11 Hysteresis cycles of stress-strain curves for a single NiTiHfPd bar

2.3.1.2 Influence of strain rate

SMAs will be subjected to high loading rates if they are used in dynamic applications. In this subsection, the effects of the loading rate on the material behavior are investigated. Figure 2-12 illustrates the compression stress–strain curves of aged NiTiHfPd under the selected loading frequencies at various strain amplitudes and at selected temperature. It can be seen that an increase in loading rate does not affect significantly the forward transformation path, whereas it somewhat increases the reverse transformation stresses. At higher loading rates, the latent heat released during loading did not have enough time to transfer out completely. This leads to a higher temperature in the specimen at the start of unloading, and in return, an increase in the reverse transformation stresses. Therefore, the unloading path moves upward and the hysteresis loop narrows as the frequency increases.

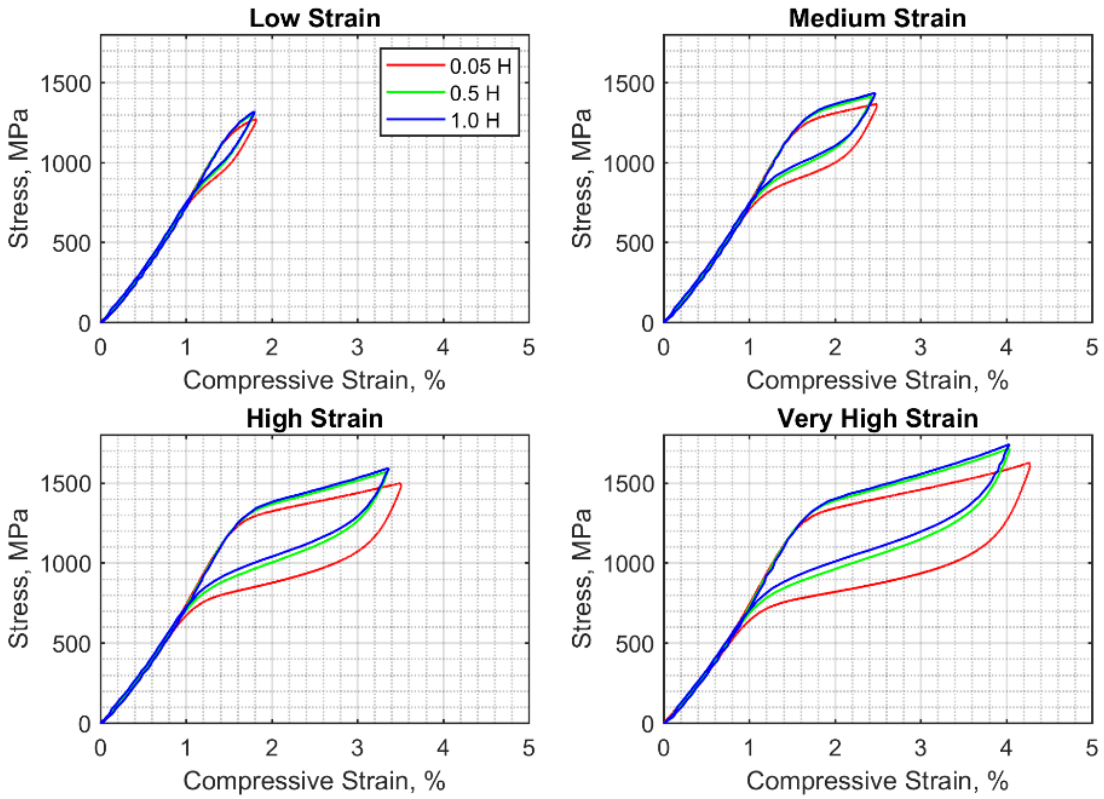

Figure 2-12 Stress-strain curves of NiTiHfPd-SC-(111)-400C-3hr-rate specimen SMAs the temperature of 25 °C with various strain and loading frequency levels

The mechanical behavior of NiTi SMAs is significantly influenced by their loading rate. The rate-dependent behavior is influenced by the complex interaction between stress, temperature, and the rate of heat generation during phase transformation [73]. The rate of loading influences the mechanical response characteristics of NiTiHfPd SMA, as observed in civil engineering structures under the dominant frequency range of 0.2 Hz to 4.0 Hz during an earthquake event. The increase in the loading frequency, and consequently the strain rate, increases the loading plateau and decreases the amount of the hysteretic damping of NiTi SMA [57, 59]. A researcher reported that the strain rate effects are caused by the inability of SMA to dissipate heat energy [74]. The larger diameter SMA bars generally display greater dependence on strain rate. The loading effect on the superelastic behavior of NiTi SMA is an important consideration in evaluating its mechanical characteristics before the actual implementation in civil engineering, since the SMA material encounters dynamic effects during earthquake events. Past research studies reported an inconsistency in findings on the effect of loading rate, which can be caused by multiple factors,

such as the different composition of the material, the experimental testing at different strain rates, and the experimental test conditions. When strain rates increase, the reverse transformation stress is also increased, without the considerable variation in the forward transformation stress, but the energy dissipation is decreased, as reported by [75-76]. Another study showed that the increase in strain rates contributes to an increase in both the forward and reverse stresses. Furthermore, another researcher noticed that the higher strain rates attribute to increase in the forward transformation stress, but decrease in the reverse transformation stress [77].

2.3.1.3 Influence of temperature

A temperature variation can considerably influence the material performance and hysteretic behavior due to thermal changes during the cyclic loading, since the phase transformation and superelastic behavior of NiTi wires and NiTiHfPd bars are also dependent on temperature variation. A number of researchers have conducted experimental tests to determine the influence of the temperature variation on the superelastic behavior of SMAs [57, 78-80]. The critical stress that activates the phase transformation changes significantly with temperature variations, as reported in the literature. It was reported that the increase in temperature linearly increases in the transformation stress and linearly decreases the equivalent viscous damping. Figure 2-13, which belong to current study, shows the stress-strain curves at various temperatures of superelastic NiTiHfPd bars experimentally tested. As it can be seen from Figure 2-13, the hysteresis loops of NiTiHfPd SMAs move upward with increasing temperature and also this can decrease dissipating energy capability as well as reducing equivalent viscous damping ratio. Figure 2-14 also shows the stress-strain curves at various temperatures of superelastic NiTi wires experimentally tested by [81]. It is reported that the superelastic behavior of NiTi wires was observed when the NiTi wires were heated above 0 °C, and the residual strains were noticed in hysteric responses above 40 °C. It can be seen in the Figure that the hysteresis curves can shift upward as the temperature increases.

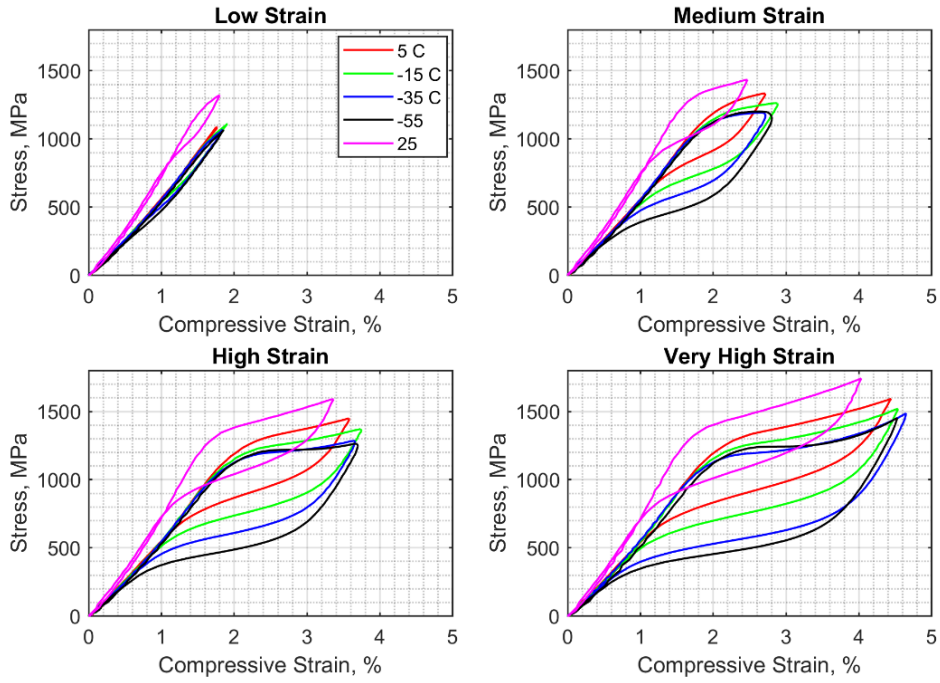

Figure 2-13 Stress-strain curves of NiTiHfPd-SC-(111)-400C-3hr-rate specimen SMAs at the loading frequency of 1.0 H with various strain and temperatures

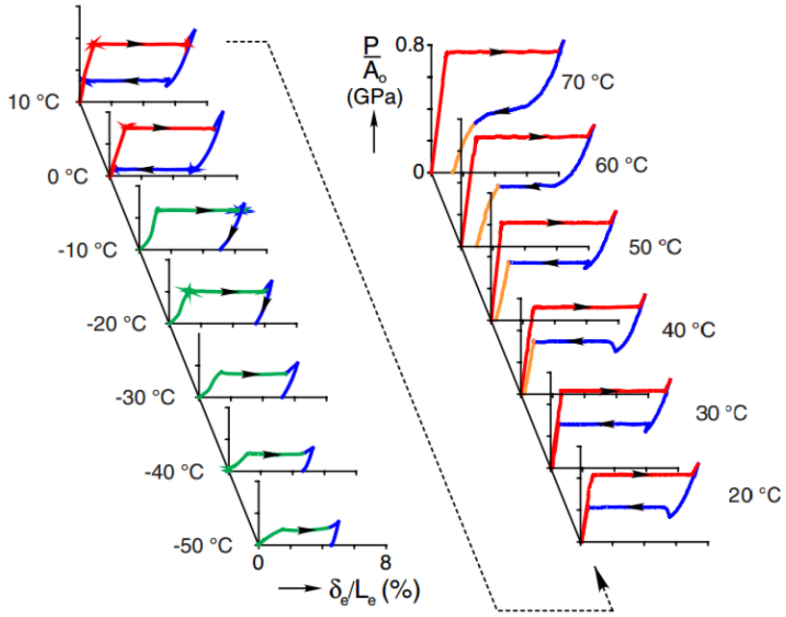

Figure 2-14 Stress-strain curves of NiTi wires at different temperatures [79]

2.4 Applications of Shape Memory Alloys in Civil Structures

The SMAs have been investigated for countless civil engineering applications. In this section, the applications of SMAs in steel beam-column connections, steel bracing systems, isolation systems and passive control devices are reviewed. Since there is not any structural application of the new developed NiTiHfPd SMA, in the following subsection the review will be limited to using NiTi SMA in civil engineering applications.

2.4.1 SMA-based Structural Connections

Numerous researchers have investigated the potential application of SMAs as a structural beam-column connection element that can ultimately control the damage and structural responses in both structural connections and the main structural components.

Two full-scale experimental tests were made on exterior joint connections using Nitinol SMAs according to the SAC loading protocol, to evaluate their connection behavior considering the ability of SMA tendons. As shown in Figure 2-15, the SMA tendons in a semi-rigid connection were assembled from the flange of the beam to the column to serve as the primary load transforming element for the steel structural connection. The SMA tendons were designed to initiate entirely the martensitic behavior, and subjected to several loading cycles at higher cyclic strains, up to 4%, without damage. To activate the shape memory behavior of the tendons, they were heated above the transformation temperature upon the end of the cyclic loading to regain their original configuration [82].

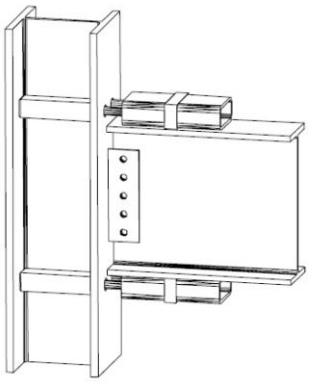

Figure 2-15 Innovative Steel Beam-Column Connection Using Shape Memory Alloys Tendons [82]

For comparison purposes, the companion steel connections were also experimentally tested to evaluate their performance. It was observed that the SMA connection revealed the stable and repeatable hysteresis behavior for rotations up to 4%. Comparing the hysteric behavior of the first and second test series, the moment rotation characteristics of the SMA tendon in the second testing series were identical to the first test. This result indicated the ability of SMA-based structural connections to sustain repeated large deformations without strength degradation, and to recover their initial properties following heating above their transformation temperature.

A researcher investigated the feasibility of an innovative beam-column connection consisting of an extended end plate with SMA bolts, beam flange ribs, and web stiffeners to predict the behavior of the SMA connection under quasi-static tests. Advanced 3D finite element models of the conventional end-plate bolted connection and the SMA-based structural connections were developed to compare the behavior of these two. This new SMA-based beam-column design concept appeared to enhance the seismic performance of structural connections, due to its excellent ductility and energy dissipation demands accommodated by the deformations of the superelastic SMA bolts. The result indicated that the SMA connection achieved the desired deformation capacity by controlling the moment-carrying capacity of the bolt cluster below the elastic flexural capacity of the connecting beam and forming the plastic hinge within the beam-column interface. Similarly, SMA connections recovered up to 94% of the total deformation due to the non-occurrence of local buckling of SMA connections during entire loading cycles, indicating the effectiveness of increasing the distance of the bolt to reduce residual deformation. Hence, the resulting benefits of SMA connections were enhanced ductility, moderate energy dissipation capacity, and excellent re-centering capability, which can minimize post-earthquake repair work and costs to repair structural elements. Figure 2-16 illustrates the SMA connection diagram in the beam-column connection [83].

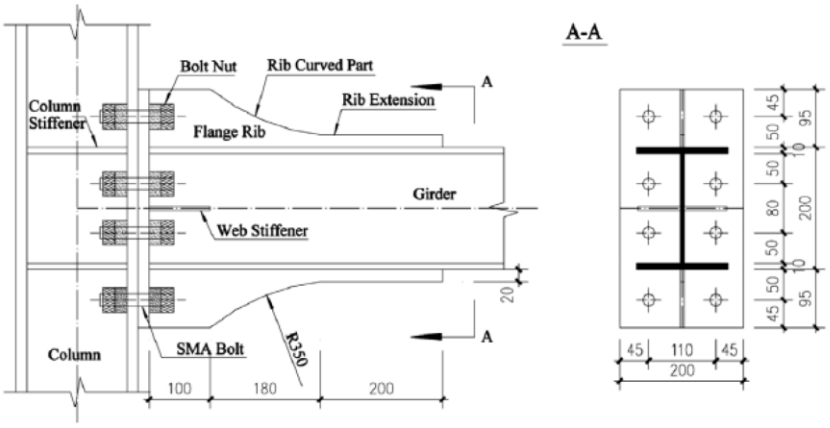

Figure 2-16 The SMA connection diagram [83]

The seismic behavior of superelastic SMAs are numerically studied by [84] in the beam-column connections of steel moment resisting frames. The numerical simulations were conducted for a set of steel structural models with a different number of stories and varying eccentricities, incorporating SMA connections subjected to different bi-directional earthquake components. In the study, extensive nonlinear time history analyses were made in order to examine the performance of SMA-equipped structural connections in reducing their seismic response, and to evaluate the energy dissipation capability of the structural connection. The comparative evaluation of inter-story drift, base shear capacity, moment-rotation behavior of structural connection, and residual strains was reported for both the conventional steel moment resisting frame and the frame model with SMA connections, to demonstrate the efficiency of the steel structural model equipped with new SMA connections. The result indicated that the application of the SMA connection in the steel structural model reduced the base shear-force of the structural model and residual displacement due to the superelastic characteristic of SMA materials. However, structural models with SMA connections were not able to produce significant reduction in lateral displacements, compared to the responses of the structural model with fixed connection models.

The experimental investigation of steel structural connections with copper-based SMA bars is reported by [85] for a prototype of partially restrained connections subjected to a controlled cyclic displacement history. The physical model of the structural connection included an end-plate connection at a rectangular hollow structural beam connected to a wide flange column, which were connected by four CuAlBe SMA bars in the austenitic phase. A simple experimental test set-up

for the SMA-based structural connection was developed to explore the potential of SMA prestressed bars subjected to dynamic cyclic tests. The static tensile test results showed that the fracture strain was approximately 8%, with a transgranular fracture mechanism. Similarly, SMA-based structural connections demonstrated a moderate level of energy dissipation, superelastic behavior, and no strength degradation, up to 3% drifts under several cycles of dynamic loading. After evaluating the performance of structural connections, numerical simulations of a three-story benchmark building were also presented, to compare the dynamic performance of a rigid steel building and a partially restrained building equipped with SMA-based connections. The preliminary results highlighted that copper-based SMA rods at structural connections did not provide a specific conclusion about the potential advantage of CuAlBe connections in steel moment resisting frames.

A half-scale interior beam-column connection is explored, as shown in Figure 2-17, incorporating superelastic nickel-titanium (NiTi) shape memory alloy (SMA) tendons, which were designed, fabricated, and tested experimentally. To assess the feasibility of structural connections in a moment resisting frame, experimental tests were conducted in frames designed with the four different tendons, for structural connections made of (i) steel, (ii) martensitic NiTi SMA, (iii) superelastic NiTi SMA, and (iv) superelastic NiTi SMA in parallel with aluminum. The low-strength aluminum bars were employed to contribute additional energy dissipation. In this study, the re-centering connections were designed in such a way that inelastic deformations occurred in the tendons, while the other members of the structural system remained in the elastic range. The experimental test results illustrated that a superelastic NiTi SMA-based structural connection contributed excellent ductility, energy dissipation, and re-centering properties compared to the other two connections made from steel and martensitic NiTi SMA. The superelastic SMA-connection was found to possess significant superelastic behavior at drift levels below 1%, and to recover 85% of its total deformation after being cycled to 5% drift demand, highlighting the excellent re-centering capabilities of the superelastic nickel-titanium SMA-based beam-column connections.

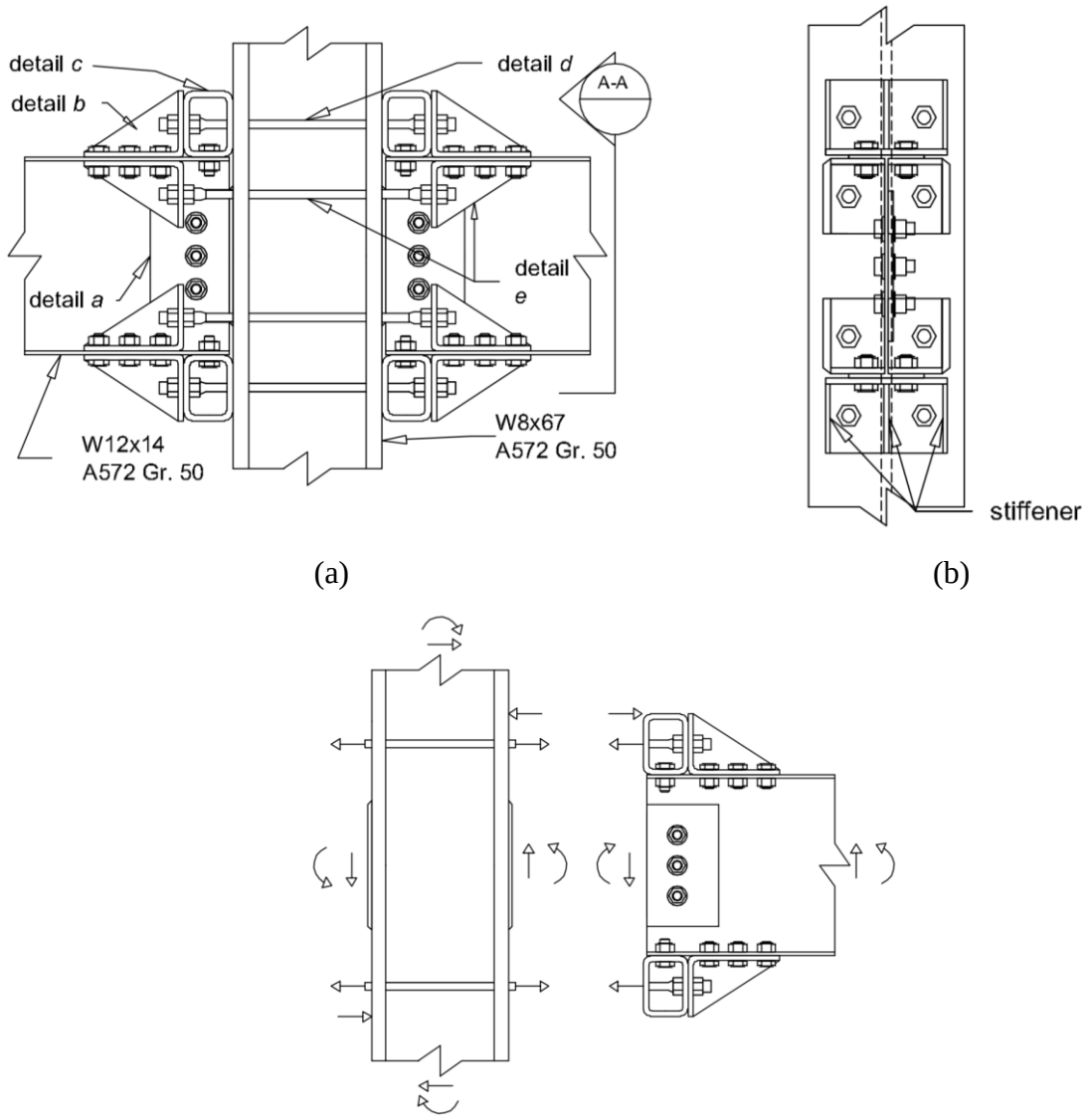

Figure 2-17 Steel beam-column connection details (a) Front view (b) Side view, section A-A (c) Free body diagram (interior brackets excluded) [86]

Both numerical study and experimental tests are conducted by [87] on the extended end-plate connections with NiTi SMA bolts, as shown in Figure 2-18, to demonstrate responses in terms of re-centering ability, supplementary energy dissipation, and hysteretic stability. Initially, seven full-scale tests were performed to validate the cyclic responses of numerical modeling results. The results of detailed finite element analyses demonstrated good agreement with the test results in terms of the hysteric moment-plastic rotation behavior, energy dissipation characteristics, and re-centering ability. After validating the numerical modeling strategy, a parametric study was carried

out to demonstrate the influence of bolt geometry/layout; beam behavior; beam-to-connection strength ratio; end-plate thickness; column deformation behavior; and shear-resisting mechanism. In order to address the major concerns identified from the parametric study, an improved connection type was proposed, using a high-strength (HS) SMA hybrid solution, in which HS bolts and SMA bolts were employed to resist the shear force and to provide recoverable bending resistance, respectively. The hybrid structural connection incorporated the multi-functional use of SMA Belleville washers for protecting the HS bolts, enabling connection re- centering ability, and offering supplementary energy dissipation. Finally, the feasibility of the HS-SMA hybrid connection was confirmed through a detailed FE model, and a design recommendation on the NiTi SMA equipped end-plate connection was proposed for the normal design of such connections.

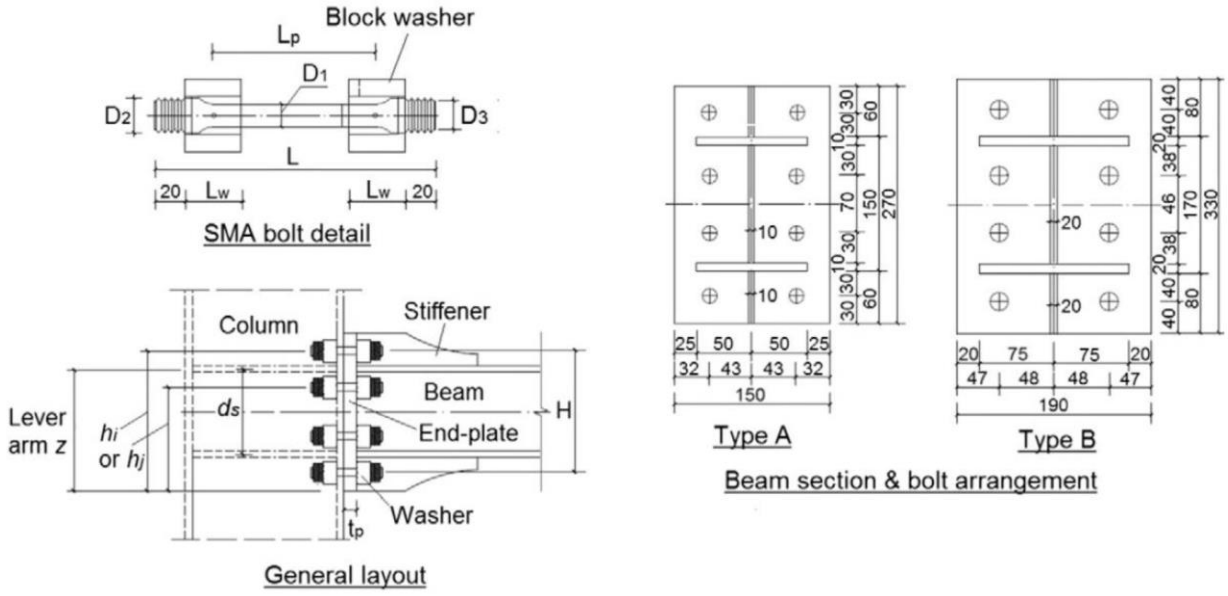

(a)

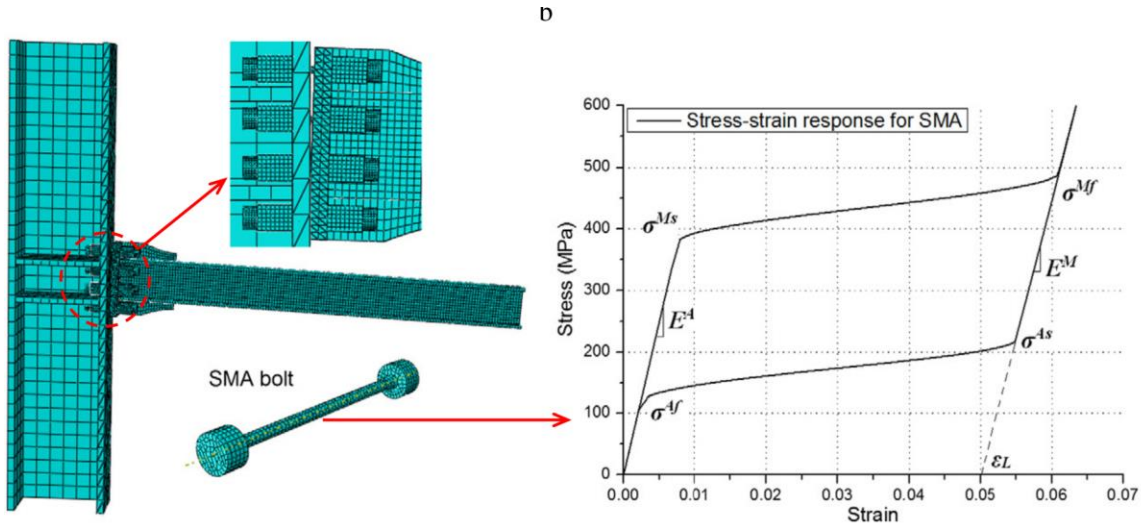

(b)

Figure 2-18 (a) Geometric configurations and layouts (b) FE mesh and stress–strain response for SMA [87]

2.4.2 SMA-based Bracing Systems

The seismic performance of concentrically braced frames with superelastic SMA braces is investigated by [88], to address the limitations of the conventional brace frame systems in terms of ductility and energy dissipation due to the buckling of conventional braces. In order to reduce the length of SMA braces, chevron braced frames were developed employing SMA bars in parallel, consisting of each single bar, with varying diameters from 12.7 to 31.75 mm, connected to the frames through rigid elements. An extensive analysis of three- and six-story concentrically braced frame systems with either superelastic SMA braces or conventional steel braces was conducted. A series of nonlinear time history analyses were conducted to identify the potential benefits of using SMA braces for the dynamic control of braced-frame systems. For the comparative evaluation of two braced systems, the frames with SMA braces were designed to provide yield force and initial stiffness to equal that of the conventional steel brace system, such that both frame systems revealed the same fundamental period. The results highlighted that frames with SMA braces contributed promising benefits in controlling inter-story drift and residual drift during an earthquake event, indicating excellent re-centering characteristics of superelastic SMAs. Furthermore, SMA braces appeared to be the most effective in limiting inter-story drift in the lower stories of tall buildings, compared to the drift of conventional steel brace systems.

The seismic performance of steel frame systems installed with superelastic SMA braces in buildings having various stories and different bracing configurations, is studied by [89] to evaluate the efficiency of SMA braces. In order to compare the responses, steel buildings with varying stories (4, 6, 8, 10, 12, and 14 stories) for four different bracing configurations (diagonal, split X, chevron V, and inverted V) were designed, considering three groups of braced frames: an SMA brace system with rigid element, an SMA brace system with buckling restrained braced (BRB) element, and a BRB system. To evaluate the potential benefit of an SMA-based innovated bracing system, the dynamic response of a steel braced frame equipped with SMA braces was compared to the brace system with BRBs, subjected to three ground motion records. The results of the comparative study revealed that the frame system with SMA braces provided a more effective method to reduce both inter-story drift and residual drift, and to minimize losses associated with damage to structural systems during earthquake events, independent of both the structures' brace configurations and their stories. Moreover, the results indicated that the energy dissipation capabilities of the SMA-braced systems were comparable to BRB frame systems. In addition, the SMA-braced systems were able to reduce peak inter-story drift up to 60%, lessen residual deformations in the structure due to excellent re-centering ability, and reduce the deformation demand on the column members at each floor level. Figure 2-19 displays the bracing system with the SMAs, which highlights the SMA connection with either a rigid brace or a buckling restrained brace.

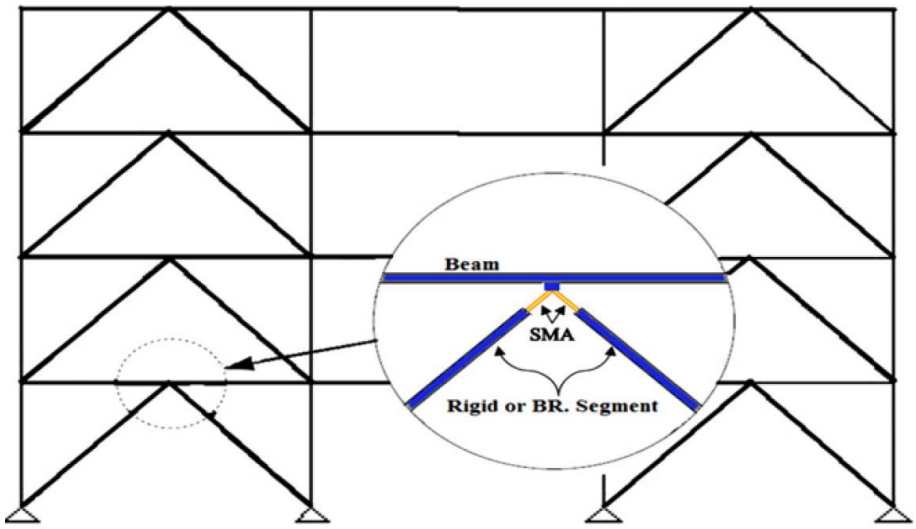

Figure 2-19 Bracing system with SMA connection in two cases [89]

A high-performance, self-centering, buckling-restrained brace (SC-BRB) is developed by [90] as shown in Figures 2-20 and tested the SC-BRB experimentally under the uniaxial quasi-static cyclic loading. The SC-BRB comprised the robust hysteric behavior of two distinct components: a typical BRB component to provide energy dissipation, and superelastic NiTi shape memory alloy (SMA) rods to offer self-centering as well as additional energy dissipation. In this study, the self-centering mechanism was provided by the combination of SMA rods and the BRB, using a configuration of concentric tubes and free-floating end plates that caused the pretensioned SMA rods to elongate when the brace was in either tension or compression. The application of SMA rods contributed large deformations with considerably lower residual deformation, and dissipated energy, as revealed by the flag-shaped hysteretic behavior. The SC-BRB was easily implemented, adopting current design practice, and was employed in place of a steel brace or a BRB following the conventional braced-frame configuration. To validate the innovative brace concept, two half-scale SMA-based SC-BRBs were designed, fabricated, and tested, adopting a standard cyclic loading protocol. The experimental result showed that the use of superelastic NiTi SMAs in the SC-BRB illustrated the promising benefits of the stable hysteretic behavior, including excellent energy dissipation, self-centering capability, and both large maximum and cumulative deformation capacities. The result also demonstrated that the residual brace deformation was controlled by suitably adjusting the ratio of initial SMA pretension force to the strain-hardened BRB core yield force.

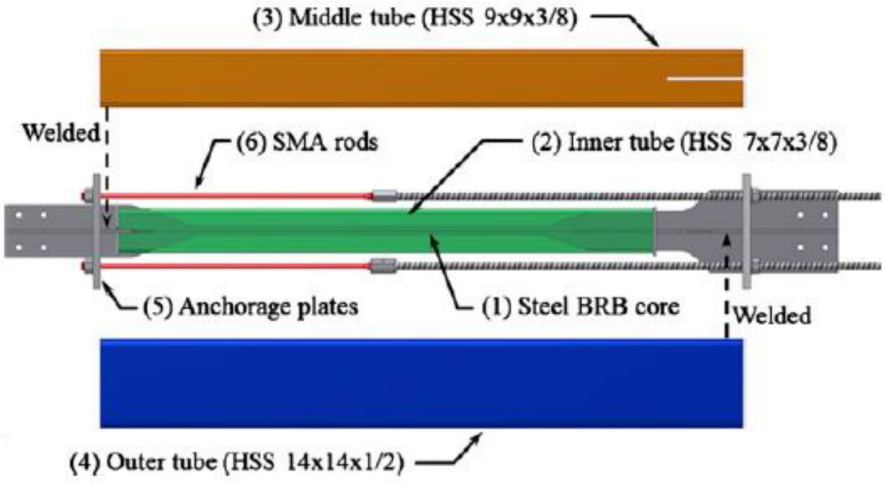

(1)

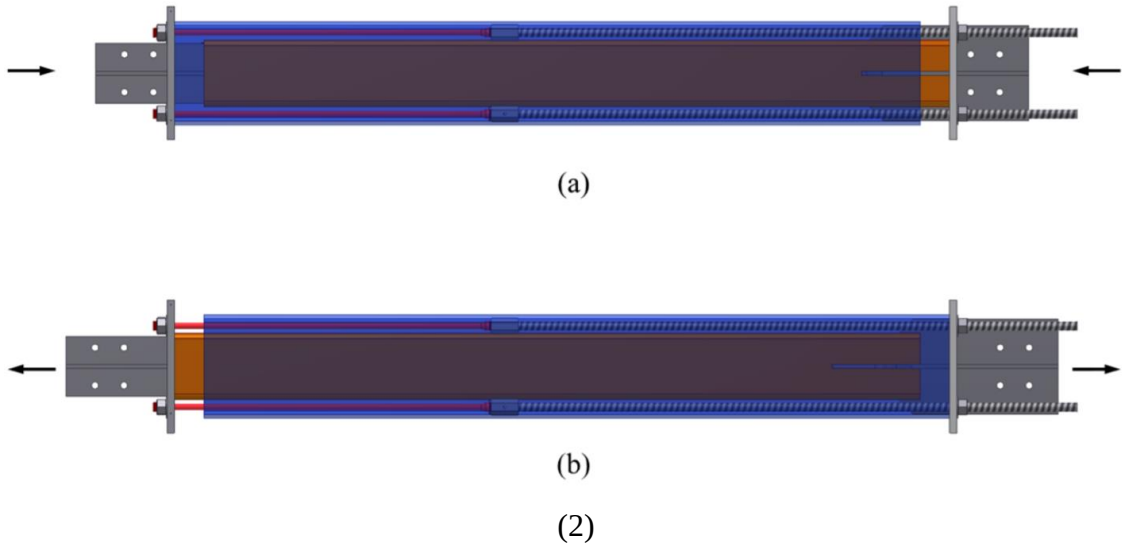

Figure 2-20 (1) SC-BRB components (2) SC-BRB mechanics (a) SC-BRB in compression with gap opening at right end; (b) SC-BRB in tension with gap opening at left end [90]

A steel frame system is researched by [91] with a superelastic Cu-Al-Mn SMA tension brace as a self-centering element in shaking table tests under a series of scaled earthquake ground motions experienced during the 1995 Kobe earthquake in Japan. The large diameter SMA bars, entitled Cu-Al-Mn bars, were recently developed. The results highlighted that the proposed SMA braces were effective in providing self-centering capabilities and in preventing punching. After calibrating the numerical prediction with respect to the response observed from the shaking table tests, the numerical simulations using the calibrated analytical models for the SMA-based tension braces were also performed, under a suite of near-fault ground motions, to access the effectiveness of the SMA braces considering the variability of ground motion records. The results of the validated numerical simulation under near-fault ground motions reinforced the effectiveness of the SMA-based tension brace, indicating an acceptable range of drift angle of less than 0.02 rad, and strains in SMA bars of less than 5%. In this study, a simple stopper, or a deformation-restraining device was also proposed, to ensure extra safety to the frame when experiencing unexpectedly strong ground motions. The test results demonstrated that the installation of stoppers was effective to prevent premature fractures due to imposed loading. Figure 2-21 illustrates the superelastic SMA tension bar with the mechanism of the stopper.

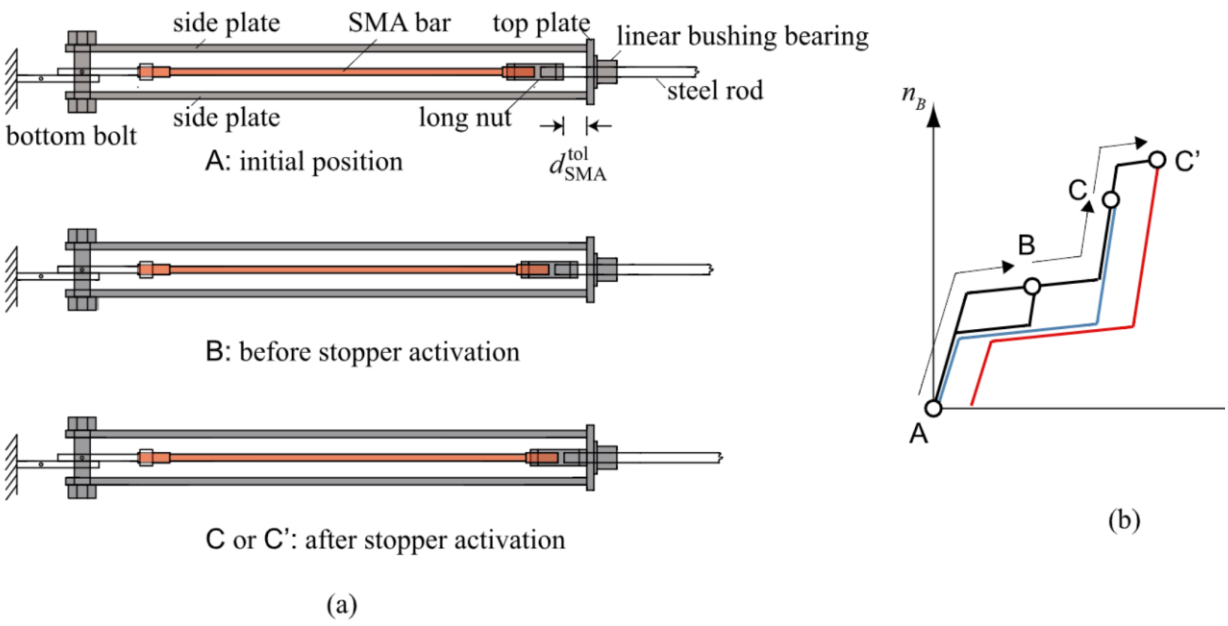

Figure 2-21 Mechanism of the stopper: (a) deformation of the shape memory alloy (SMA) bar. (b) The relation-ship between the brace axial force n_B and the brace elongation d_B [91]

A bracing system is investigated by [92] based on an SMA ring which is capable of both re-centering and energy dissipation. This lateral force resisting system is a cross-braced system consisting of an SMA ring and four tension-only cable assemblies, which can be applied to both new construction and seismic retrofit. The performance of this bracing system is examined through a quasi-static cyclic loading test and finite element (FE) analysis. The system has two configurations with different components installed. One is the system as shown in Figure 2-22(a) with only SMA wires inside the AQ (AQ-S bracing system), and the other is the system as shown in Figure 2-22 (b) with both SMA wires and two C-shape steel dissipaters installed inside the AQ (AQ-SC bracing system). The performances of these bracing systems were investigated through quasi-static cyclic loading tests. The AQ-S bracing system showed great re-centering ability with a residual story drift of only 0.12% after the test frame was pushed to 3% story drift. The AQ-SC system exhibited higher damping capacity as well as satisfying re-centering capacity with a 0.47% residual story drift after the 3% story drift. As a result, these seismic bracing systems based on SMA wires displayed good performances which are clearly needed in seismic design and retrofit for both new constructions and existing structures.

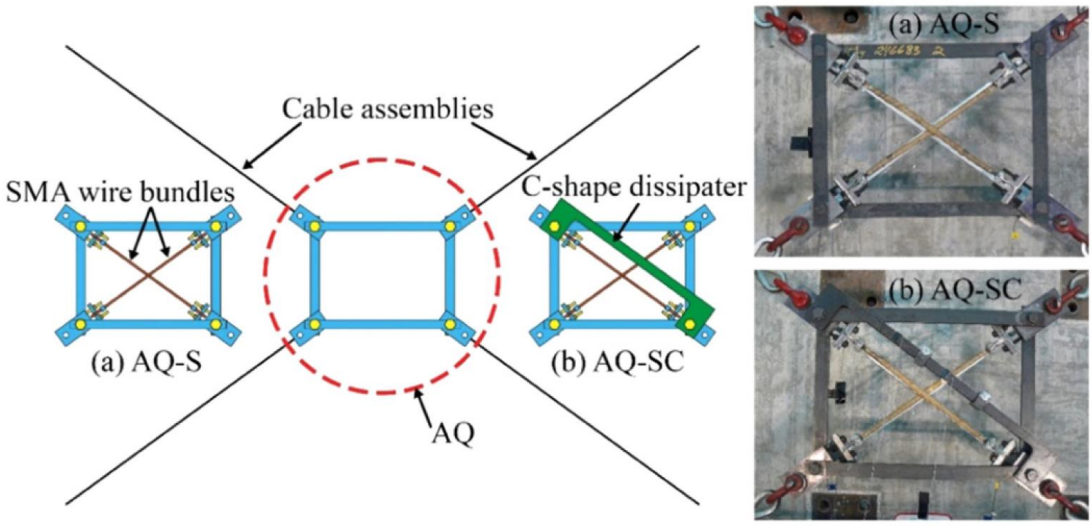

Figure 2-22 SMA-based articulated quadrilateral (AQ) bracing system: (a) AQ-S configuration and (b) AQ-SC configuration [92]

Seismic performance of steel frame buildings with SMA-based self-centering bracing systems is explored by [93]. The self-centering bracing system described in this study relies on superelastic response of large-diameter cables. The bracing systems is designed such that the SMA cables are always stressed in tension. An SMA-based bracing system that has both energy dissipation and self-centering abilities is proposed in this study. A schematic diagram and cross-sectional view of the SMA bracing system are shown in Figure 2-23 (a). The SMA bracing system consists of an outer member, an inner member, SMA tendons, two end plates, a connection plate and two guide members. The inner member is a steel I-section with an extended web at one end. The inner member is placed into the outer tubular member to guide the SMA cables. The outer member is a steel box section with a connection plate welded to one of its end. The SMA cables are anchored to two end steel plates that can freely move under the guidance of inner member. The design mechanism of the SMA bracing system allows SMA cables to work always in tension when the bracing system itself is either under tension or compression. When the bracing system is under compression, the inner member will move to the right and push the right end plate away. However, the left end plate will be blocked by the outer member, which will produce tensile forces in the SMA cables (Figure 2-23(b)). When the bracing is in tension, the inner member will pull the left end plate but the right end plate will be blocked by two guide members attached to the outer box beam (Figure 2-23(b)). Therefore, the SMA cables will again

be under tension. SMA bracing system considered in this study exploits advantageous characteristics of large diameter SMA cables to provide a flag-shaped hysteretic response.

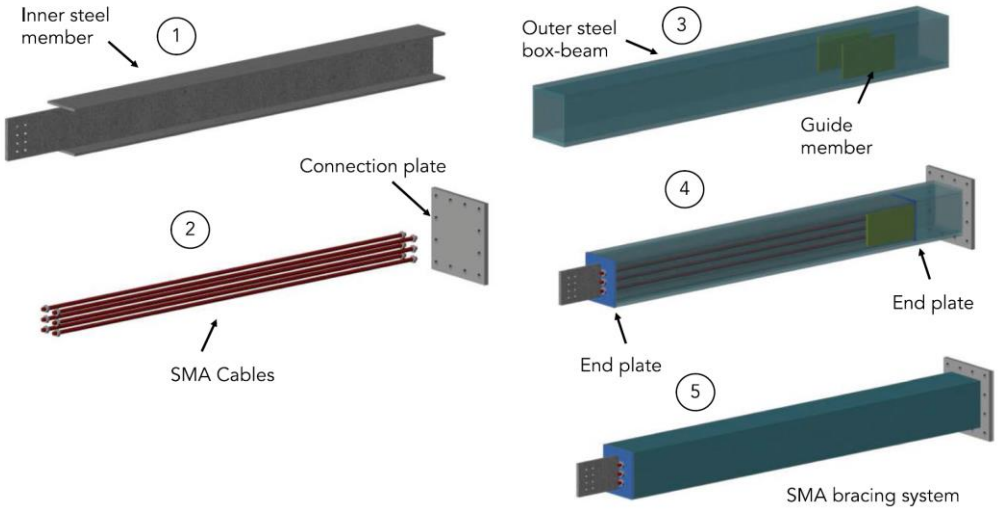

(a)

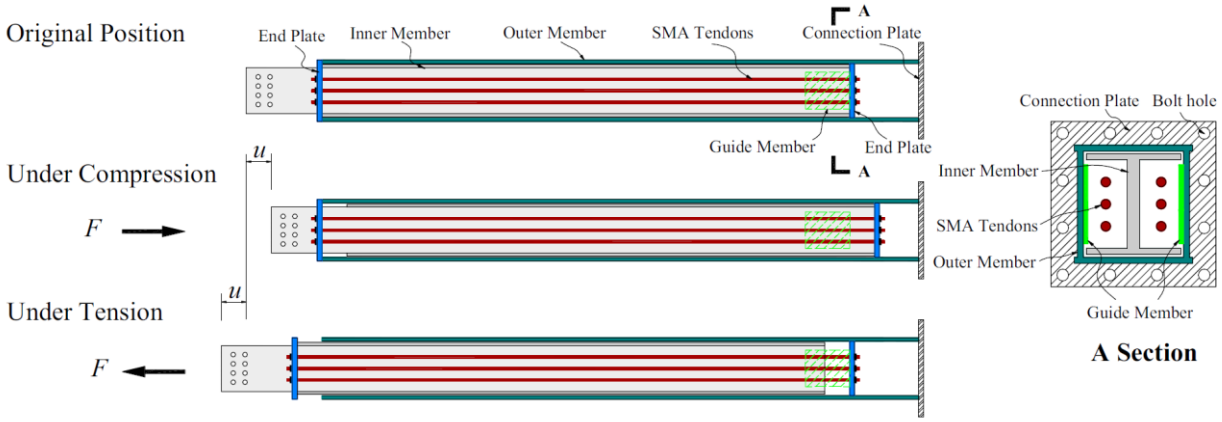

(b)

Figure 2-23 (a) SMA bracing system and its components, (b) SMA bracing system at the displaced positions [93]

2.4.3 SMA-based Isolation Systems

The seismic performance of an SMA-based, sliding-type, base isolation system under variations of environmental temperatures is studied by [94]. As shown in Figure 2-24, the SMA-based isolation system strategically combined a steel-Teflon sliding bearing, which was employed to dissipate energy through frictional behaviors, and NiTi SMA wires, which were used to offer

additional energy-dissipating and re-centering capabilities. In order to capture the behavior of superelastic NiTi wires under variations of temperature and loading-rate, a neuro-fuzzy model was used to predict the force of SMA wires. A multi-objective genetic algorithm was employed to determine the length and cross-sectional area of the SMA wires, which were the primary design parameters of the SMA device. A sliding bearing with an SMA device was installed in a multi-span bridge to evaluate the seismic performance of the isolation system under various outside temperatures. The result demonstrated that temperature changes indicated a modest influence on the performance of isolated bridge structures. Particularly, the result highlighted that the structural responses of the isolated bridge were affected as follows: a maximum of 13% variation on the displacement response, and a maximum of 8% change in acceleration response when the temperature change was 20 °C from the reference temperature of 20 °C. The result revealed that SMA-based sliding isolators were effective to control the structural response of isolated bridges subjected to earthquake events.

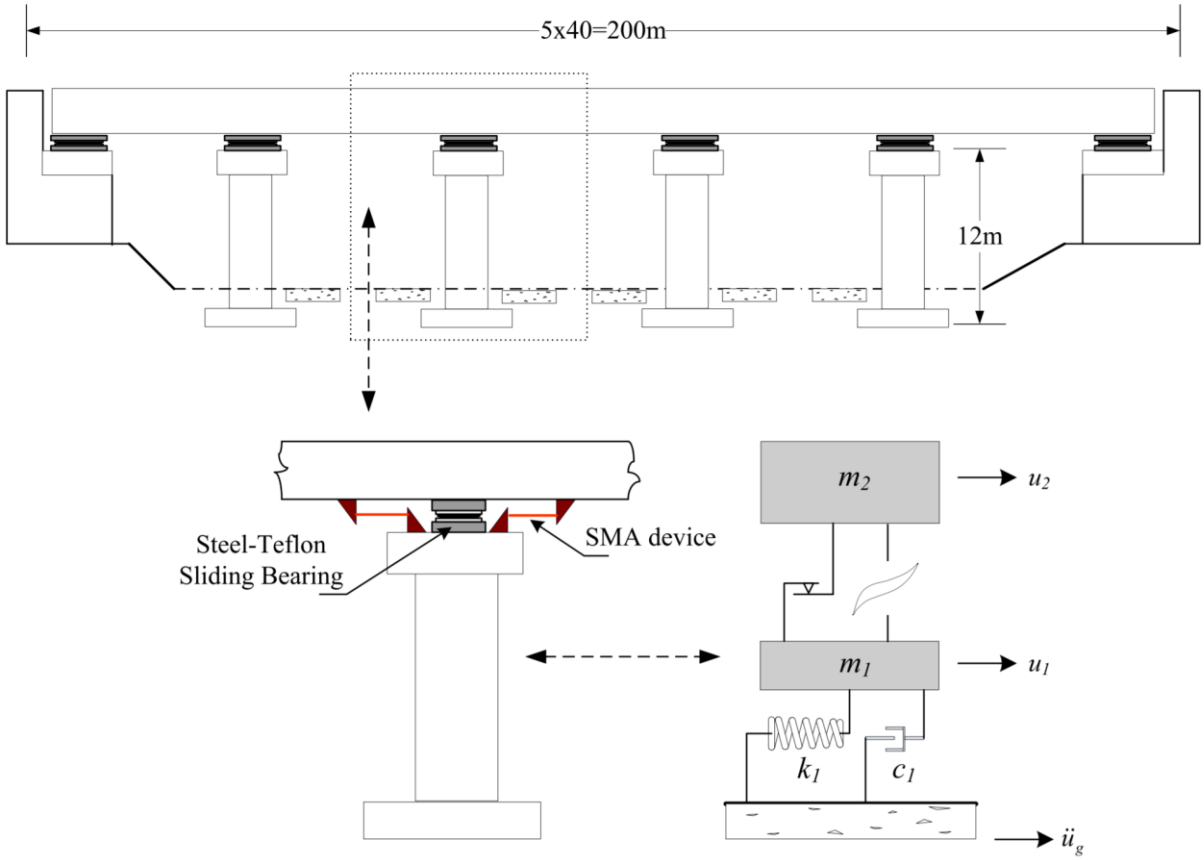

Figure 2- 24 A bridge structure modeled with sliding bearings and SMA device [94]

The seismic performance assessment of a bridge structure isolated by a high-damping rubber bearing (HDRB) is conducted by [95] and an SMA-based rubber bearing (SRB), as shown in Figure 2-25 to assess the effectiveness of different isolation systems subjected to moderate to strong ground motion records. For the combined isolation bearing, the SRB consisted of a natural rubber bearing (NRB) wrapped with shape memory alloy (SMA) wires. Two types of combined isolation bearings, SRB-1 and SRB-2, were proposed by using two types of SMA wires, Cu-Al-Be and Ni-Ti wires, respectively. The bridge structure isolated with three versions of isolation systems, named as HDRB, SRB-1, and SRB-2, was modeled considering appropriate hysteric behavior for these isolation systems. To simulate the superelastic and damping characteristics of SMA wires, a simplified viscoelastic analytical model was adopted. The numerical results demonstrated that SMA-based isolation bearings satisfactorily indicated the superior seismic performance in controlling residual displacement of the bridge deck and the displacement of the bridge pier when subjected to moderate seismic events. However, these results also demonstrated that the SMA-based isolation systems, with Ni-Ti and *Cu-Al-Be,* were not able to restrain the residual displacement and pier displacements for strong earthquakes. This study highlighted that the seismic response of the bridge structure was influenced by both the type of isolation bearings and the effect of the modeling of isolation bearings.

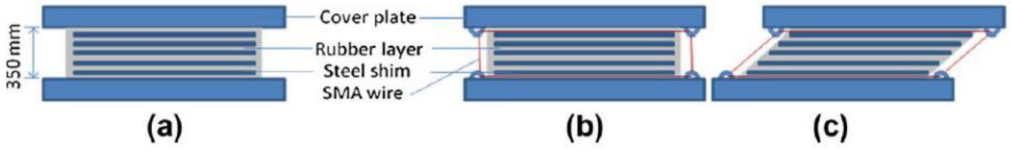

(1)

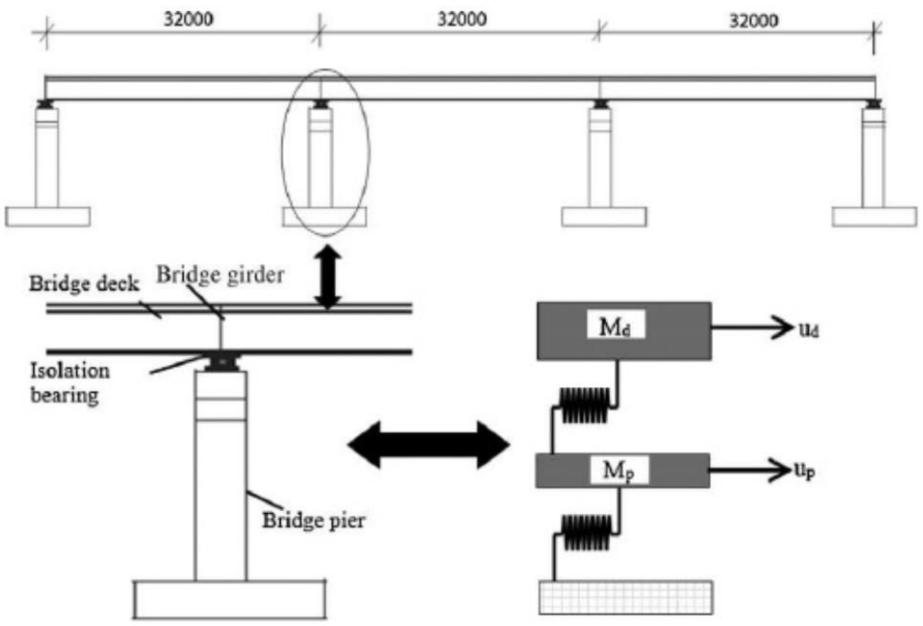

(2)

Figure 2-25 (1) Description of the isolation bearing (a) HDRB; the rubber layers with high-damping properties are vulcanized by steel shims, (b) SRB in un-deformed condition, and (c) SRB in deformed condition (2) Analytical modeling of the bridge pier [95]

The seismic performance of building structures isolated by the SMA-supplemented rubber bearing (SMARB) is investigated by [96] as shown in Figure 2-26. The study compared the performance of SMARB over the traditional lead rubber bearing (LRB) under near-fault earthquake records. The numerical study presented the comparative response evaluation of the isolated buildings under a set of historical near-fault, fault-normal components of earthquake records. A parametric study was conducted to identify the optimal characteristic strengths for both the SMARB and LRB systems. Next, the robustness of the seismic performance improvement was also presented, under the varying system characteristics of the superstructure-isolation parameters and the different scenarios of earthquake loadings. The result demonstrated that the seismic performance of the building structure isolated by SMARB was superior over the performance of the conventional LRB under near-fault earthquakes. The result showed that the application of SMARB provided significant improvements in isolation efficiency, indicating considerable reductions of both the peak and residual displacement of the bearings over the application of elastomeric bearings, such as LRB. It was also concluded that the SMARB was more effective in providing protection for

frequency-sensitive equipment, by suppressing the transfer of high-frequency components of ground motions.

The optimal performance of a building frame isolated by an SMA-based lead rubber bearing (SMA-LRB) is proposed by [97] under random earthquake events. The SMA-LRB, as shown in Figure 2-27 was proposed by combining the superelastic property of SMA and LRB as the most widely used base isolation system. In this study, a shear building model isolated by the SMA-LRB system was analyzed through nonlinear random vibration analysis to assess the effectiveness of the proposed SMA-based isolation device.

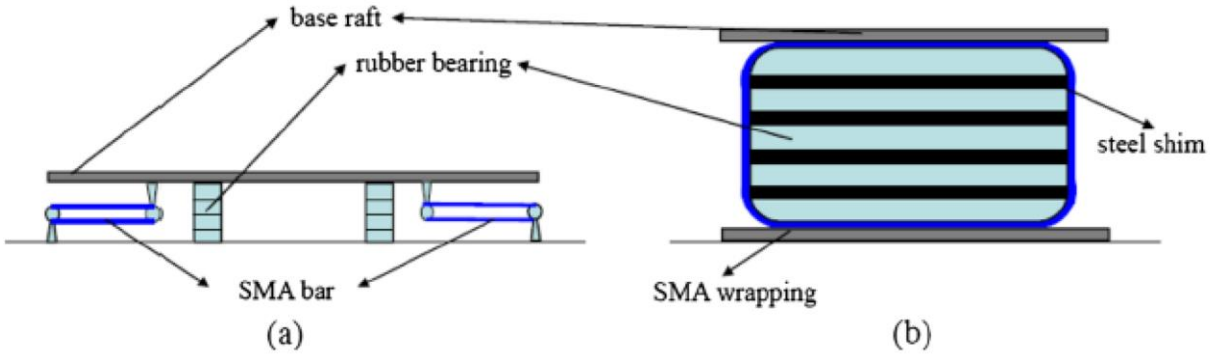

(1)

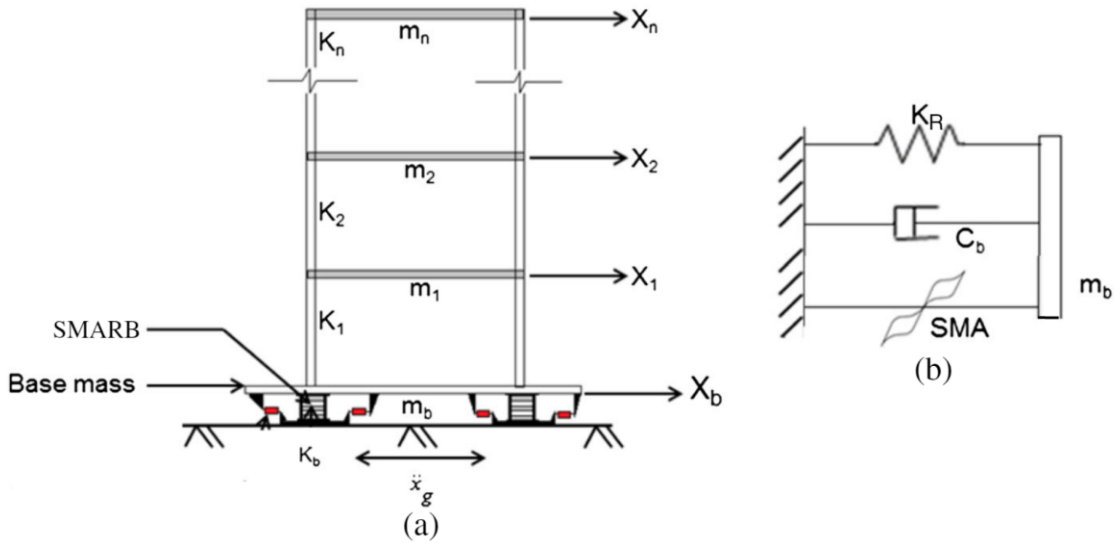

(2)

Figure 2-26 (1) Configurations of the SMARB system: (a) shape-memory alloy (SMA) cable/bar supplementing RB and (b) the rubber bearing with SMA wrap (2) (a) Idealized model of the base-isolated building frame by shape-memory-alloy rubber bearing (SMARB) and (b) a mechanical idealization of the SMARB [96]

Moreover, a bi-objective optimization was formulated to ensure optimal performance of the device by considering two design variables, namely the transformation strength of the SMA and the yield strength of the LRB. The numerical result demonstrated that a base isolation system designed with the set of optimal characteristic strengths of the SMA and LRB was essential to ensure superior performance, by minimizing isolation displacement as well as maximizing isolation efficiency. The results of the parametric study illustrated that the isolation system with optimal design parameters enhanced the robustness of the isolation system under the possible ranges of variations in periods of the system, as well as different earthquake loadings.

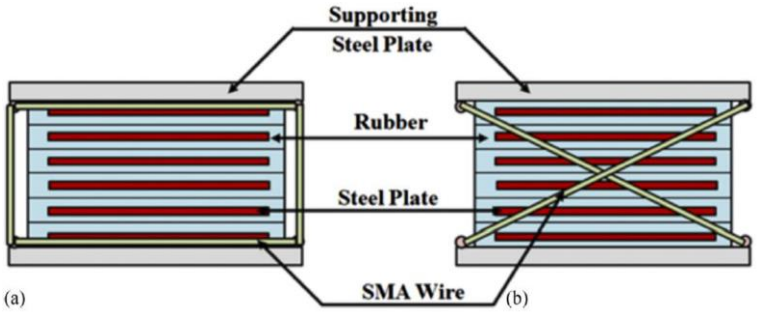

(1)

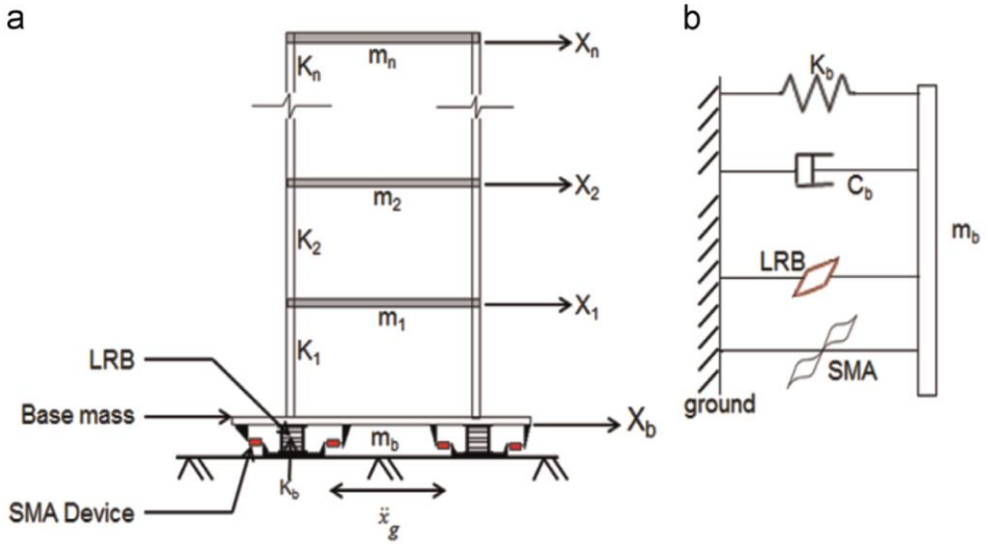

(2)

Figure 2-27 (1) Configuration of the isolation system supplemented with SMA (2) Idealized model of the (a) base isolated structure and (b) SMA-LRB isolation device. [97]

The influence of high austenite stiffness of shape memory alloy (SMA) used in the elastomeric rubber bearings (ERB) are presented by [98], entitled SMA supplement elastomeric rubber bearing (SMARB), to evaluate the structural response of base-isolated buildings subjected to near-fault earthquake excitations. Figure 2-28 shows the configuration of SMARB. The study evaluated the structural response of the building, considering three structural response parameters: top floor acceleration, isolation displacement, and base shear. The effect of the isolation time period, the transformation strength of SMA, and austenite stiffness on the structural response was investigated. The result demonstrated that the SMA-based isolation devices with high austenite stiffness excited the higher modes of the base-isolated structures; thus, higher acceleration associated with higher frequencies were transmitted to superstructures. However, an isolation device with the high austenite stiffness of SMA did not considerably influence the base displacement and base shear of structures.

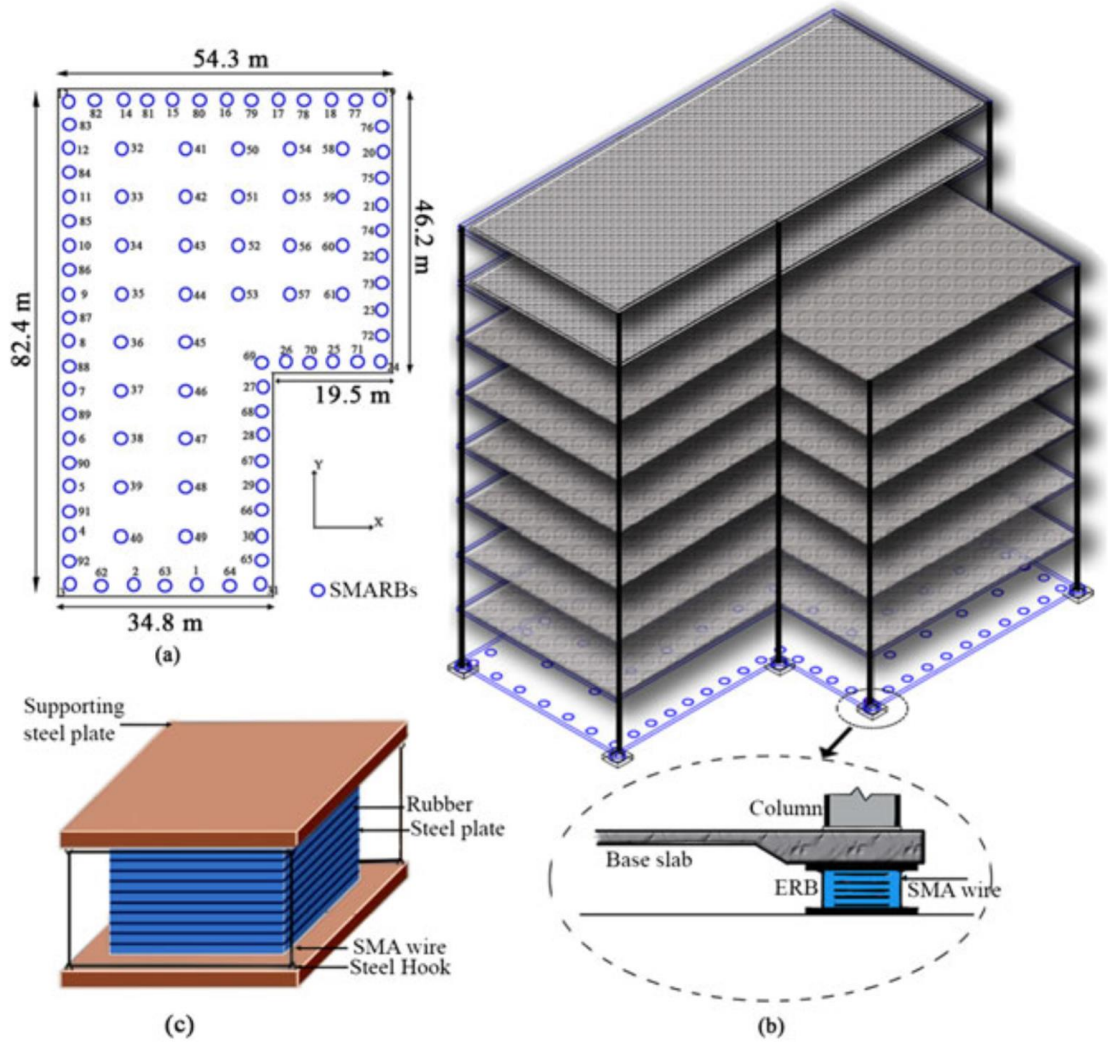

Figure 2 28 (a) Plan of base-isolated benchmark building with shape memory alloy (SMA) supplemented isolation bearings (b) Elevation of base-isolated benchmark building frame (c) SMA supplement elastomeric rubber bearing (SMARB) [98]

2.4.4 SMA based dampers

The effectiveness of an SMA-based reusable hysteric damper (RHD) in the seismic response control of civil engineering structures subjected to strong earthquake events are conducted by [99]. The RHD, as shown in Figure 2-29 was developed to provide distinctive features, such as the tunable hysteric behavior and the ability to withstand several design-based earthquakes by utilizing superelastic Nitinol stranded wire for energy dissipation. In the design of the RHD, design parameters, such as the inclination angle of the SMA wires, pretension levels, and friction

coefficients of the damper, were adjusted to achieve the suitable hysteretic behavior of the damper while using the device for passive structural control. The hysteric behavior of the RHD device was validated through the experimental test results, and an analytical model of the RHD was developed to predict its response. A parametric study was conducted to examine the influence of design parameters on the damper's energy-dissipating performance. The numerical simulation of a three-story steel building with and without RHDs was conducted to evaluate the effectiveness of the RHD as a passive structural control of structure systems. The results demonstrated that the RHD device was effective in reducing the structural response of steel frame structures excited by strong earthquake events.

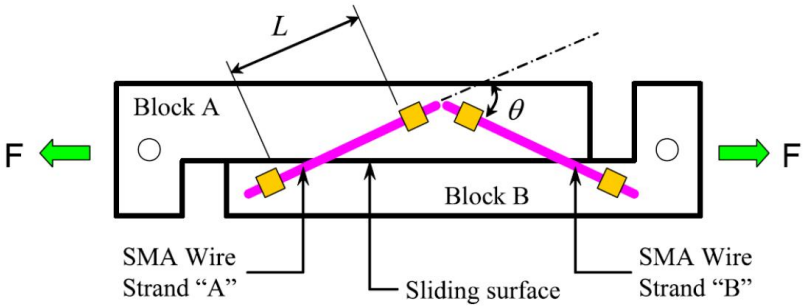

(a)

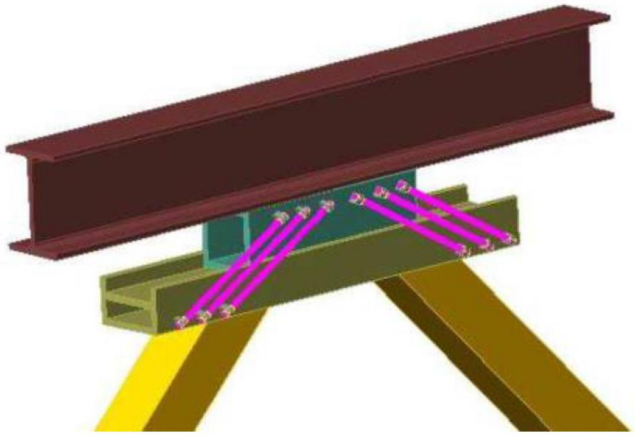

(b)

Figure 2-29 Schematics of the (a) SMA-based reusable hysteretic damper, (b) an RHD in a steel framed building [99]

Again, the self-centering capability of a special SMA-based bracing element named as self-centering friction damping brace (SFDB) are carried out by [100], as shown in Figure 2-30. The SFDB was developed by leveraging the re-centering capability of superelastic Nitinol wires and the enhanced energy dissipation capability of a friction-based mechanism. The dynamic analyses of three- and six-story steel concentrically braced frames (CBFS) were conducted for a comparative evaluation of SFDB frames and buckling restrained braced (BRB) frames subjected to two suites of historical ground motions for Los Angeles. The self-centering behavior of the SFDB was obtained by suitably selecting the ratio between the yield strength of the Nitinol SMA and the friction force developed in the device. The result demonstrated that SFDB frames were capable of providing a comparable seismic response to that of BRB frames, in terms of peak inter-story drift, while reducing the residual drift considerably. Furthermore, the results highlighted the enhanced seismic performance of the SFDB due to the potential benefit of the frictional damping in the device. The comparative study concluded that the SFDB revealed promising characteristics, in withstanding several design-based earthquakes with no need of replacement, due to the full strain recovery feature of superelastic SMA wires.

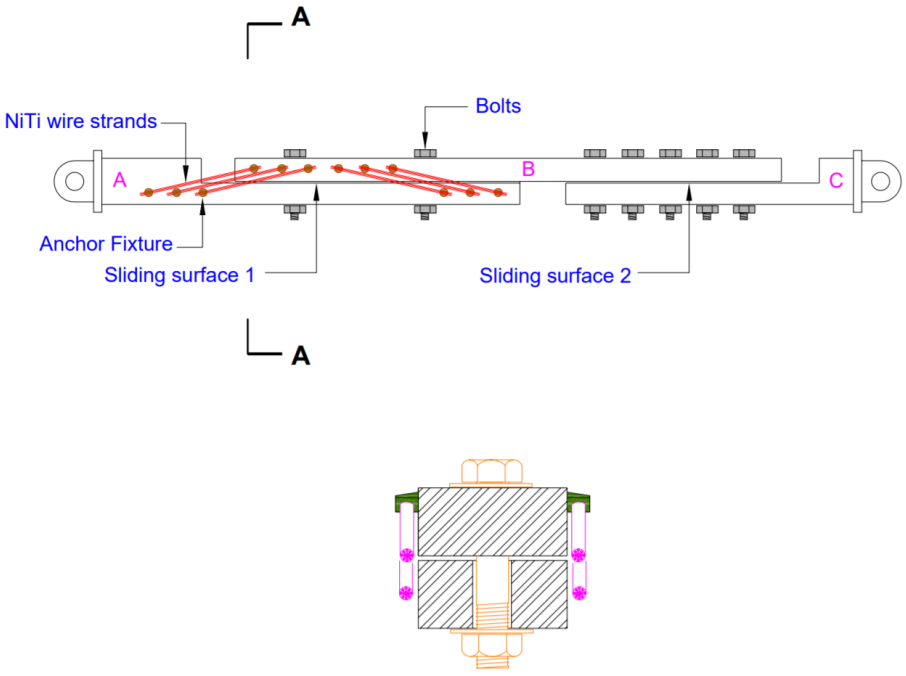

Figure 2-30 Schematic of mechanical configuration of SFDB [100]

An innovative SMA-based damper with full re-centering capability are studied by [101]. As shown in Figure 2-31, the new damper was composed of the pretensioned superelastic SMA wire to contribute energy dissipation, and two precompressed springs to offer re-centering ability. In the damper device, the pretensioned SMA wires and roller system provided a high-energy dissipation capacity, while these springs supplied an expected restoring force to the damper, providing full re-centering capability by altering the precompression applied to the springs. Numerical studies were performed, using the Vrinson's constitutive model for the SMA material, to validate the expected behavior of the damper. The analytical results showed that the meter-long SMA-based damper demonstrated full re-centering capability with the equivalent damping ratio of 0.12, which was obtained when the SMA wire loops revealed a high energy dissipation capacity at 3% pre-strain and 2.8% strain amplitude, to a 30 mm stroke.

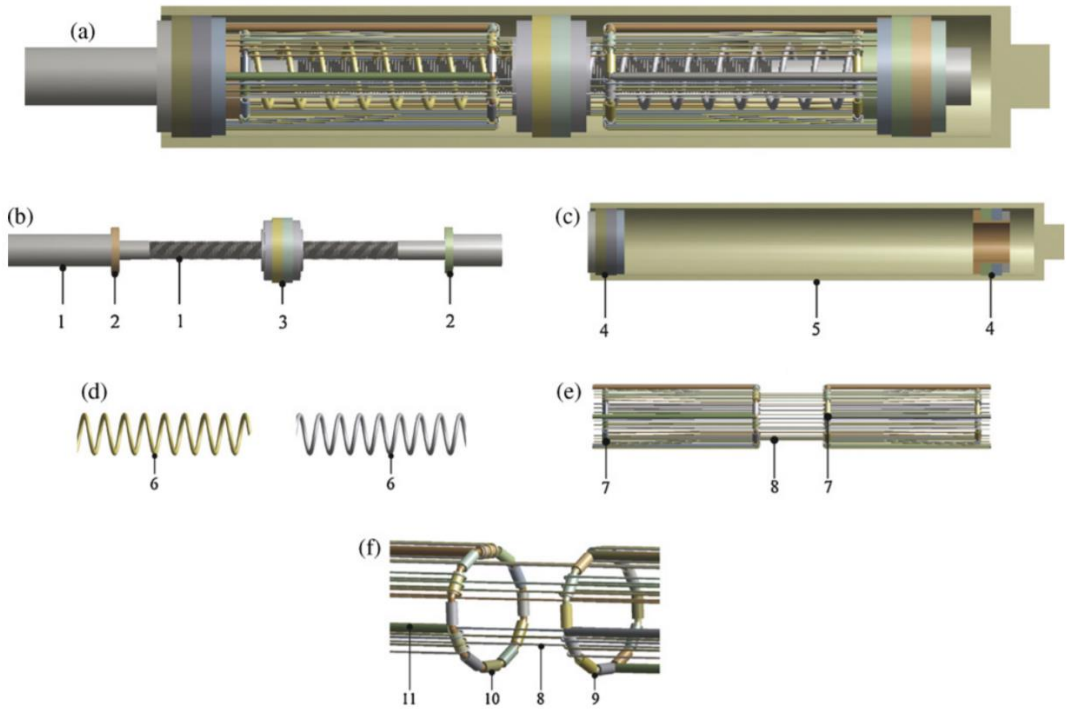

Figure 2-31 . Schematic diagram of the SMA damper: (a) sectional view of the damper; (b) internal shaft group; (c) external tube group; (d) springs; (e) SMA wires group; (f) the connection between SMA wires and roller system. (1) Internal shaft; (2) shim plate; (3) middle anchor; (4) outside anchor; (5) external tube; (6) spring; (7) SMA wire; (8) roller system; (9) roller shaft; (10) roller; (11) stump [101]

The effectiveness of a re-centering shape memory alloy damper (RSMAD) is evaluated by [102] to mitigate the seismic response of structures. The RSMAD was developed utilizing the superelastic Nitinol wires (SMA) as the kernel energy-dissipating component as shown in Figure 2-32. In this study, improved constitutive equations for the superelastic Nitinol wires were proposed, based on the Graesser and Cozzarelli model and validated by the cyclic tensile-compression tests on the dampers, with different prestrains under various loading frequencies and displacements. The results from the experimental test validated the hysteric behavior generated, based on the improved constitutive model, reflecting the martensitic hardening characteristics of SMAs under large amplitudes, with superior performance both in the re-centering and energy-dissipating features under various conditions. In the numerical simulation, a ten-story frame with SMA dampers in five different configurations, and also without the dampers, was investigated, considering different earthquake ground motions, to access the effectiveness of RSMADs for structural seismic protection. The simulation results revealed that the SMA-based dampers were capable of significantly reducing structural vibrations, indicating their effectiveness as an energy-dissipating device.

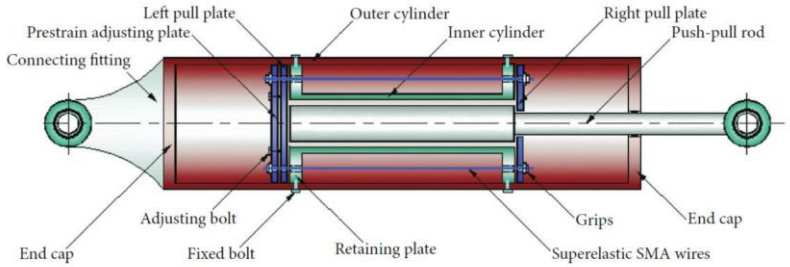

Figure 2- 32 Proposed RSMAD device [102]

An SMA-based hybrid device, which provided the dual characteristics of energy-absorbing and re-centering capabilities is researched by [103], to mitigate structural damage during seismic events. The hybrid damper, shown in Figure 2-33(a) and (b), consisted of three main components: (i) a set of re-centering SMA material; (ii) two energy-absorbing struts- and (iii) two high-strength steel tubes to facilitate the movement of the device. The length of the SMA wires was designed such that their strain reached within the target strain of 6%, which indicated full re-centering capability and avoided the SMA stiffening phase even in the occurrence of large deformations. Furthermore, the energy-absorbing struts were designed to be seismically compact and stocky to

avoid the buckling issue in compression loading. The numerical study of a three-story SAC building was conducted to explore the behavior and performance of the building installed with the hybrid devices in two different configurations: horizontally between a beam and braces of a frame, or utilized simply as a diagonal brace, as shown in Figure 2-33(c) and (d). The results from the numerical study concluded that the SMA-based hybrid dampers contributed performances comparable to the BRBF system in energy dissipation capacity and peak inter-story drift, while also indicating superior re-centering capabilities.

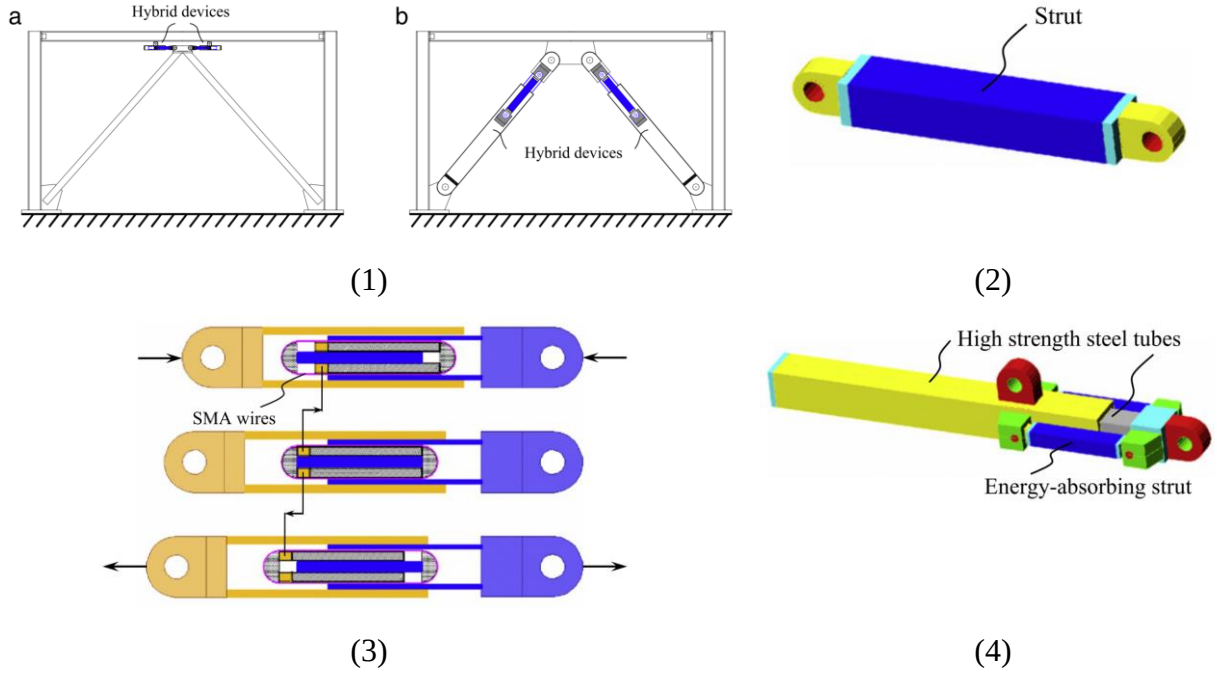

Figure 2-33 (1) Arrangement of hybrid devices: (a) Configuration 1 and (b) Configuration 2 (2) Energy-absorbing strut (3) SMA wires inside a hybrid device with clevis pins for Configuration 2 (4) Overview of a hybrid device with clevis pins for Configuration 1 [103]

The effectiveness of a superelastic shape memory alloy friction damper (SSMAFD) in controlling the seismic response of structures is proposed by [104], through experimental testing of a three-story steel frame building. The SSMAFD was proposed by combining the unique features of pretensioned superelastic SMA wires and friction components, as shown in Figure 2-34. The SMA wires and the integrated friction devices were primarily employed to contribute re-centering ability and energy dissipation ability, respectively. In shake table tests, a quarter-scale building structure was experimentally tested to assess the seismic performance of the device under historical earthquake records. The structural models with or without SSMAFD were analyzed under various earthquake loadings to evaluate their dynamic behaviors in terms of story displacements, inter-

story drift, and story accelerations. The shake table test results revealed that the frame building installed with SSMAFD was capable of controlling the dynamic response of the buildings subjected to strong earthquake events. Furthermore, the SSMAFD demonstrated superior energy dissipation capability with remarkable re-centering ability.

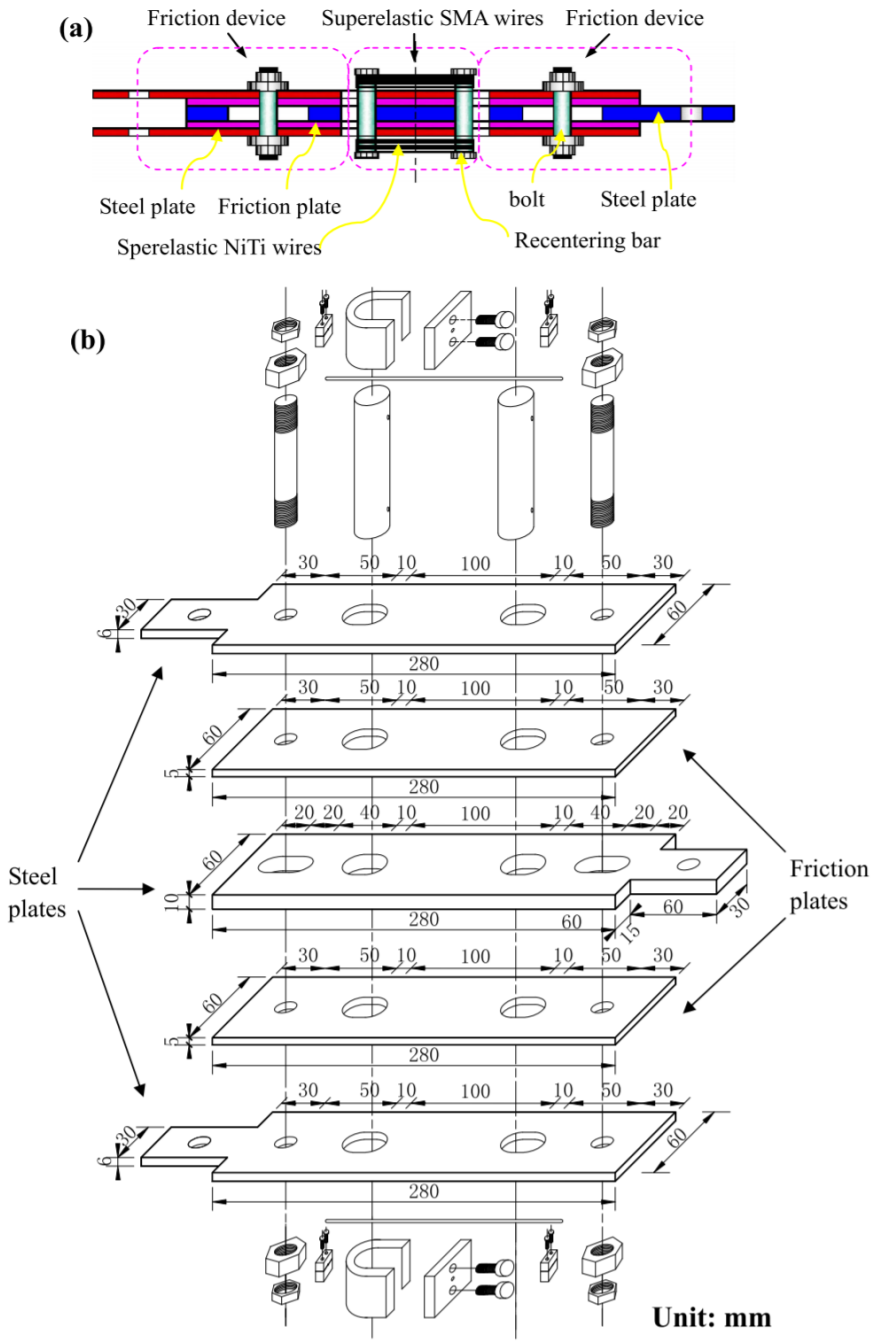

Figure 2-34 Configurations of SSMAFD: (a) scheme diagram of SSMAFD and (b) details of each parts of SSMAFD [104]

The seismic performance of a new *Fe*-based SMA (*Fe-Ni-Co-Al-Ta-B*, entitled FNCATB) damper are numerically explored by [105], as an alternative to Nitinol or *Cu-Al-Be* SMAs. Figure 2-35 illustrates the schematic diagram of the proposed damper. The performance of the superelastic FNCATB damper installed in a single-bay and single-story structural frame was compared with a frame with Nitinol and *Cu-Al-Be*-based devices. The optimal performance of the damper was achieved by selecting the parameters of the damper to maximize its equivalent damping. The force-deformation behavior of the damper was validated by fitting the available experimental test data with a cyclic stress-strain model proposed by the well-known Auricchio model. The numerical results illustrated that structural systems exhibited a superior performance with the proposed FNCATB damper, in terms of reducing story drift. The study concluded that the new FNCATB damper with a *Fe*-based SMA could be a cost-effective alternative because of its ferrous constituent.

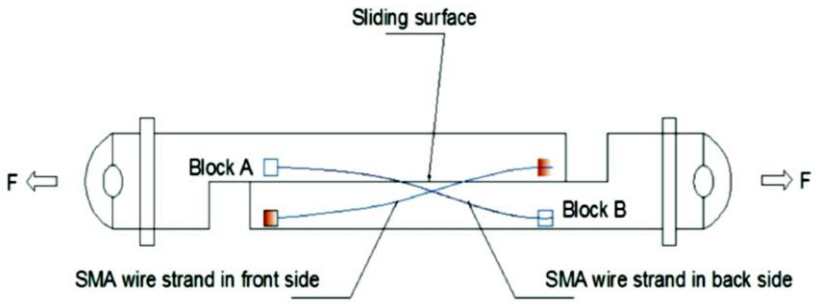

Figure 2-35 Schematic configuration of the superelastic damper [105]

A hybrid passive control device and investigates its performance in improving response of steel frame structures subjected to multi-level seismic hazards is proposed by [106]. The proposed superelastic viscous damper (SVD) relies on shape memory alloy (SMA) cables for re-centering capability and employs a viscoelastic (VE) damper that consists of two layers of a high damped (HD) blended butyl elastomer compound to augment its energy dissipation capacity. The SVD frame effectively reduces the peak inter-story drift ratio at different seismic hazard levels without a considerable increase in the acceleration response. The SVD frame also produces minimal residual drifts even at very high seismic hazard levels. The significantly lower residual drifts observed in the SVD frame indicates that the repair costs of the steel frame buildings with SVD

will be less than that of the conventional SMRF. Overall, the results show the potential of SVDs as a passive seismic control device in improving collapse resistance of steel frame buildings and eliminating the damage under various seismic hazard levels. (Figure 2-36).

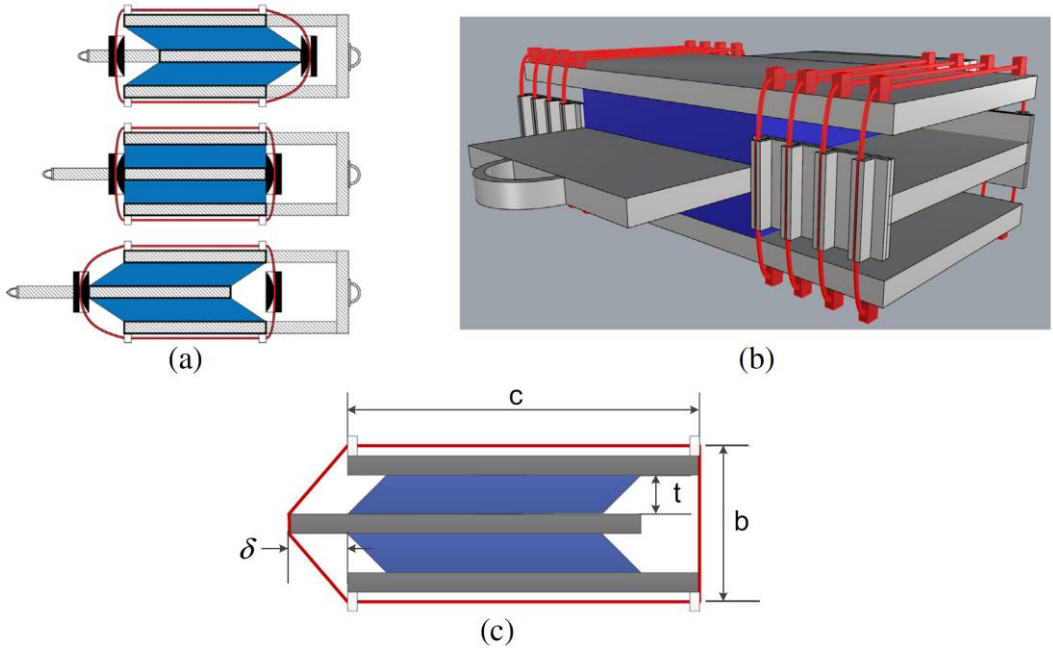

Figure 2-36 (a) A schematic diagram of SVD at its undeformed and deformed positions, (b) 3D rendering of SVD and (c) design parameters for SVD 3D rendering SVD damping device [106]

2.5 Applications of the Friction Spring in civil engineering

Friction springs are indispensable safety components in all fields of technology where suddenly occurring forces have to be taken up and kinetic energy absorbed, or where springs are required with relatively compact dimensions while also being able to sustain high forces. Expert friction springs are needed when it comes to the deceleration of moving masses in a quick, safe and precise manner. Friction springs are all-purpose elements and have a clear advantage over other damping systems. One of the advantages is that, they own ultra-high force capacity which makes them to be promising in damper systems. Friction springs are used wherever high kinetic energies have to be taken up and dampened, or where springs with relatively small dimensions are required for high forces. The range of application for friction springs is very versatile. Basically, they serve three

areas which can also be combined with one another: overload protection, clearance compensation and energy absorption. In the following one of the applications of friction spring will be discussed.

One such new device, based on a self-centering friction mechanism is investigated by [131]. This device uses ring springs, also known as friction springs (Figure 2-37), as the key components to dissipate seismic-induced energy. Results of characterization tests performed on a 200-kN capacity damper prototype and shake table tests on a half-scale moment-resisting steel frame equipped with the same damper prototype are presented. Results of the shake table tests are also compared with numerical predictions. The results of the characterization tests showed that the force-displacement hysteresis loops of the damper were self-centering, repeatable, stable, identical in tension-compression, and nearly identical for all frequencies considered. In the shake table tests, the damper was effective in reducing the lateral displacements of the test structure. The damper was also efficient in reducing acceleration levels under earthquake intensity that caused slight yielding of the structure without a damper. The schematic view of the device can be seen in Figure 2-38.

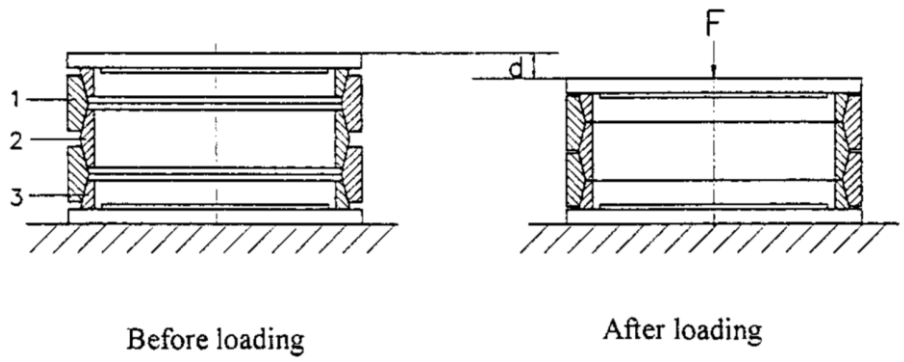

Figure 2-37 Friction Spring Details. 1-Outer Ring; 2-Inner Ring; 3-Inner Half Ring [131]

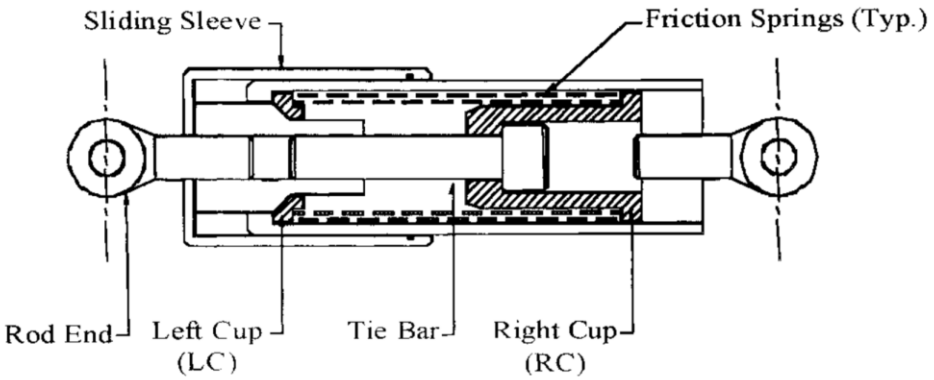

Figure 2-38 Diagrammatic View of Seismic Damper [131]

2.6 Closure

In this chapter a review of the SMA materials are carried out. Various types of the SMA materials as well as their general characterizations are introduced and compared to each other. Mechanical properties of the SMA materials plus their test sensitivity toward load rating load, temperature, and cyclic load are explored. A new kind of SMA bar material named as NiTiHfPd is introduced. New SMA material's advantages compare to other SMA materials show that NiTiHfPd SMA is a promising candidate for replacing old SMA materials in term of owning ultra-force capacity, good cycling behavior and excellent temperature tolerance. At the end of the chapter vast civil engineering applications of SMA materials were illustrated. It can be predicted that SMA based materials especially new NiTiHfPd SMA material will be promising to be utilized more often in passive structural control systems for its ultra-dissipating energy capacity.

3 Experimental Testing and Finite Element simulations

3.1 Introduction

In addition to the immediate structural response to a dynamic event, the amount of residual deformation, once motion has stopped, is an important metric to evaluate building post-event performance. Due to its inherent re-centering ability, shape memory alloys (SMAs) have been extensively studied over the past decade to develop self-centering structural systems [106-110]. Although the shape memory phenomenon has been observed in a variety of alloys, due its excellent ductility and shape memory properties near equatomic NiTi (49-51 at% Ni) is known as the workhorse of research and applications in SMA related studies. However, NiTi has some limitations such as limited material strength and damping capacity and unsatisfactory shape memory properties (e.g. low recoverable strain) at high stress levels and elevated temperatures [36-38]. A recently developed class of SMAs that consists of NiTiHfPd provides large energy dissipation and high stresses [25] and can overcome the deficiency of currently available SMAs. Figure 3-1 presents typical strain-stress diagrams of NiTi and NiTiHfPd SMAs at room temperature. It can be seen that the area captured within the hysteresis loop, which signifies the dissipated energy, for NiTiHfPd is considerably larger than that of NiTi. The strength of NiTiHfPd is also significantly higher than that of NiTi. Thus, the required cross-sectional area of the SMA elements to develop the design force of a damping device will be considerably smaller for NiTiHfPd.

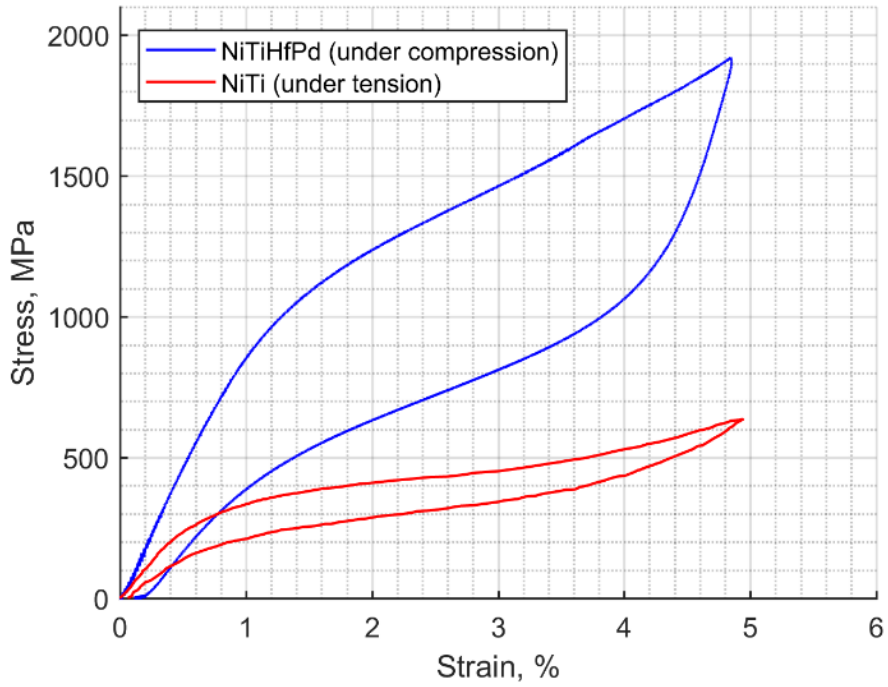

Figure 3-1 Strain-stress diagrams for NiTi and NiTiHfPd at temperature room and loading frequency of 1.0 Hz

3.2 High Damping and High Strength NiTiHfPd SMAs

NiTi SMAs have been studied and employed in a variety of applications due to their superior shape memory properties, corrosion resistance, biocompatibility, ductility, etc. However, they have certain limitations that restrict their functionality for some applications. Alloying is one of the most effective ways to engineer properties and overcome these problems. For instance, an SMA material with good damping capacity needs to have large mechanical hysteresis and transformation strain at high-stress levels to be employed as dampers. While the mechanical hysteresis and damping capacity of binary NiTi alloys has been reported to be 200-400 MPa and 16 $J.cm^{-3}$ respectively [50], with the addition of Nb it can be increased to 500-600 MPa and 38 $J.cm^{-3}$ [49]. The addition of elements like Zr, Hf, and Pd also has been studied to improve strength, wear resistance and damping capacity of SMAs. Due to its low cost, medium ductility and higher work output, the addition of Hf to NiTi binary found to be the promising [51-52]. However, one of the main challenges that should be addressed before NiTiHf alloys can be used in practical applications is their brittleness. Therefore, the addition of a variety of quaternary elements to NiTiHf has been

explored in the literature. For example, the addition of Cu to NiTiHf has been found to shrink thermal hysteresis, improve thermal stability, ductility and two-way shape memory effect but no other substantial change has been observed for other shape memory properties of the alloy [111-112]. The addition of Pd as a quaternary element to NiTiHf alloy has resulted in a significant improvement in the ductility, adjustment of TTs or enhance the shape memory behavior. Toward this goal, Pd can be added in the expense of Ti to increase the transformation temperatures or at the expense of Ni improves superelasticity. Single crystalline NiTiHfPd alloy has been reported to show huge mechanical hysteresis of up to 1270MPa, superelastic response under extremely high-stress levels (2.5GPa), and damping capacity of 44 J cm^{-3} [25, 29, 113] Even polycrystalline NiTiHfPd alloys can generate high work outputs of 32-35 J cm^{-3} (up to 120 ºC), which are considerably higher than NiTi and Ni. The ultra-high-strength, and the exceptional damping capacity and practical ability to demonstrate superelastic behavior at room temperature makes NiTiHfPd SMAs a great candidate for applications that require high damping. Besides the alloying, other most common methods to improve the shape memory and mechanical properties of SMAs are thermomechanical processing (e.g. cold working and post-annealing), precipitate formation, and grain refinement of polycrystalline alloys. However, thermal treatments seem to the most practical and cost-effective method amongst the others. It has been shown that by the formation of precipitates through aging, the strength of the matrix and required critical stress are increased which results in better shape memory response, the fatigue life, and cyclic stability. It should be noted that the strengthening ability of the precipitates depends on the size, volume fraction, antiparticle spacing, and coherency of these particles [114].

3.3 Material Characterization

For experiment characterization, Ni-rich single [111] oriented single crystal Ni45.3Ti29.7Hf20Pd5 (at %) and polycrystal Ni45.7Ti29.3Hf20Pd5 (at %) alloys obtained from NASA. In collaboration with department of mechanical engineering' researchers at the University of Kentucky, two different SMA specimens are used for experimental tests. First sample named NiTiHfPd 3rdB-400C-3hr with the height of 7.76 mm and cross section of 3.68x3.78mm^2 (Sample 1). The second sample named NiTiHfPd SC [111] 400C-3hr with the height of 7.71 mm and cross section of 3.84x3.85mm^2 (Sample 2). The sample is heat treated at 400 ºC for 3 hours and then water quenched before testing. Heating–cooling rate was adjusted to 10 ºC/min. Aging of the samples

was performed using Lindberg/Blue M BF514541 furnace in air atmosphere and then water quenched. The mechanical experiments were performed in an MTS Landmark servo-hydraulic test platform (100 kN) on compression specimens cut by electro-discharge machining. The strain was measured by an MTS high-temperature extensometer with a gage length of 12 mm attached to compression grip faces. Loading and unloading are conducted at the selected frequencies of 0.05, 0.5 and 1Hz and temperatures of-55 ^{o}C, -35 ^{o}C, -15 ^{o}C, 5 ^{o}C and 25 ^{o}C for one set of specimens. Also, Loading and unloading are conducted at the selected frequencies of 0.05, 0.5 and 1Hz and temperatures of 0^{o}C, 20 ^{o}C and 40 ^{o}C for another set of specimens. Heating of the specimens was occurred by means of mica band heaters retrofitted to the compression grips, and cooling was achieved through internal liquid nitrogen flow in the compression grips. A heating–cooling rate of 10 ^{o}C/min was applied during testing, using an Omega CN8200 series PID temperature controller. K-type thermocouples attached to the test specimens and the compression grips provided real-time temperature feedback.

3.4 Experimental Testing results of NiTiHfPd SMAs

3.4.1 Strain-Stress curves of NiTiHfPd-SC-(111)-400C-3hr-rate specimen (Sample 2)

Figure (3-2) to (3-6) show strain-stress curves of NiTiHfPd-SC-(111)-400C-3hr-rate specimen SMAs at -55°C, -35 °C, -15°C, 5 °C and 25 °C, respectively. The curves at each temperature are plotted for the tests conducted at different strain amplitudes and different loading frequencies. It can be seen that the hysteresis loops of NiTiHfPd SMAs move upward with increasing temperature. In addition, when temperature decreases from +25 °C to -55 °C, the hysteresis loops tend to have a wider area. This indicates that energy dissipation of the SMA increases with a decrease in temperature. Increasing loading frequency also shifts hysteresis loops upward, yet, it does not change the area of hysteresis loops considerably.

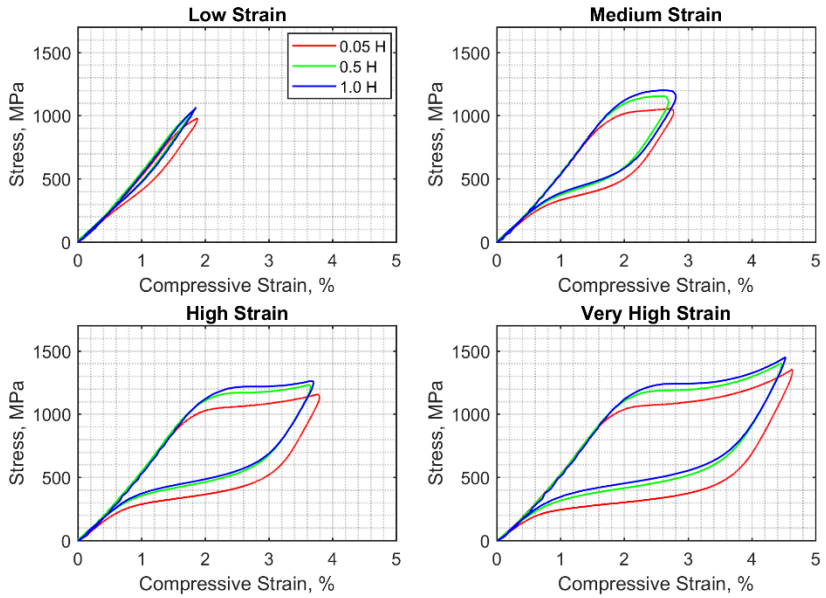

Figure 3-2 Stress-strain curves of NiTiHfPd-SC-(111)-400C-3hr-rate specimen SMAs at the temperature of -55°C with various strain and loading frequency levels

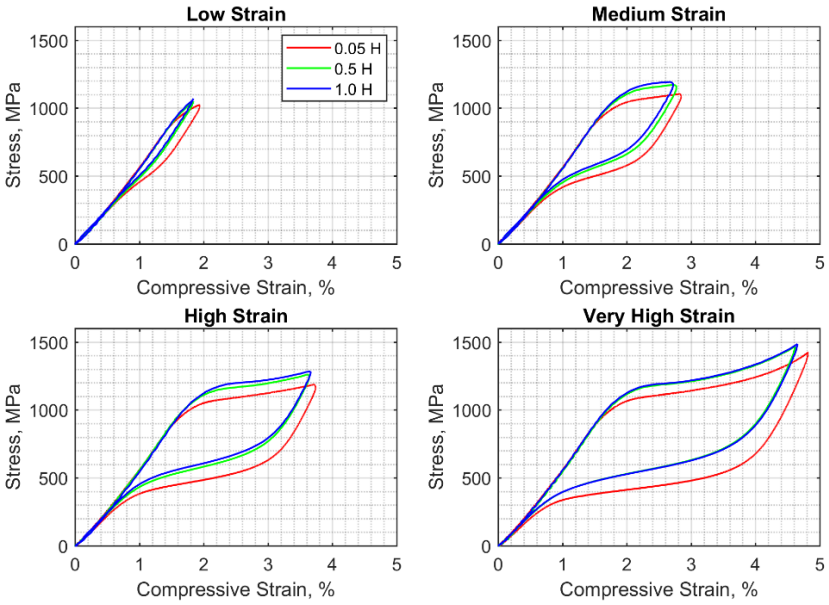

Figure 3-3 Stress-strain curves of NiTiHfPd-SC-(111)-400C-3hr-rate specimen SMAs at the temperature of -35°C with various strain and loading frequency levels

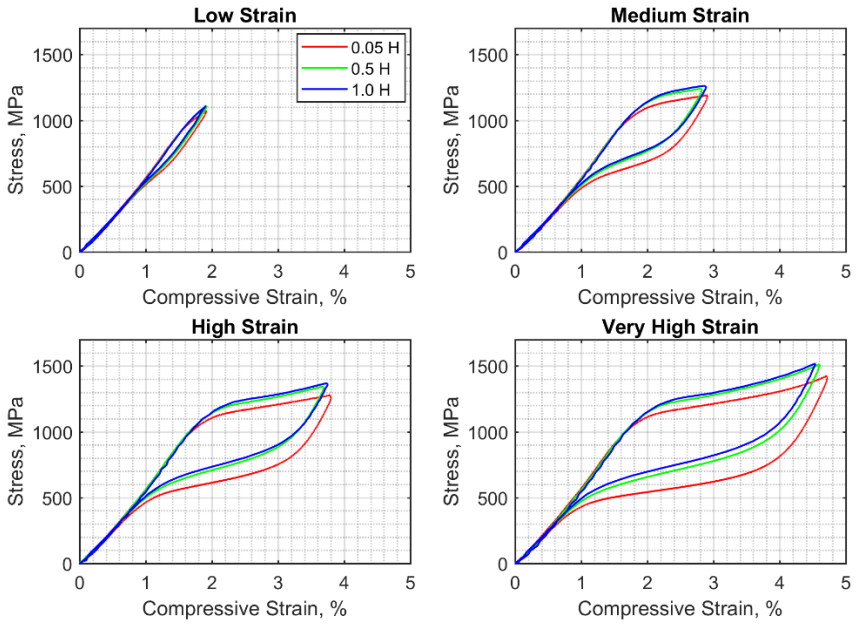

Figure 3-4 Stress-strain curves of NiTiHfPd-SC-(111)-400C-3hr-rate specimen SMAs at the temperature of -15°C with various strain and loading frequency levels

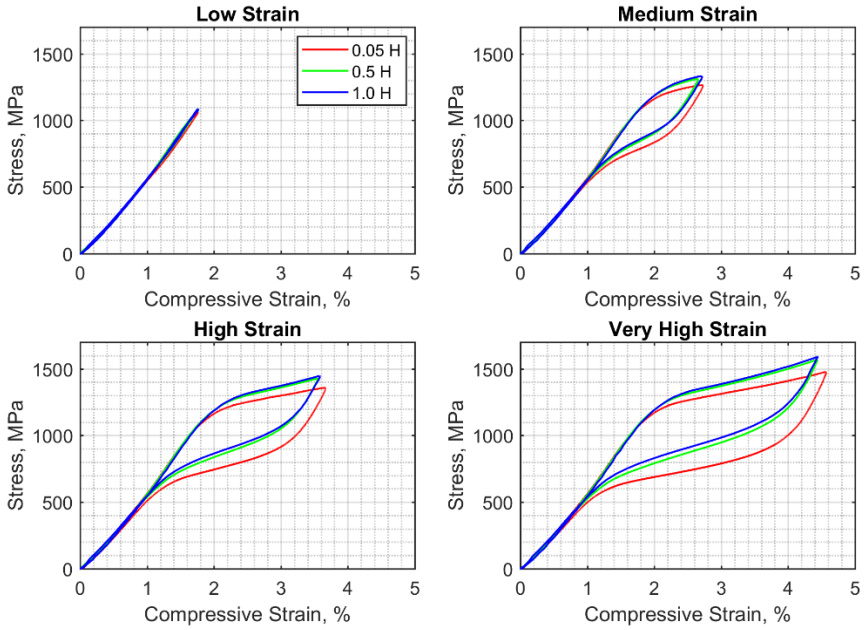

Figure 3-5 Stress-strain curves of NiTiHfPd-SC-(111)-400C-3hr-rate specimen SMAs at the temperature of +5°C with various strain and loading frequency levels

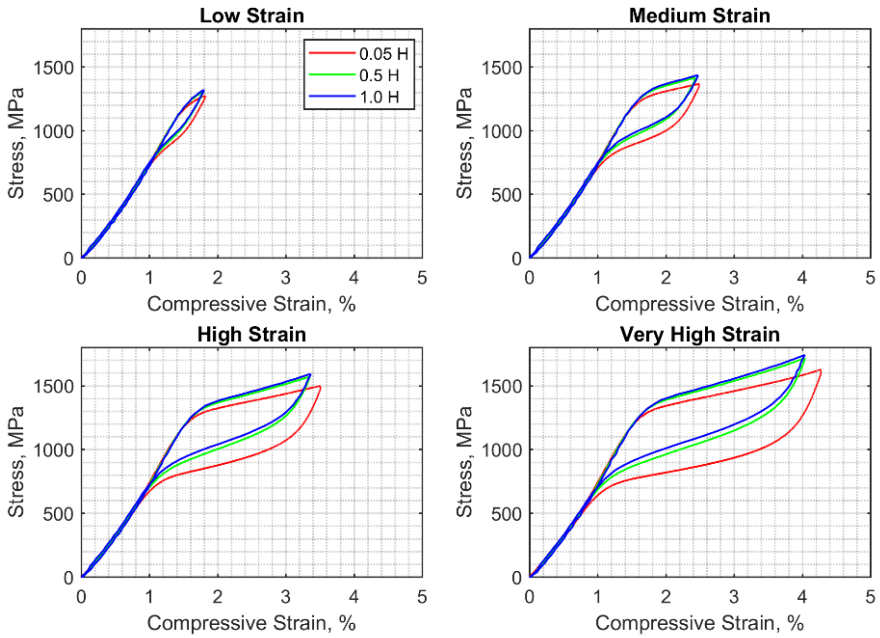

Figure 3-6 Stress-strain curves of NiTiHfPd-SC-(111)-400C-3hr-rate specimen SMAs the temperature of +25°C with various strain and loading frequency levels

Figure (3-7) to (3-9) show strain-stress curves of NiTiHfPd SMAs at rating load 0.05 H, 0.5 H and 1.0 H. It can be seen that the hysteresis loops of NiTiHfPd SMAs move upward with increasing temperature. Increasing loading frequency shifts hysteresis loops upward, yet, it does not change the area of hysteresis loops.

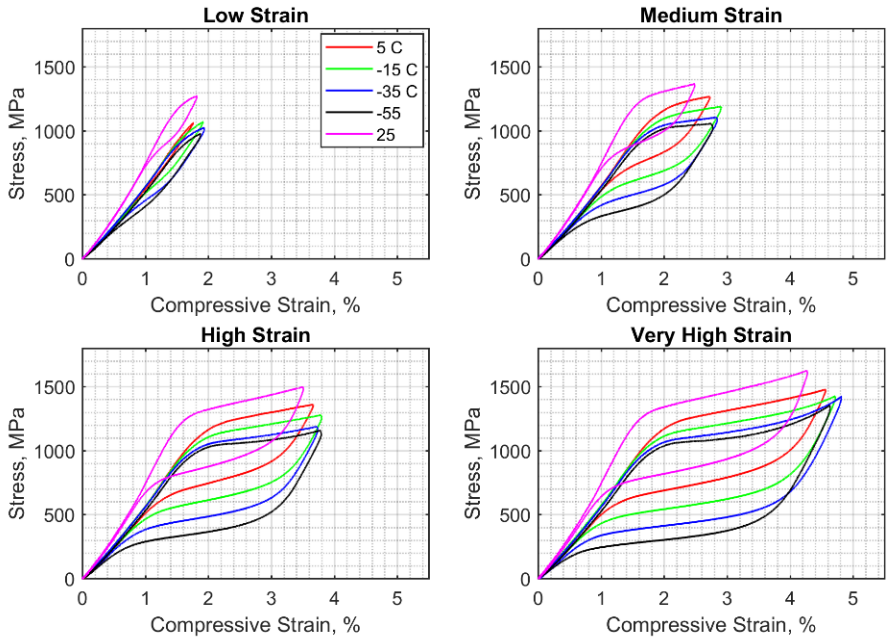

Figure 3-7 Stress-strain curves of NiTiHfPd-SC-(111)-400C-3hr-rate specimen SMAs at the loading frequency of 0.05 H with various strain and temperatures

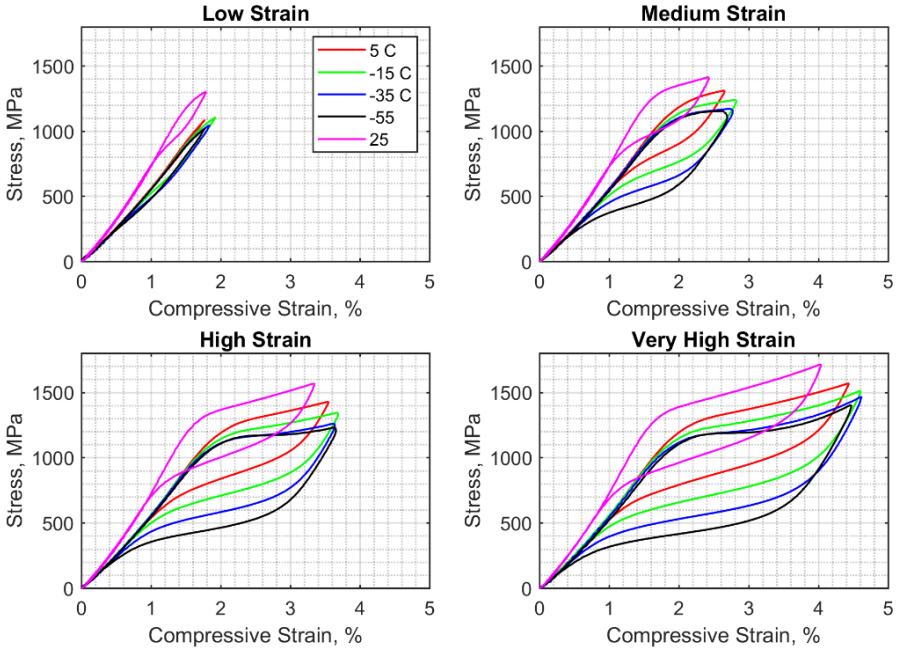

Figure 3-8 Stress-strain curves of NiTiHfPd-SC-(111)-400C-3hr-rate specimen SMAs at the loading frequency of 0.5 H with various strain and temperatures

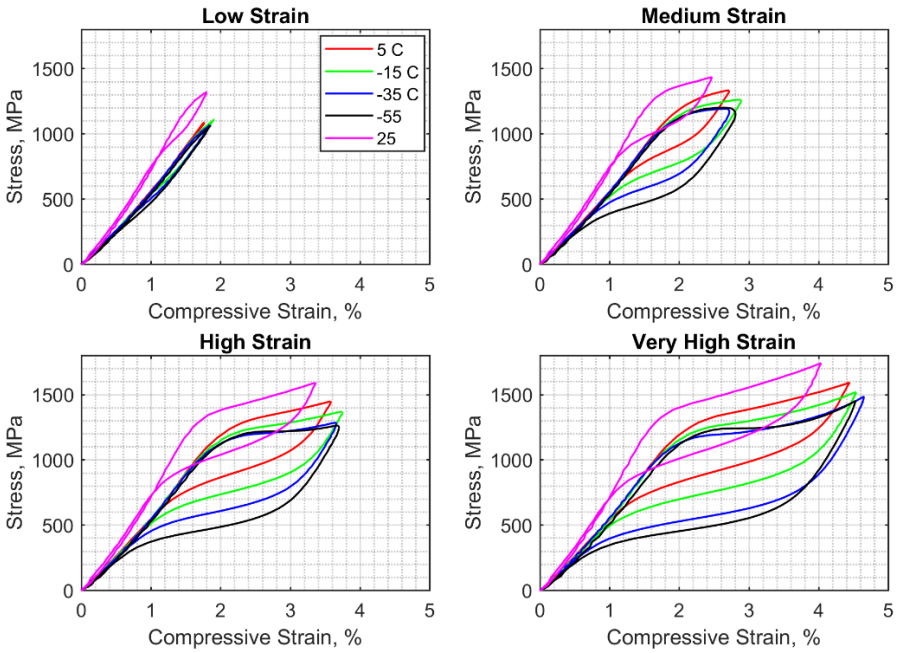

Figure 3-9 Stress-strain curves of NiTiHfPd-SC-(111)-400C-3hr-rate specimen SMAs at the loading frequency of 1.0 H with various strain and temperatures

3.4.2 Strain-Stress curves of NiTiHfPd-3rdB-400C-3hr-rate tests specimen (Sample 1)

Figure (3-10) to (3-12) show strain-stress curves of NiTiHfPd-3rdB-400C-3hr-rate tests specimen SMAs at 0 °C, 20 °C and 40 °C, 5 °C respectively.

The curves at each temperature are plotted for the tests conducted at different strain amplitudes and different loading frequencies. It can be seen that the hysteresis loops of NiTiHfPd SMAs move upward with increasing temperature. In addition, when temperature decreases from 0 °C to 40 °C, the hysteresis loops tend to have a wider area. This indicates that energy dissipation of the SMA increases with a decrease in temperature.

Figure (3-13) to (3-15) show strain-stress curves of NiTiHfPd SMAs at rating load 0.05 H, 0.5 H and 1.0 H. It can be seen that the hysteresis loops of NiTiHfPd SMAs move upward with increasing temperature. Increasing loading frequency shifts hysteresis loops upward, yet, it does not change the area of hysteresis loops.

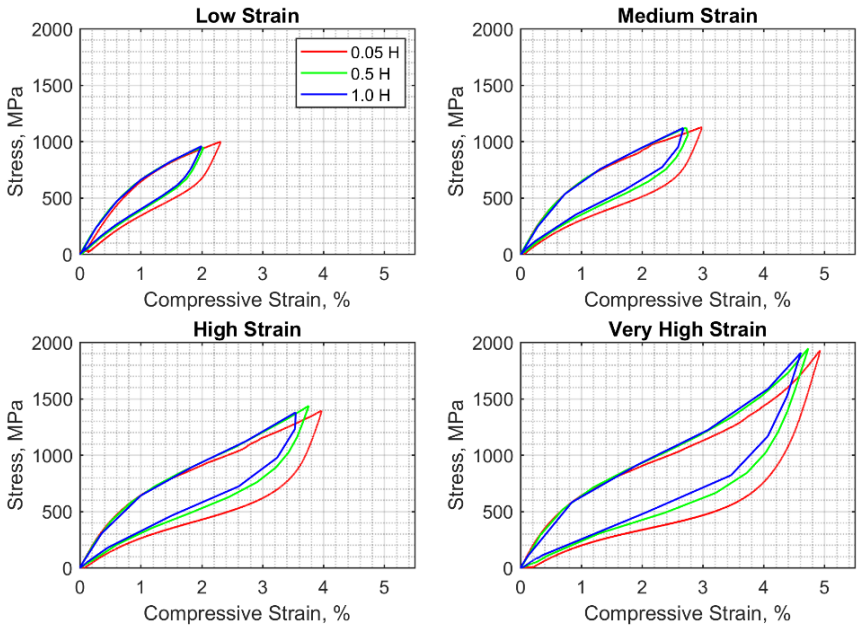

Figure 3-10 Stress-strain curves of NiTiHfPd-3rdB-400C-3hr-rate specimen SMAs the temperature of 0°C with various strain and loading frequency levels

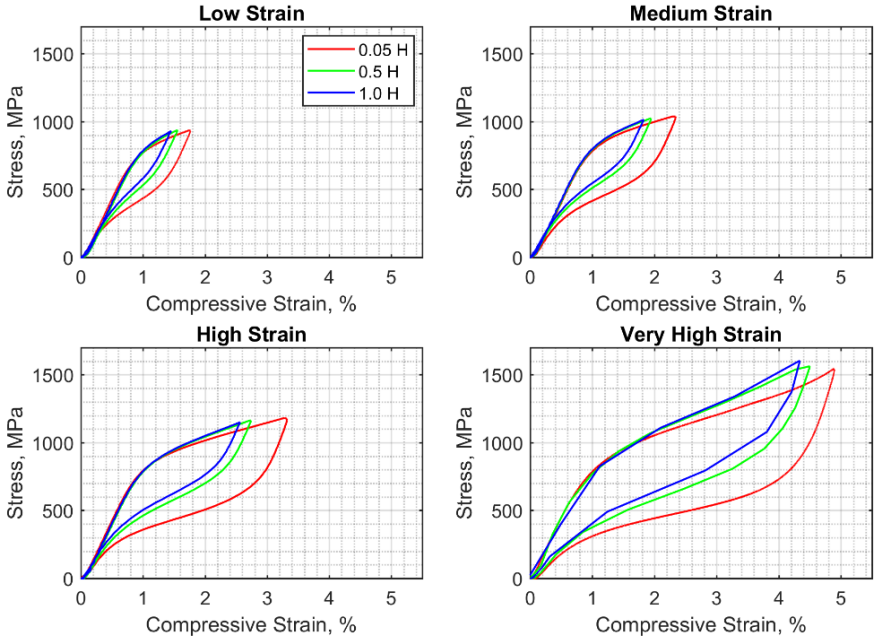

Figure 3-11 Stress-strain curves of NiTiHfPd-3rdB-400C-3hr-rate specimen SMAs the temperature of +20°C with various strain and loading frequency levels

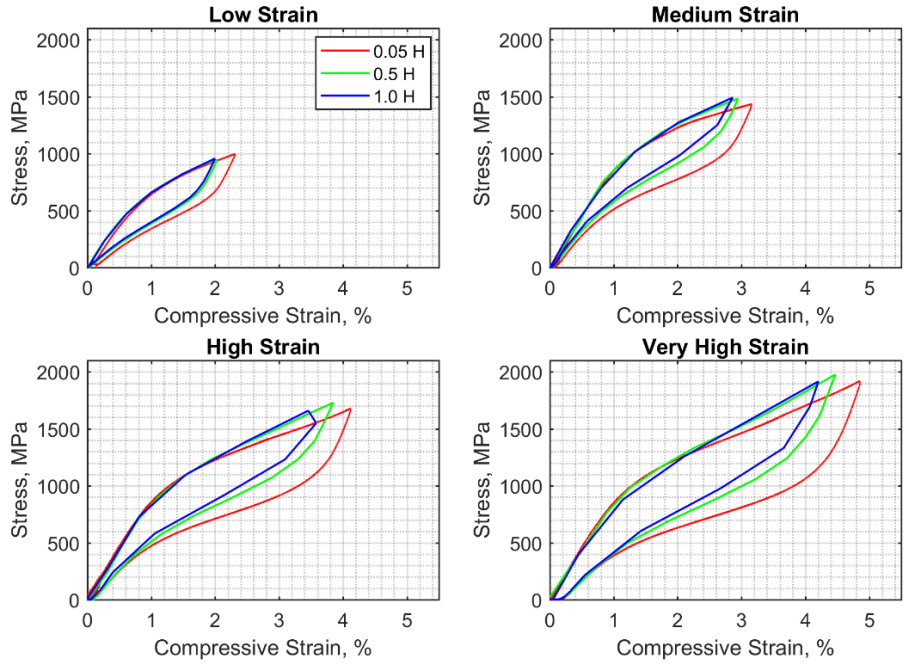

Figure 3-12 Stress-strain curves of NiTiHfPd-3rdB-400C-3hr-rate specimen SMAs the temperature of 40°C with various strain and loading frequency levels

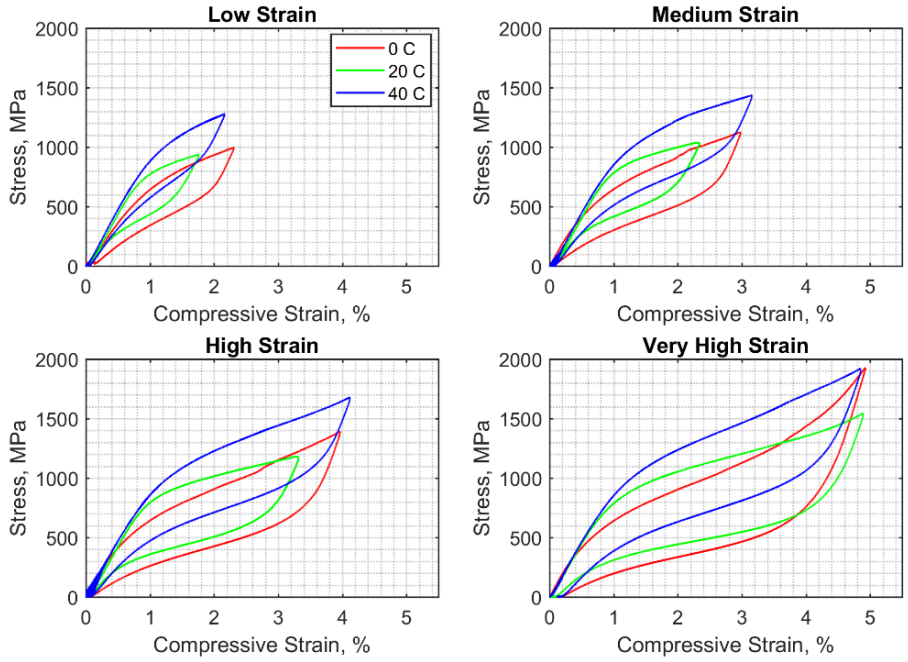

Figure 3-13 Stress-strain curves of NiTiHfPd-3rdB-400C-3hr-rate specimen SMAs at the loading frequency of 0.05 H with various strain and temperatures

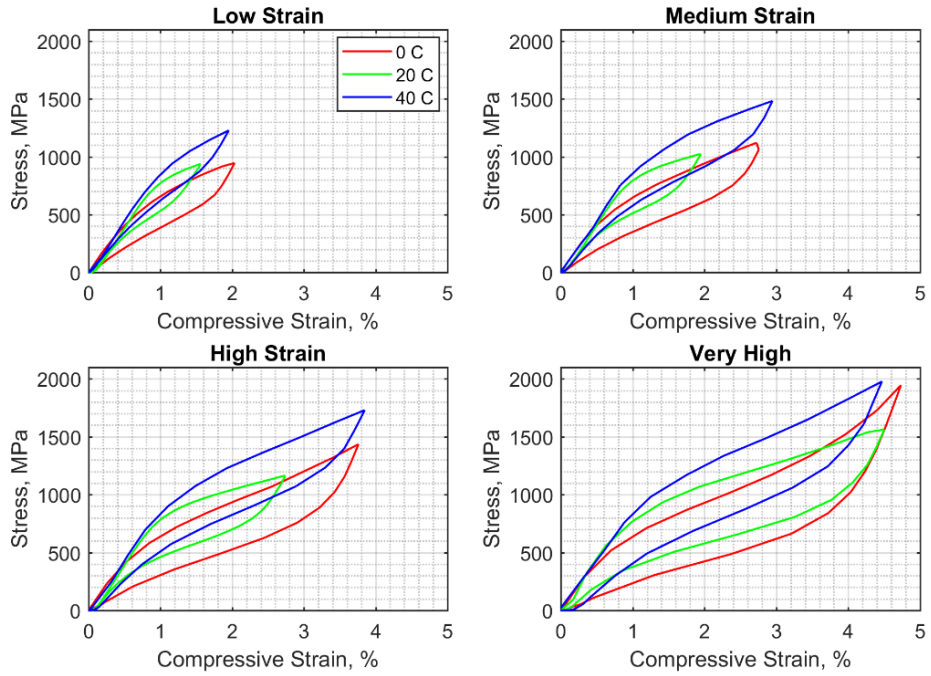

Figure 3-14 Stress-strain curves of NiTiHfPd-3rdB-400C-3hr-rate specimen SMAs at the loading frequency of 0.5 H with various strain and temperatures

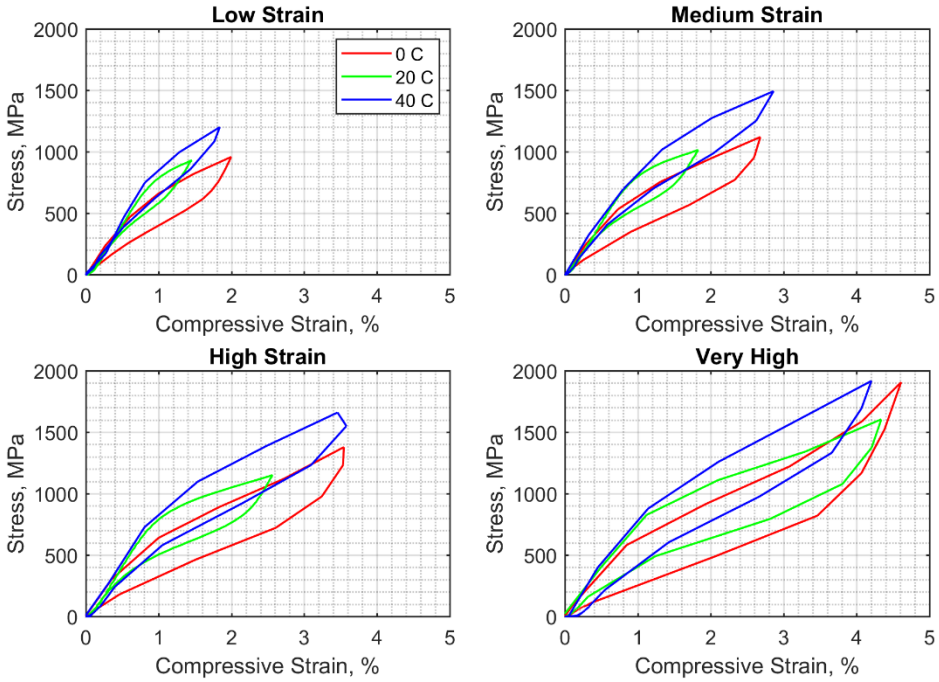

Figure 3-15 Stress-strain curves of NiTiHfPd-3rdB-400C-3hr-rate specimen SMAs at the loading frequency of 1.0 H with various strain and temperatures

3.5 Some important mechanical properties of NiTiHfPd SMA specimens

In order to enable the assessment of the test results in a more quantative way, some important mechanical proporties, including the equivalent (secant) stiffness, K_e, the energy dissipation per cycle, E_D, and the equivalent viscous damping ratio, ξ_{eqv} are calculated. The equivalent viscous damping ratio and the equivalent (secant) stiffness are defined as:

$$\xi_{eqv} = \frac{E_D}{4\pi E_S} \tag{3-1}$$

$$K_e = \frac{F_{max} - F_{min}}{D_{max} - D_{min}} \tag{3-2}$$

Where E_S is the maximum elastic strain energy for the same cycle; and F_{max} and F_{min} are the maximum and minimum forces obtained for the maximum and minimum cyclic deformation D_{max} and D_{min}.

3.5.1 Force-deformation curves of NiTiHfPd-SC-(111)-400C-3hr-rate specimen (Sample 2)

In order to calculate the mechanical properties of SMA specimens Force-Deformation plots should be obtained. Figure (3-16) to (3-20) show force-deformation curves of NiTiHfPd-SC-(111)-400C-3hr-rate specimen SMAs at -55°C, -35 °C, -15°C, +5 °C and +25 °C, respectively. The curves at each temperature are plotted for the tests conducted at different displacement amplitudes and different loading frequencies.

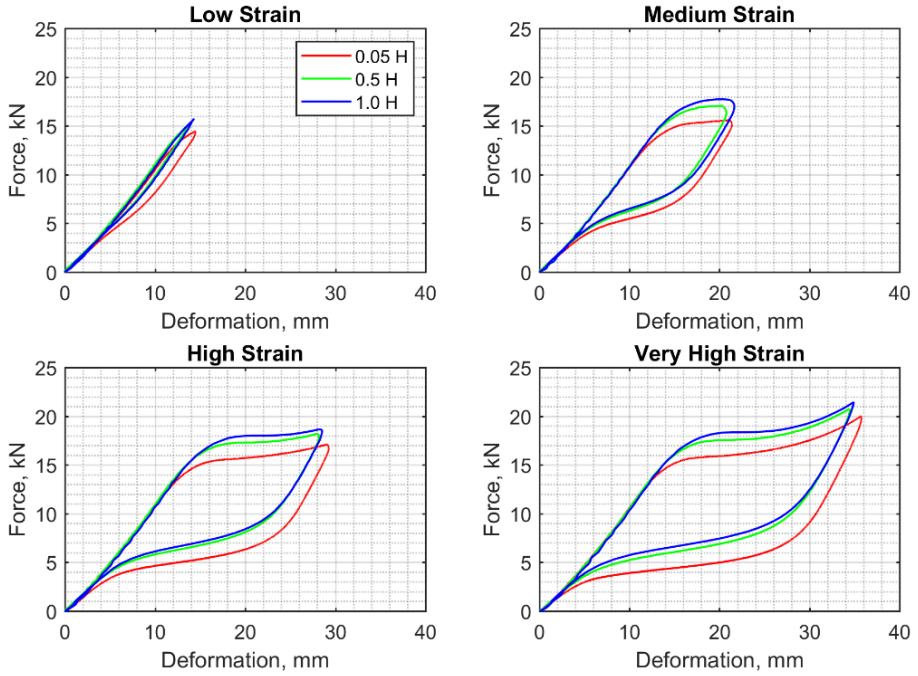

Figure 3-16 Force-deformation curves of NiTiHfPd-SC-(111)-400C-3hr-rate specimen SMAs at the temperature of -55°C with various strain and loading frequency levels

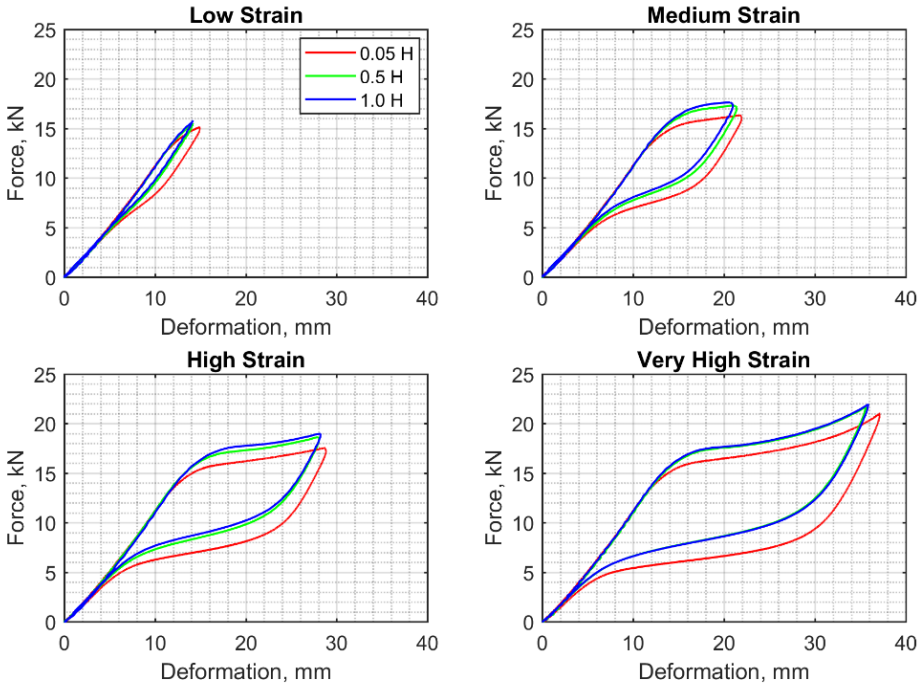

Figure 3-17 Force-deformation curves of NiTiHfPd-SC-(111)-400C-3hr-rate specimen SMAs at the temperature of -35°C with various strain and loading frequency levels

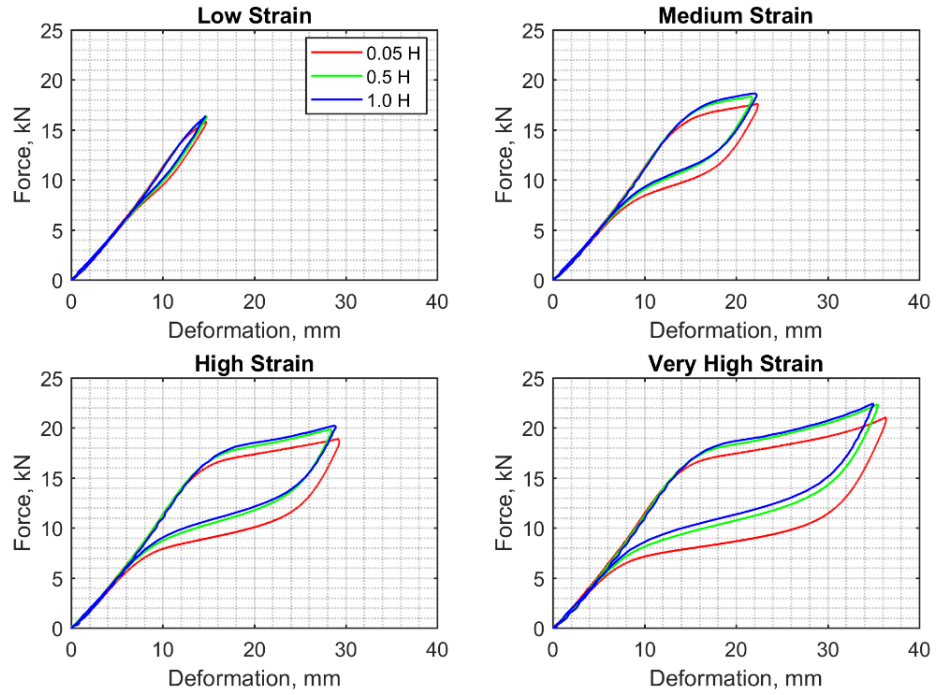

Figure 3-18 Force-deformation curves of NiTiHfPd-SC-(111)-400C-3hr-rate specimen SMAs at the temperature of -15°C with various strain and loading frequency levels

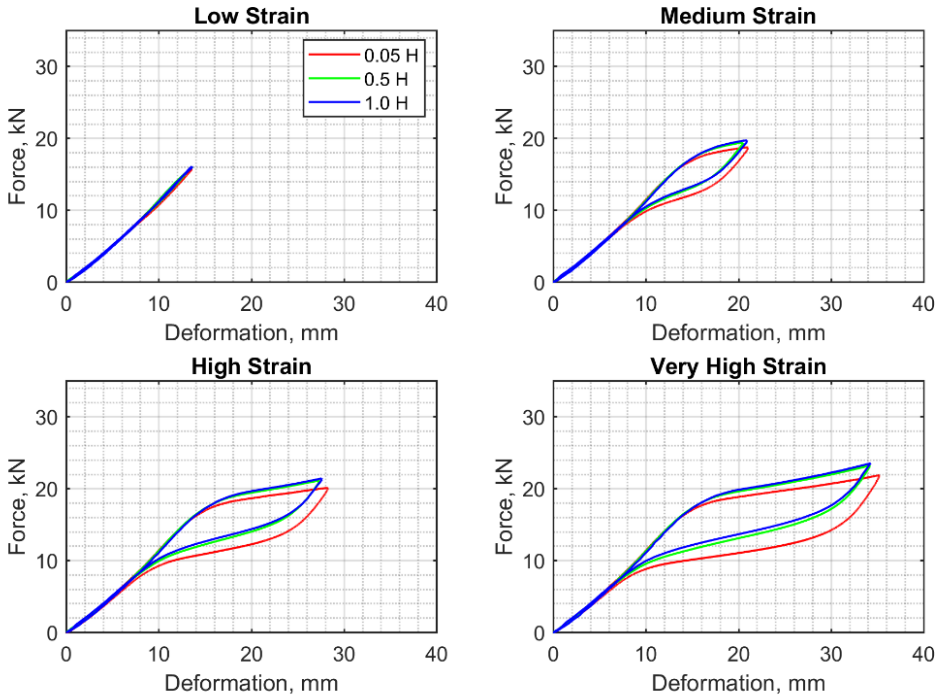

Figure 3-19 Force-deformation curves of NiTiHfPd-SC-(111)-400C-3hr-rate specimen SMAs at the temperature of 5°C with various strain and loading frequency levels

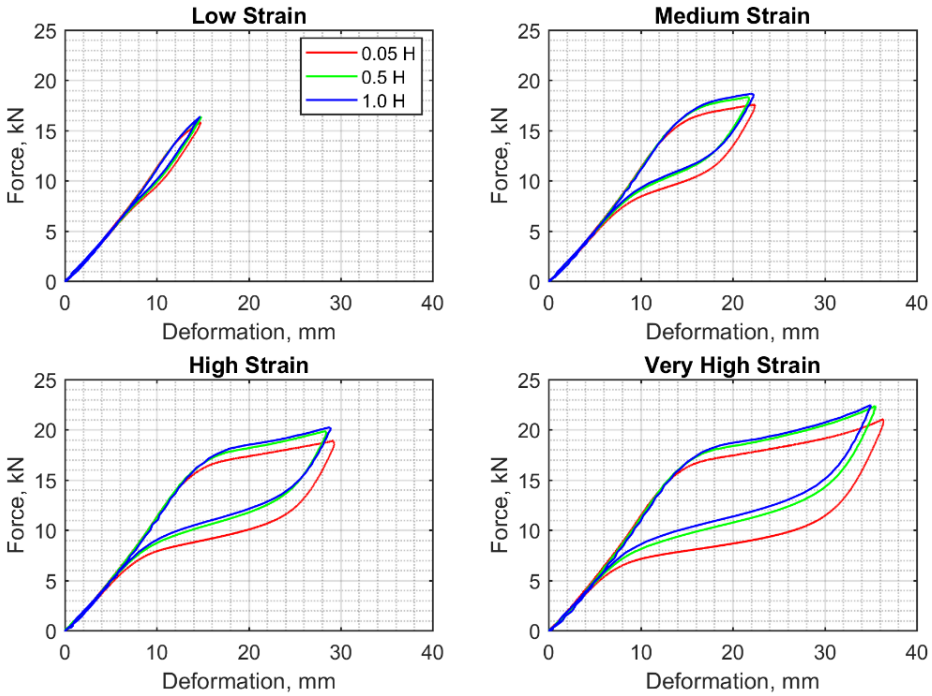

Figure 3-20 Force-deformation curves of NiTiHfPd-SC-(111)-400C-3hr-rate specimen SMAs at the temperature of +25°C with various strain and loading frequency levels

3.5.2 Force-deformation curves of NiTiHfPd-3rdB-400C-3hr-rate specimen (Sample 1)

Figure (3-21) to (3-23) show force-deformation curves of NiTiHfPd-3rdB-400C-3hr-rate specimen SMAs at 0°C, 20 °C and 40 °C, respectively. The curves at each temperature are plotted for the tests conducted at different displacement amplitudes and different loading frequencies.

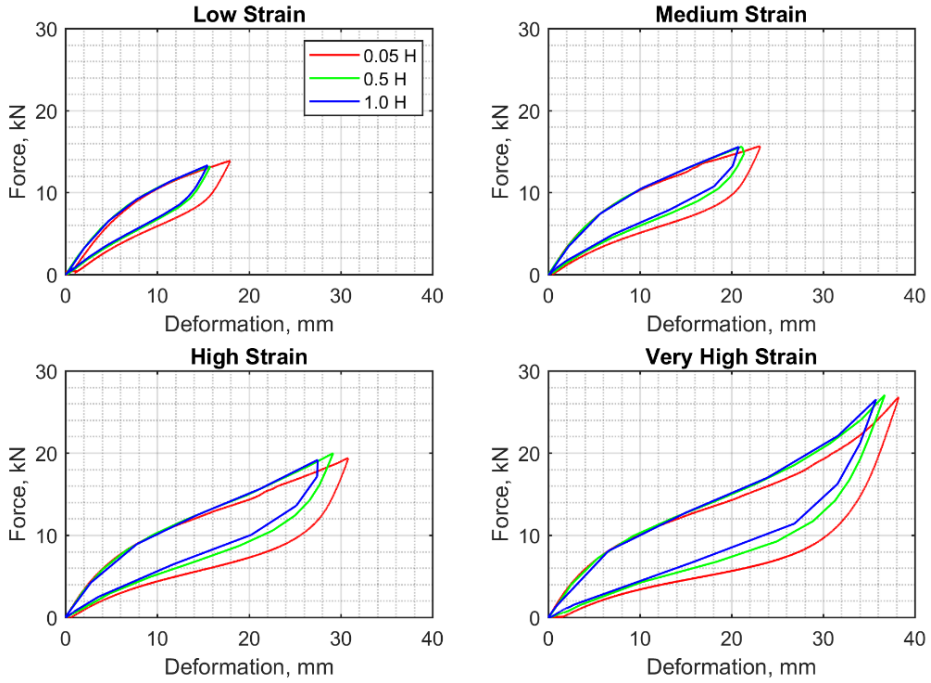

Figure 3-21 Force-deformation curves of NiTiHfPd-3rdB-400C-3hr-rate specimen SMAs at the temperature of 0°C with various strain and loading frequency levels

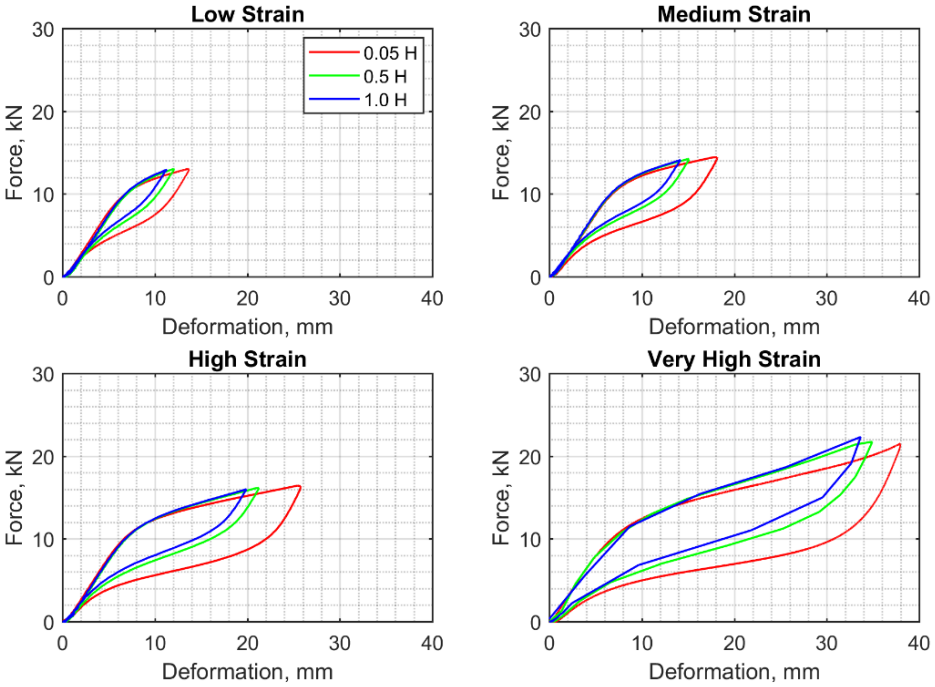

Figure 3-22 Force-deformation curves of NiTiHfPd-3rdB-400C-3hr-rate specimen SMAs at the temperature of 20°C with various strain and loading frequency levels

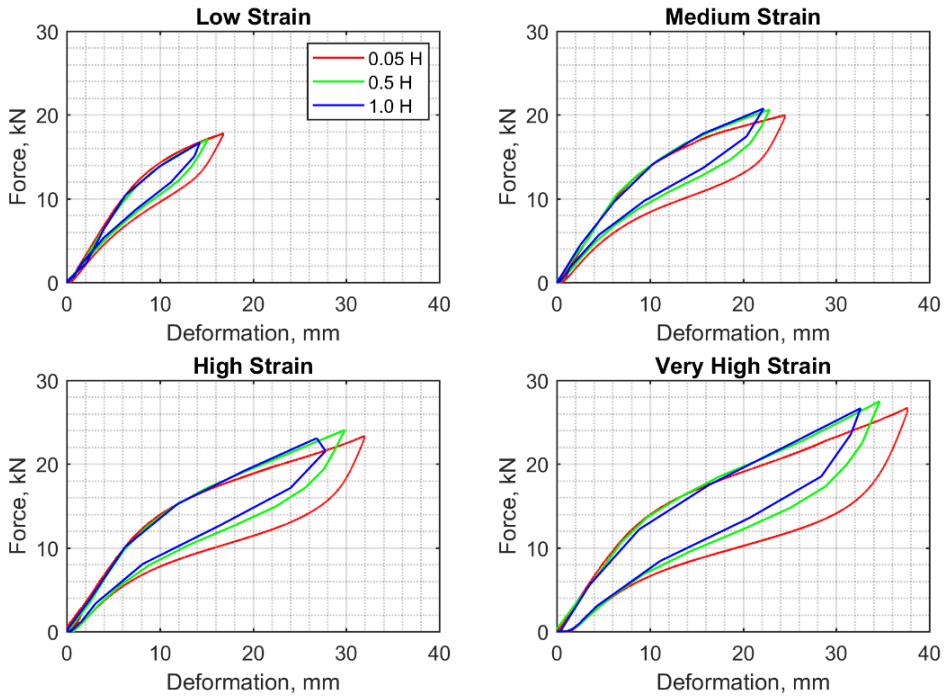

Figure 3-23 Force-deformation curves of NiTiHfPd-3rdB-400C-3hr-rate specimen SMAs at the temperature of +40°C with various strain and loading frequency levels

3.5.3 Energy dissipation per cycle, equivalent viscous damping with temperature for NiTiHfPd-3rdB-400C-3hr-rate specimen (Sample 1)

In this section, some important mechanical properties of NiTiHfPd-3rdB-400C-3hr-rate specimen are obtained in order to compare their mechanical properties with variation of temperature and loading rate frequency. Figure (3-24) to (3-25) show bar plots of Equivalent Viscous Damping (EVD) for SMA specimens with variation of temperature and loading rate frequency.

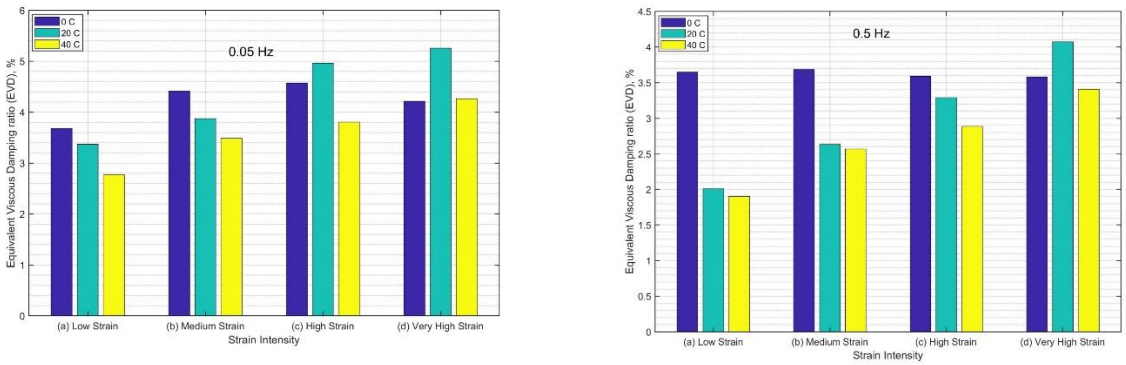

(a) (b)

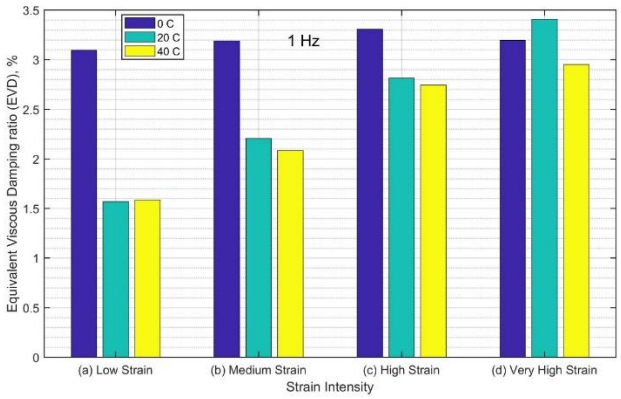

(c)

Figure 3-24 Variation of equivalent viscous damping with temperature for (a) 0.05H, (b) 0.5H and (c) 1.0 H for the NiTiHfPd-3rdB-400C-3hr-rate specimen

Figure 3-24 shows the variation of equivalent viscous damping with temperature for the tests conducted at different loading frequencies. It can be seen that the equivalent viscous damping generally decreases with increasing temperature. It also worth mentioning that, generally the equivalent viscous damping for the loading rate frequency of 0.05H is larger than two other frequencies. Figure 3-25 shows variation of the equivalent viscous damping with different levels of strain from low to very high strain. Figure 3-25 indicates that the equivalent viscous damping of the specimens goes up with increasing strain level. This can be related to the fact that, when specimens undergo larger strain, at the same time the loop of the flag shape changes to be bigger and consequently the equivalent viscous damping tends to be larger in higher strains. Tables (3-1) to (3-3) show energy dissipation, energy stored and equivalent viscous damping of the specimens.

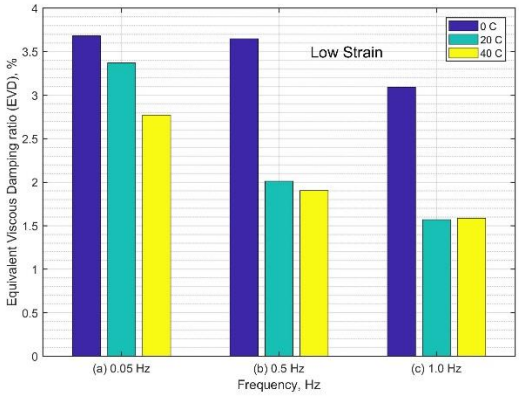

(a)

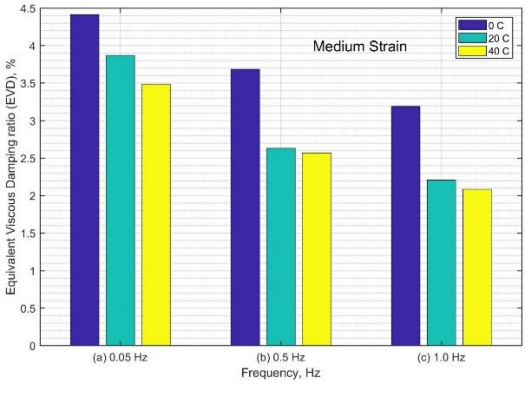

(b)

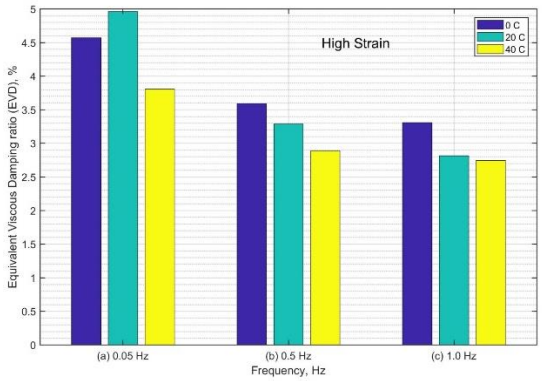

(c)

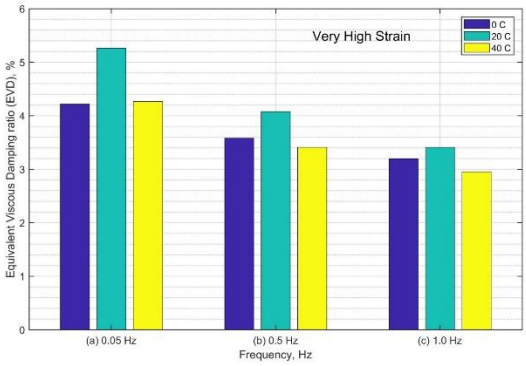

(d)

Figure 3-25 Variation of equivalent viscous damping with temperature and loading rate frequency for (a) Low Strain, (b) Medium Strain and (c) High Strain, and (d) Very High Strain for the NiTiHfPd-3rdB-400C-3hr-rate specimen

Table 3-1 Calculations of the mechanical properties of sample 1 for temperature 0 °C

Strain level	0 °C					
	Different Strain level	Dissipation Energy(kJ)	Different Strain level	Stored Energy(kJ)	EVD	EVD%
Low Strain	ADL1	57.392	ASL1	124.0758	0.0368277	3.68277
	ADL2	47.5355	ASL2	103.7337	0.03648451	3.648451
	ADL3	40.0521	ASL3	103.075	0.03093729	3.093729
Med Strain	ADM1	99.4653	ASM1	179.335	0.04415876	4.415876
	ADM2	76.3236	ASM2	164.853	0.03686144	3.686144
	ADM3	64.8042	ASM3	161.72	0.03190434	3.190434
High Strain	ADH1	171.008	ASH1	297.7965	0.0457201	4.57201
	ADH2	131.4704	ASH2	291.4352	0.03591669	3.591669
	ADH3	109.5402	ASH3	263.5917	0.0330866	3.30866
Very High Strain	ADVH1	271.5439	ASVH1	512.6608	0.04217162	4.217162
	ADVH2	223.4363	ASVH2	496.9569	0.0357969	3.57969
	ADVH3	190.5078	ASVH3	474.4958	0.03196618	3.196618

Table 3-2 Calculations of the mechanical properties of sample 1 for temperature +20 °C

Strain level	+20 °C					
	Different Strain level	Dissipation Energy(kJ)	Different Strain level	Stored Energy(kJ)	EVD	EVD%
Low Strain	ADL1	37.4752	ASL1	88.5573	0.03369225	3.369225
	ADL2	19.8781	ASL2	78.65	0.02012271	2.012271
	ADL3	14.4072	ASL3	73.0626	0.01569983	1.569983
Med Strain	ADM1	63.6859	ASM1	130.916	0.0387312	3.87312
	ADM2	35.5154	ASM2	107.4106	0.0263257	2.63257
	ADM3	27.737	ASM3	100.0747	0.02206711	2.206711
High Strain	ADH1	131.1992	ASH1	210.4714	0.04963048	4.963048
	ADH2	70.9524	ASH2	171.7707	0.03288731	3.288731
	ADH3	56.3281	ASH3	159.2264	0.02816569	2.816569
Very High Strain	ADVH1	268.5134	ASVH1	406.4688	0.05259556	5.259556
	ADVH2	194.4615	ASVH2	379.8855	0.04075597	4.075597
	ADVH3	160.8366	ASVH3	375.8018	0.03407504	3.407504

Table 3-3 Calculations of the mechanical properties of sample 1 for temperature +40 °C

Strain level	+40 °C					
	Different Strain level	Dissipation Energy (kJ)	Different Strain level	Stored Energy (kJ)	EVD	EVD%
Low Strain	ADL1	52.0238	ASL1	149.3951	0.02772529	2.772529
	ADL2	30.9803	ASL2	129.4705	0.01905132	1.905132
	ADL3	23.7497	ASL3	119.2059	0.01586247	1.586247
Med Strain	ADM1	106.8655	ASM1	244.1004	0.03485615	3.485615
	ADM2	76.0268	ASM2	235.6866	0.02568279	2.568279
	ADM3	60.3327	ASM3	230.5398	0.02083614	2.083614
High Strain	ADH1	178.1541	ASH1	372.6103	0.03806723	3.806723
	ADH2	130.2869	ASH2	359.1999	0.02887852	2.887852
	ADH3	106.8135	ASH3	309.6182	0.02746692	2.746692
Very High Strain	ADVH1	268.9926	ASVH1	502.0981	0.04265423	4.265423
	ADVH2	204.1621	ASVH2	476.9127	0.03408369	3.408369
	ADVH3	161.233	ASVH3	434.9916	0.02951097	2.951097

3.5.4 Energy dissipation per cycle, equivalent viscous damping, and equivalent stiffness with temperature for the NiTiHfPd-SC-(111)-400C-3hr-rate specimen (Sample 2)

In this section, some important mechanical properties of NiTiHfPd-SC-(111)-400C-3hr-rate specimen are obtained in order to compare their mechanical properties with variation of temperature and loading rate frequency. Figure (3-26) to (3-27) show bar plots of Equivalent Viscous Damping (EVD) for SMA specimens with variation of temperature and loading rate frequency.

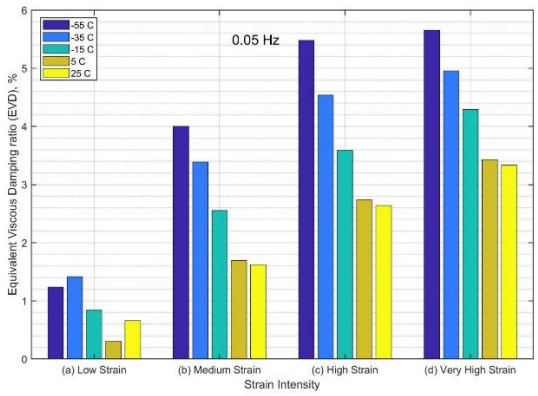

(a)

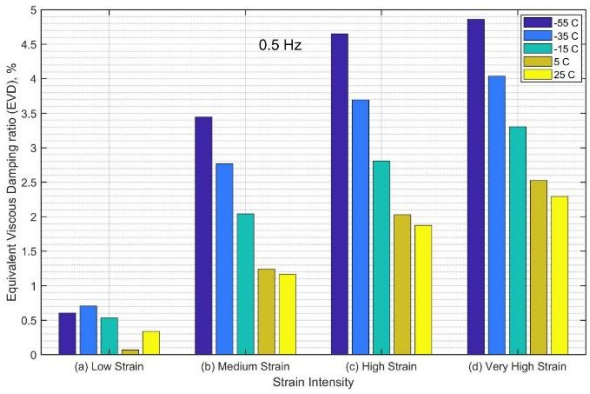

(b)

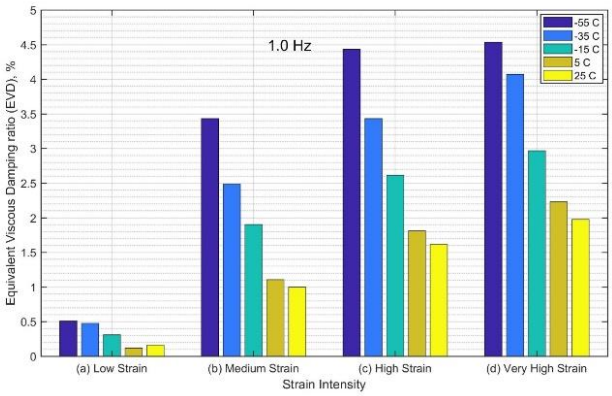

(c)

Figure 3-26 Variation of equivalent viscous damping with temperature for (a) 0.05H, (b) 0.5H and (c) 1.0 H for the NiTiHfPd-SC-(111)-400C-3hr-rate specimen

Figure 3-26 shows the variation of equivalent viscous damping with temperature for the tests conducted at different loading frequencies. It can be seen that the equivalent viscous damping

generally decreases with increasing temperature. It also worth mentioning that, generally the equivalent viscous damping for the loading rate frequency of 0.05H is larger than two other frequencies. Figure 3-27 also shows variation of the equivalent viscous damping with different levels of strain from low to very high strain. Figure 3-27 indicates that the equivalent viscous damping of the specimens goes up with increasing strain level. This can be related to the fact that, when specimens undergo larger strain, at the same time the loop of the flag shape changes to be bigger and consequently the equivalent viscous damping tends to be larger in higher strains. Tables (3-4) to (3-8) show energy dissipation, energy stored and equivalent viscous damping of the specimens.

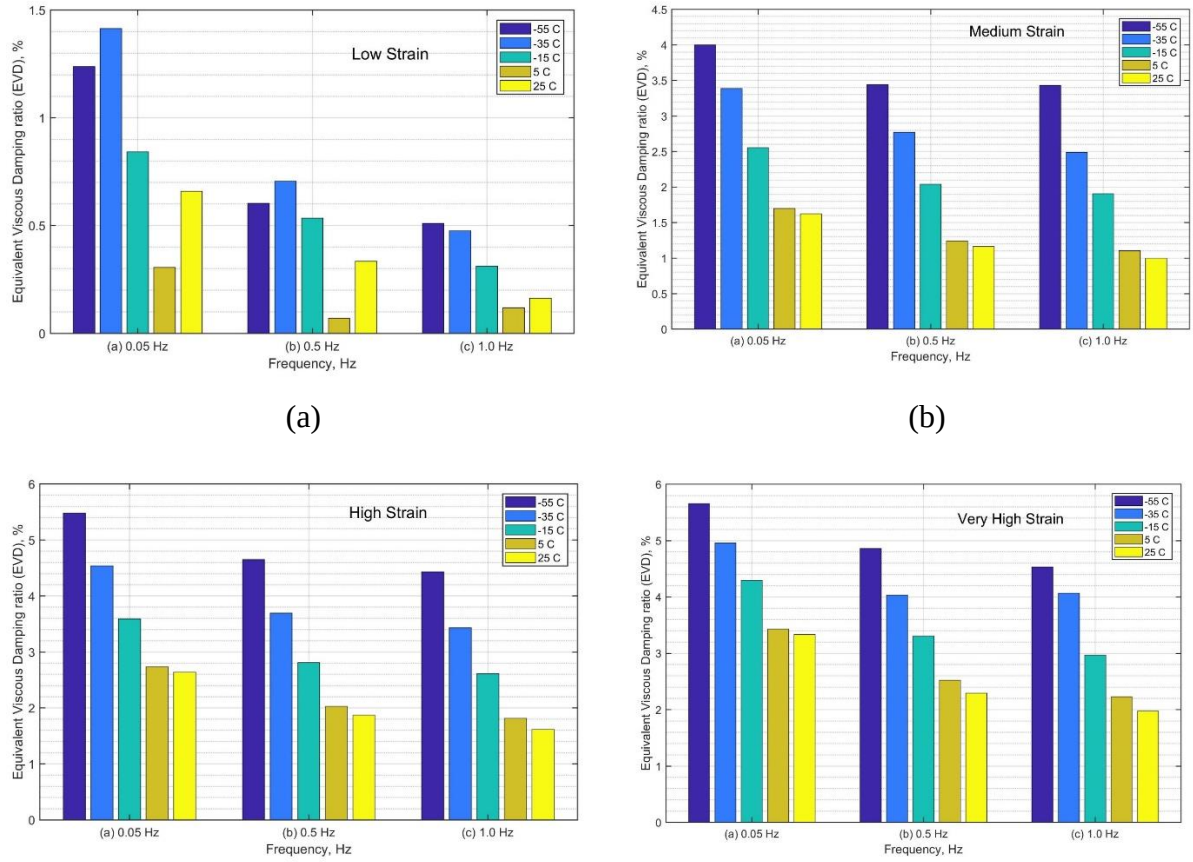

Figure 3-27 Variation of equivalent viscous damping with temperature and loading rate frequency for (a) Low Strain, (b) Medium Strain and (c) High Strain, and (d) Very High Strain for the NiTiHfPd-SC-(111)-400C-3hr-rate specimen

Table 3-4 Calculations of the mechanical properties of sample 2 for temperature -55 °C

Strain level	-55°C					
	Different Strain level	Dissipation Energy	Different Strain level	Stored Energy (kJ)	EVD	EVD%
Low Strain	ADL1	16.3081	ASL1	104.835	0.01238533	1.238533
	ADL2	7.8202	ASL2	103.1184	0.00603799	0.603799
	ADL3	7.2093	ASL3	112.4836	0.00510287	0.510287
Med Strain	ADM1	82.5888	ASM1	164.3295	0.04001437	4.001437
	ADM2	74.2195	ASM2	171.561	0.0344437	3.44437
	ADM3	80.012	ASM3	185.6487	0.03431418	3.431418
High Strain	ADH1	169.6467	ASH1	246.5376	0.05478638	5.478638
	ADH2	149.1407	ASH2	255.3381	0.04650406	4.650406
	ADH3	147.7634	ASH3	265.4775	0.04431487	4.431487
V High Strain	ADVH1	253.5245	ASVH1	356.8428	0.05656572	5.656572
	ADVH2	218.0539	ASVH2	357.0404	0.04862469	4.862469
	ADVH3	213.4471	ASVH3	374.7315	0.04535033	4.535033

Table 3-5 Calculations of the mechanical properties of sample 2 for temperature -35 °

Strain level	-35 °C					
	Different Strain level	Dissipation Energy	Different Strain level	Stored Energy (kJ)	EVD	EVD%
Low Strain	ADL1	20.0978	ASL1	113.0967	0.01414845	1.414845
	ADL2	9.7023	ASL2	109.417	0.00705993	0.705993
	ADL3	6.7065	ASL3	112.251	0.00475681	0.475681
Med Strain	ADM1	75.1853	ASM1	176.617	0.03389306	3.389306
	ADM2	63.5875	ASM2	182.7775	0.0276987	2.76987
	ADM3	57.1763	ASM3	182.9982	0.02487595	2.487595
High Strain	ADH1	142.4712	ASH1	249.9267	0.0453863	4.53863
	ADH2	120.6295	ASH2	260.0685	0.03692973	3.692973
	ADH3	115.4413	ASH3	267.8078	0.03432008	3.432008
V High Strain	ADVH1	242.4823	ASVH1	389.469	0.04956984	4.956984
	ADVH2	195.4909	ASVH2	385.5865	0.04036594	4.036594
	ADVH3	201.3738	ASVH3	393.8526	0.04070799	4.070799

Table 3-6 Calculations of the mechanical properties of sample 2 for temperature -15 °C

Strain level	-15 °C					
	Different Strain level	Dissipation Energy	Different Strain level	Stored Energy (kJ)	EVD	EVD%
Low Strain	ADL1	12.3808	ASL1	117.073	0.00841981	0.841981
	ADL2	8.185	ASL2	121.7853	0.00535099	0.535099
	ADL3	4.7235	ASL3	120.5568	0.00311948	0.311948
Med Strain	ADM1	63.168	ASM1	196.8232	0.02555237	2.555237
	ADM2	50.9654	ASM2	198.8636	0.02040471	2.040471
	ADM3	49.5023	ASM3	206.9613	0.01904349	1.904349
High Strain	ADH1	123.8147	ASH1	274.6464	0.03589291	3.589291
	ADH2	99.5845	ASH2	282.1248	0.02810353	2.810353
	ADH3	95.1753	ASH3	289.8786	0.02614078	2.614078
V High Strain	ADVH1	205.3191	ASVH1	380.7167	0.0429376	4.29376
	ADVH2	164.4592	ASVH2	396.1595	0.03305205	3.305205
	ADVH3	146.4456	ASVH3	392.5111	0.02970535	2.970535

Table 3-7 Calculations of the mechanical properties of sample 2 for temperature +25 °C

Strain level	+25 °C					
	Different Strain level	Dissipation Energy	Different Strain level	Stored Energy (kJ)	EVD	EVD %
Low Strain	ADL1	10.9107	ASL1	131.7717	0.00659236	0.659236
	ADL2	5.5946	ASL2	132.9517	0.00335031	0.335031
	ADL3	2.7777	ASL3	135.2782	0.00163481	0.163481
Med Strain	ADM1	39.5766	ASM1	194.021	0.01624053	1.624053
	ADM2	28.6399	ASM2	195.7293	0.01165	1.165
	ADM3	25.3266	ASM3	202.0971	0.00997762	0.997762
High Strain	ADH1	100.7882	ASH1	304.2882	0.02637151	2.637151
	ADH2	70.1169	ASH2	297.9121	0.01873894	1.873894
	ADH3	61.9072	ASH3	304.9465	0.01616322	1.616322
V High Strain	ADVH1	165.3825	ASVH1	395.0089	0.03333443	3.333443
	ADVH2	113.3897	ASVH2	393.7653	0.02292696	2.292696
	ADVH3	99.4585	ASVH3	400.6817	0.01976299	1.976299

Table 3-8 Calculations of the mechanical properties of sample 2 for temperature +5 °C

Strain level	+5 °C					
	Different Strain level	Dissipation Energy	Different Strain level	Stored Energy(kJ)	EVD	EVD%
Low Strain	ADL1	4.1091	ASL1	106.6656	0.00306713	0.306713
	ADL2	0.956	ASL2	109.168	0.00069722	0.069722
	ADL3	1.6303	ASL3	108.8272	0.00119273	0.119273
Med Strain	ADM1	41.8645	ASM1	196.544	0.01695885	1.695885
	ADM2	30.9698	ASM2	198.632	0.01241365	1.241365
	ADM3	28.6116	ASM3	206.0853	0.01105364	1.105364
High Strain	ADH1	97.4636	ASH1	283.4568	0.02737574	2.737574
	ADH2	73.5705	ASH2	288.7591	0.02028516	2.028516
	ADH3	66.9669	ASH3	294.164	0.01812513	1.812513
V High Strain	ADVH1	165.1143	ASVH1	383.5022	0.03427892	3.427892
	ADVH2	125.7236	ASVH2	396.6401	0.02523658	2.523658
	ADVH3	113.0759	ASVH3	403.3512	0.02232015	2.232015

Figure 3-28 shows the variation of energy dissipation per cycle, equivalent viscous damping, and equivalent stiffness with tempreture for the tests conducted at different loading frequences. It can be seen that the energy dissipation generally decreases with increasing tempreture. In particular, there is a 32%, 42%, and 50% decrease in the dissipated energy at the loading frequencies of 0.05, 0.5 and 1.0 Hz, respectively when the temperature changes from -35 °C to +25 °C. A similar decrease is also observed in the equivalent viscous damping ratio for increasing tempreture. The equivalent viscous damping ratio decreases from 4.96% at -35 °C to 3.34% at +25 °C at loading frequency of 0.05 Hz; from 4.04% at -35 °C to 2.29% at +25 °C at loading frequency of 0.5 Hz; and from 4.07% at -35 °C to 1.98% at +25 °C at loading frequency of 1 Hz. Despite the significant changes in damping properties observed for a temperature change from -35 °C to +25 °C, the change in both dissipated energy and equivalent viscous damping ratio remain within 10% when the tempreture changes from +5 °C to +25 °C. On the other hand, equivalent stiffness obtains higher values at higher tempretures for various loading frequinces. When tempreture increases from -35 °C to +25 °C, the equivalent stiffness increases by 29%, 34%, and 35% at loading frequencies of 0.05, 0.5, 1.0 Hz, respectively. This increase in the equivalent stiffness can be attributed to the fact that during loading the material reaches at higher stress levels for the same strain amplitude at higher temperatures. Figure 3-29 shows the variation of energy dissipation per cycle, equivalent viscous damping, and equivalent stiffness with tempreture for the tests conducted

at different loading frequences. It can be seen that the energy dissipation generally decreases with increasing tempreture. In particular, there is a 32%, 42%, and 50% decrease in the dissipated energy at the loading frequencies of 0.05, 0.5 and 1.0 Hz, respectively when the temperature changes from -35 °C to +25 °C. A similar decrease is also observed in the equivalent viscous damping ratio for increasing tempreture. The equivalent viscous damping ratio decreases from 4.96% at -35 °C to 3.34% at 25 °C at loading frequency of 0.05 Hz; from 4.04% at -35 °C to 2.29% at 25 °C at loading frequency of 0.5 Hz; and from 4.07% at -35 °C to 1.98% at +25 °C at loading frequency of 1.0 Hz. Despite the significant changes in damping properties observed for a temperature change from -35 °C to +25 °C, the change in both dissipated energy and equivalent viscous damping ratio remain within 10% when the tempreture changes from +5 °C to +25 °C. On the other hand, equivalent stiffness obtains higher values at higher tempretures for various loading frequinces. When tempreture increases from -35 °C to +25 °C, the equivalent stiffness increases by 29%, 34%, and 35% at loading frequencies of 0.05, 0.5, 1.0 Hz, respectively. This increase in the equivalent stiffness can be attributed to the fact that during loading the material reaches at higher stress levels for the same strain amplitude at higher temperatures.

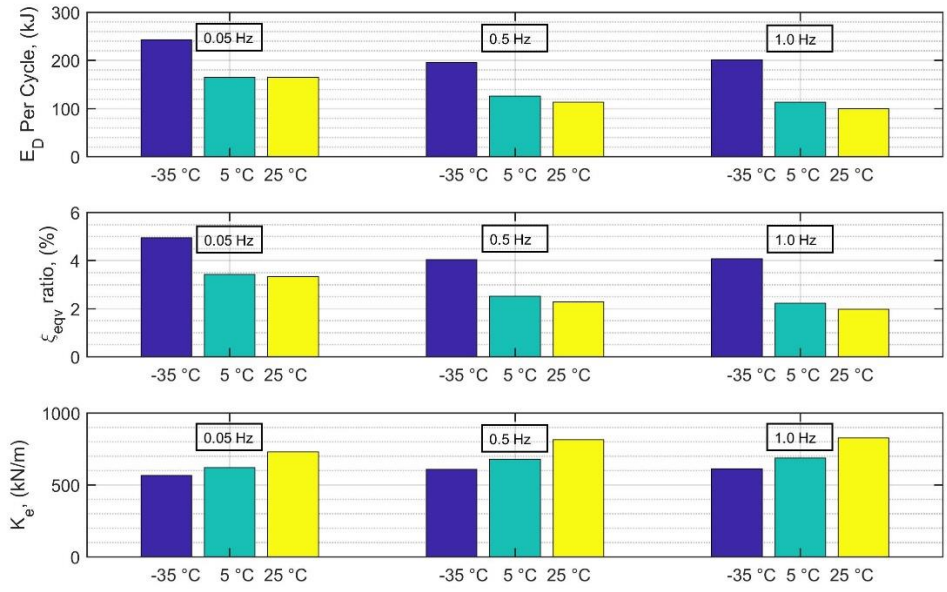

Figure 3-228 Variation of energy dissipation per cycle, equivalent viscous damping, and equivalent stiffness with temperature

Figure 3-29 shows the variation of energy dissipation per cycle, equivalent viscous damping, and equivalent stiffness with loading frequencies at different tempretures. It can be seen that the

reduction in energy dissipation, for various tempretures, ranges from 20% to 31% when the loading frequency increase from 0.05 Hz to 0.5 Hz. Nonetheless, the energy dissipation alters only -10% when loading frequences changes from 0.5 Hz to 1.0 Hz.

Similarly, it can be seen that the equivalent viscous damping ratio decreases by increasing loading frequency. In particular, there is a 26% and 11% reduction in the equivalent viscous damping ratio when the loading frequency changes from 0.05 Hz to 0.5 Hz and when the loading frequency alters from 0.5 Hz to 1.0 Hz, respectively. On the other hand, due to an increase observed in the slope of forward phase transformation plateu with an increase in the loading frequency, the equivalent stiffness attains slightly higher values at larger loading frequencies. When the loading frequency increases from 0.05 Hz to 1.0 Hz, the equivalent stiffness increases 8%, 10%, and 13% at test tempretures of 35 °C, 5 °C to 25 °C, respectively.

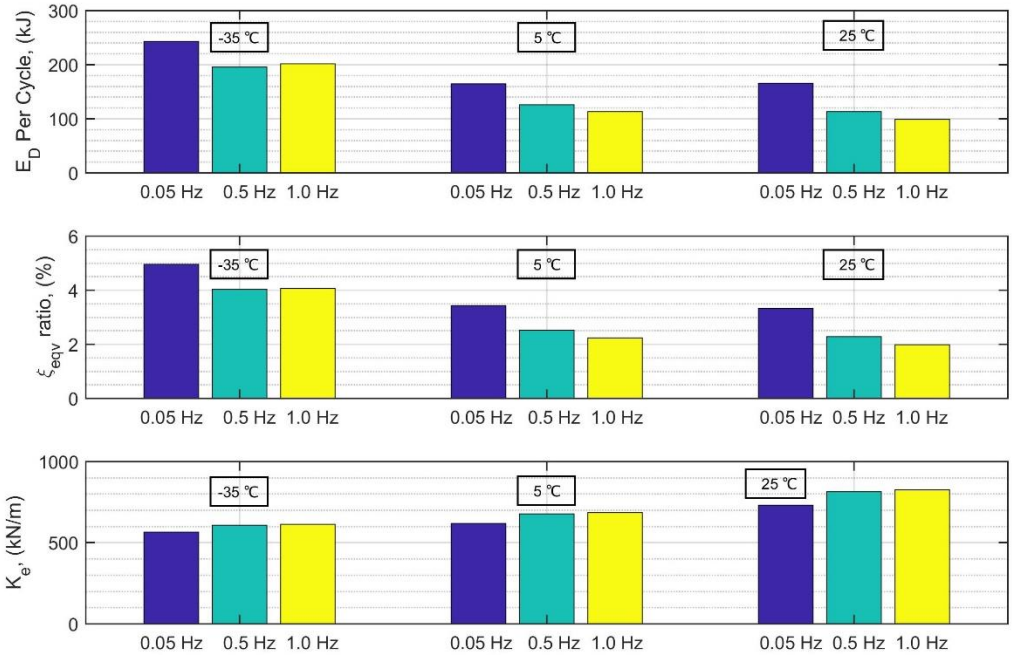

Figure 3-29 Variation of energy dissipation per cycle, equivalent viscous damping, and equivalent stiffness with loading frequency

3.6 Introduction to compressed friction spring

Friction springs consist of precisely manufactured outer and inner rings which touch each other on their tapered faces. This contact surface is called *element*. Figure 3-30 shows a friction spring that is composed of four outer rings, three inner rings and two inner ring halves, i.e. the friction spring comprises 8 elements. The number of elements is essential for the design of the spring because it determines the total travel and the total spring work. A friction spring works best when it ends with inner ring halves. For this reason, an even number of elements is preferably selected. When the spring column is axially loaded the tapered surfaces overlap causing the outer rings to expand and the inner rings get smaller in diameter. 2/3 of the introduced energy will be absorbed due to friction between the tapered surfaces of the mating rings.

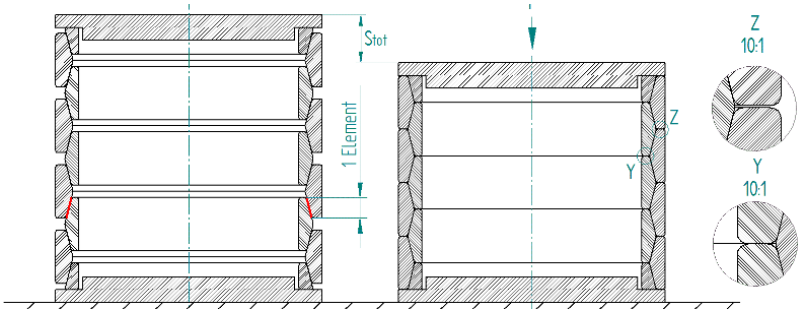

(a)

(b)

Figure 3-30 (a) Configuration of a friction spring with 8 elements, at rest (left) and loaded (right), (b) friction spring

Figure 3-31 shows basic technical characteristics of friction spring. The selection of the ring size defines further essential parameters for a friction spring; the end force F, The outer and inner guide diameters D_2 and d_2, the element height h_e, the spring travel per element s_e and the energy absorption per element W_e. For a given application, the required number of elements *e* is calculated from the desired spring travel or from the required spring work W, while the pre-load is neglected. Finally, the individual rings are built up to form complete spring columns.

3.6.1 Experimental test results of friction spring

Figure 3-31 shows experimental test results of the sample friction spring loaded up to 15 kN and then unloaded. According to the Figure 3-32 friction spring shows same behavior on every single test. As it can be seen from the results, friction spring has high energy dissipation capacity and capable of returning to its initial position which gives the sample very good re-centering behavior.

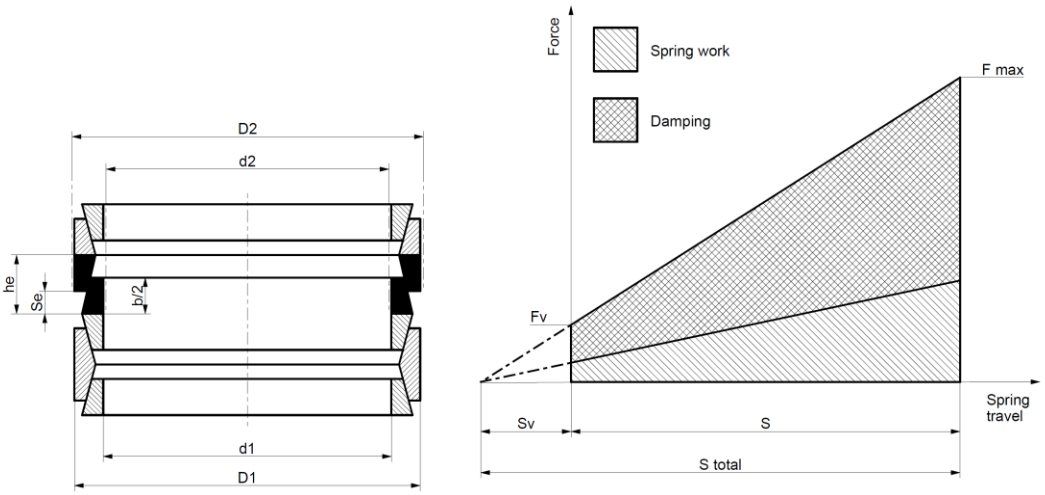

Figure 3-31 Basic technical characteristics of friction spring

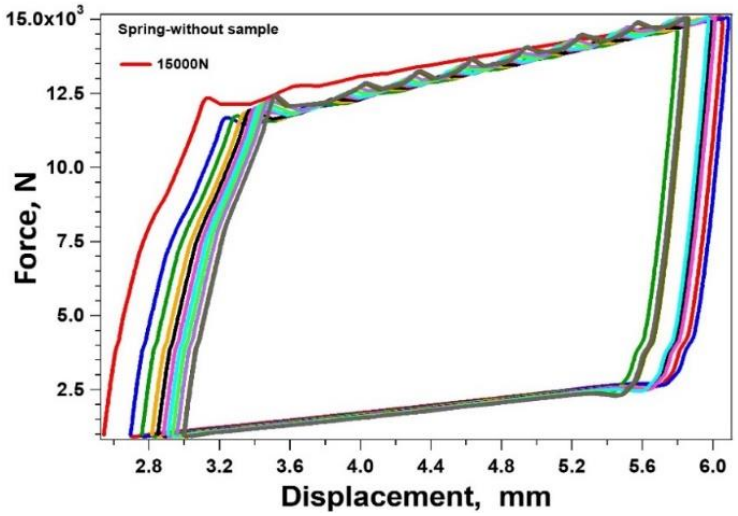

Figure 3-32 Compression behaviour of the friction spring under 15KN loading

3.7 SMA sample and friction spring assembly in series

In order to see the behavior of the friction spring in series with the SMA samples some additional experiments are conducted. After spring stabilize in 10 cycles (Figure 3-32), SMA sample attached

to the system on top grip in series with friction spring. Tests were conducted with the sample height of 6.3 mm and cross section of 4.47 x 4.70 mm^2 in room temperature. As it can be seen from Figure 3-33 sample was loaded up to 22 kN then unloaded.

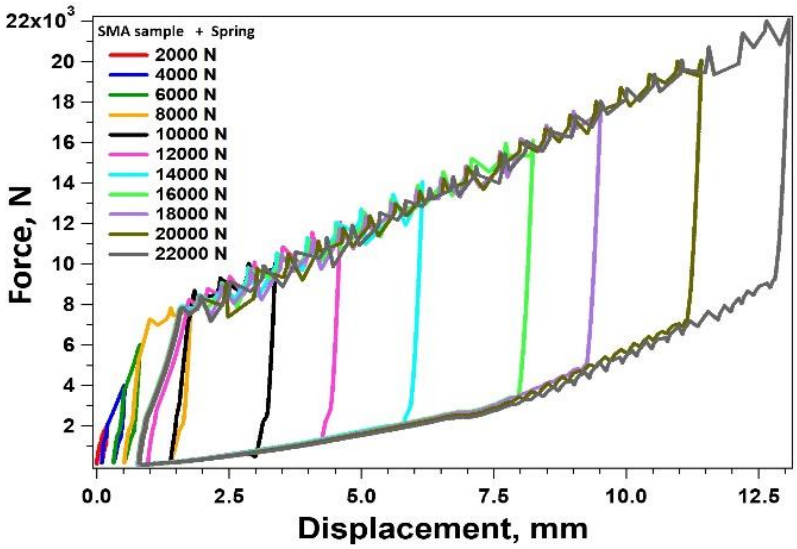

Figure 3-33 Compression behaviour of friction spring in series with SMA sample loaded up to 22 kN and unloaded in room temperature

Once this cycling completed, a new test with same sample was carried out. This time the height of the same is 4.47 mm with cross section of 6.30x4.47mm^2. This test was conducted with larger cross section. (Figure 3-34)

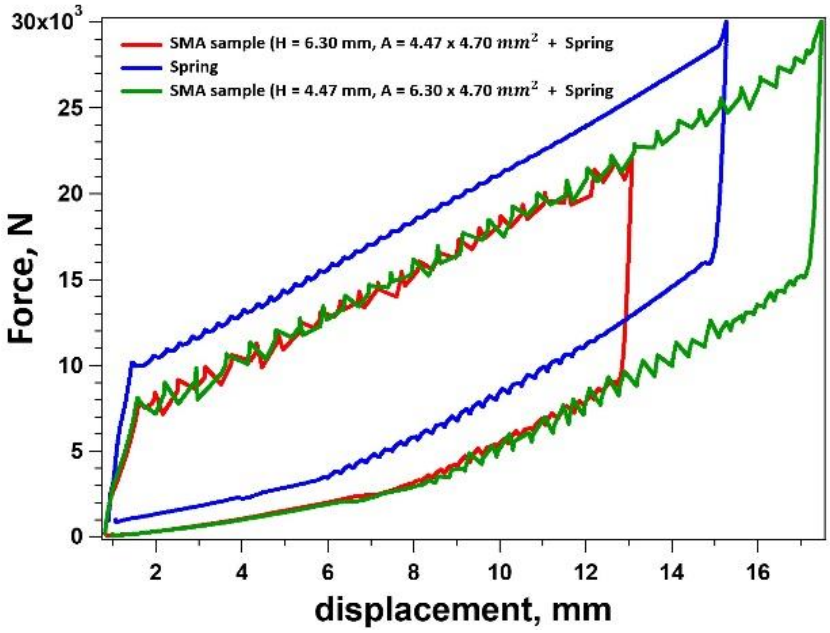

Figure 3-34 Comparison of the SMA sample and friction spring loaded up to 30 kN then uploaded

3.8 OpenSees simulations of SMA and friction spring samples

To model hysteretic response of SMAs samples at different temperatures and friction spring a mechanical model is proposed in Open System for Earthquake Engineering Simulation (OpenSees). Self-centering material is used for simulations of experimental data. (Figure 3-35)

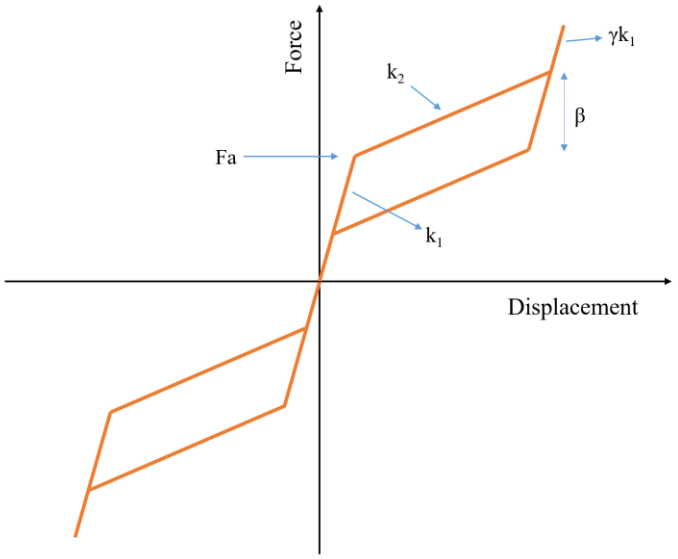

Figure 3-35 Self-centering material in OpenSees used for simulations

3.8.1 OpenSees simulation of SMA samples

The model can be consists of one, two or couple of self-centering material placed in parallel for the SMAs as shown in Figure 3-36 (a-b). It can also be combination of self-centering material with other defined materials in OpenSees. The use of two or more self-centering element instead of one for the SMAs provides more accurate modeling of the material response, especially for inner loops.

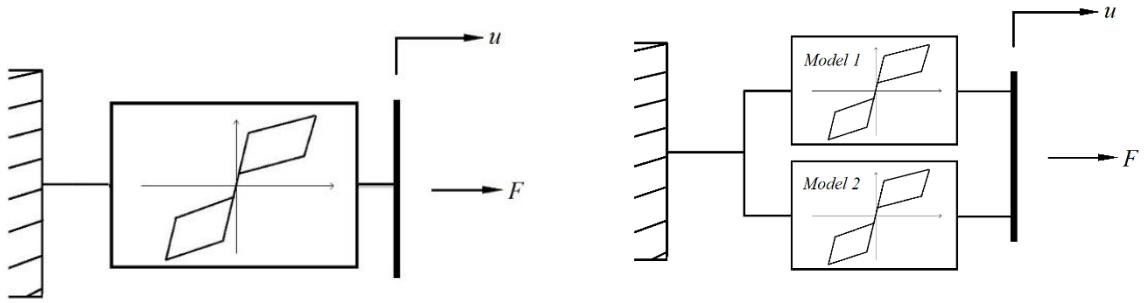

(a) (b)

Figure 3-36 A schematic representation of; (a) one self-centering material, (b) two self-centering material in parallel

An example of OpenSees experimental data simulation can be seen in the Figure 3-36. The experimental data of SMA samples can be found in Figure 3-37 (a). As it can be seen in Figure 3-37 (b), one of the stress-strain curves, green, is selected and again plotted in MATLAB programing. OpenSees simulation of the selected curve as well as experimental data is shown in Figure 3-37 (c). Two self-centering material are used for better fitting.

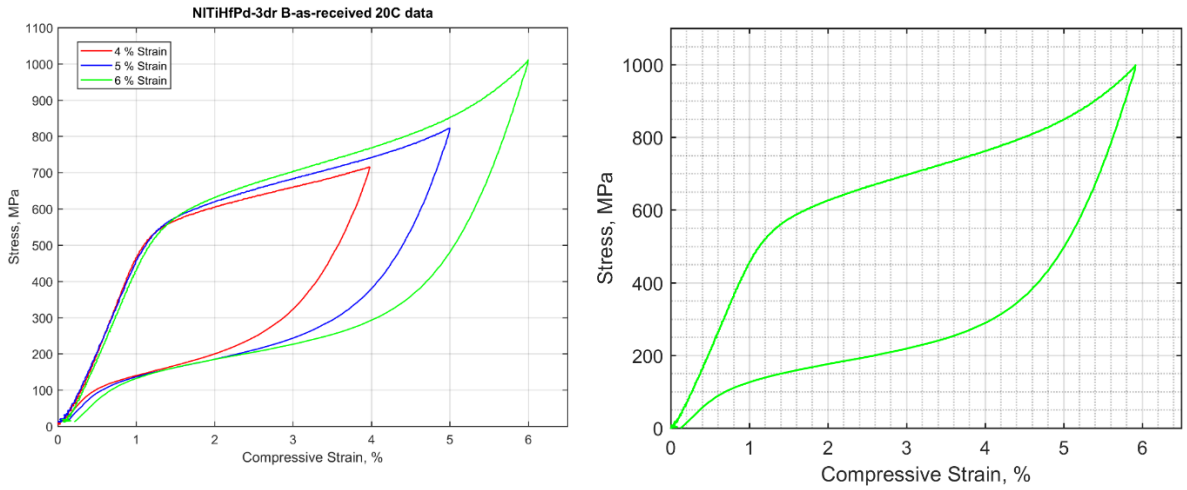

(a) (b)

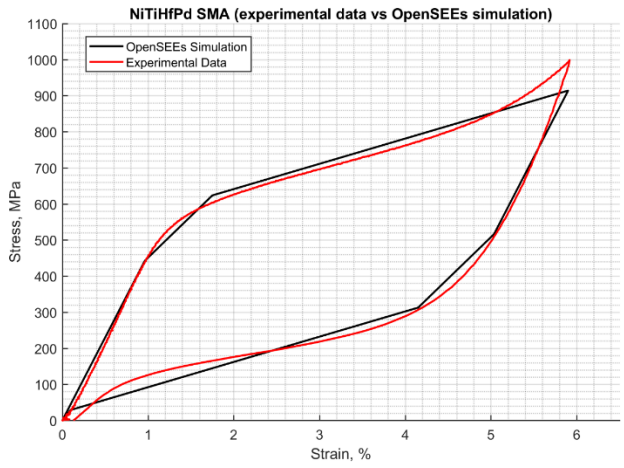

(c)

Figure 3-37 OpenSees simulation; (a) experimental data of SMA sample, (b) one selected experimental data, (c) simulation curve fitted well into experimental data

3.8.2 OpenSees simulation of friction spring sample

For the friction spring sample one of the cycles Figure 3-38 (b) (blue line) from experimental testing results (Figure 3-38(a)) of the spring is selected and modeled the behavior of the spring (Figure 3-38(c)). One self-centering material is good enough for a well-fitting.

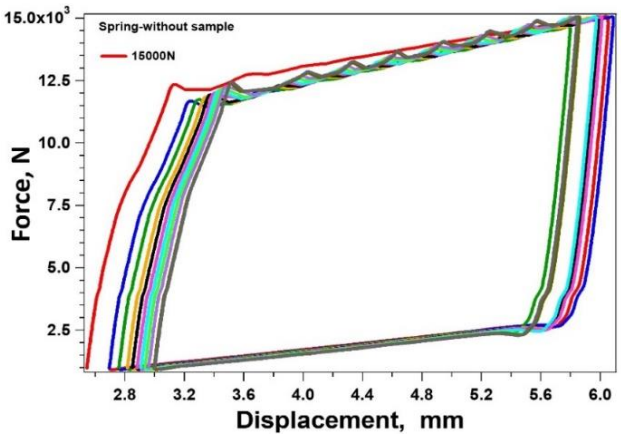

(a)

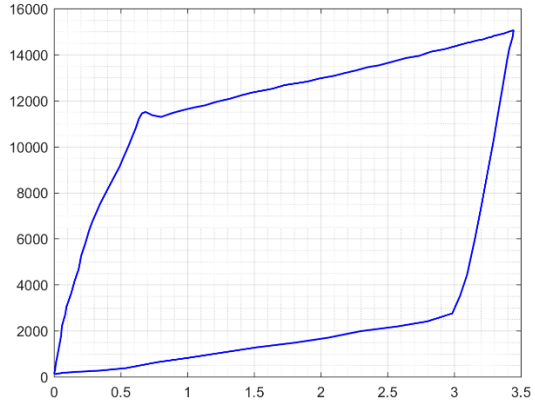

(b)

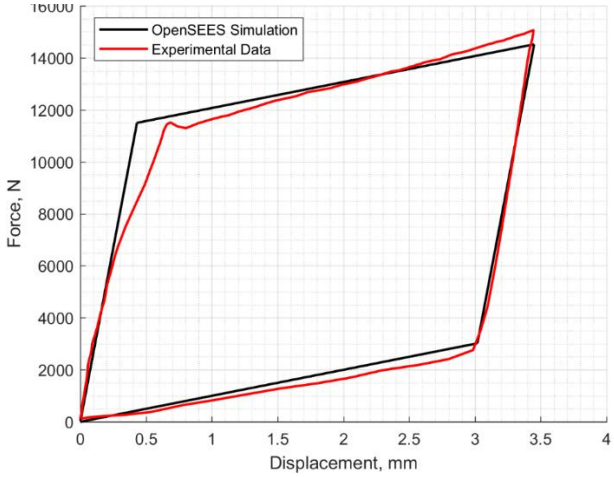

(c)

Figure 3-38 OpenSees simulation; (a) experimental data of friction spring sample, (b) one selected experimental data, (c) simulation curve fitted well into experimental data

According to the Figure 3-39, The behavior of the numerical model of the spring at large displacement levels is simulated with the experiemental behavior of the spring at large displacement levels (i.e. blue line in the second Figure below). Our numerical model seems to correctly modeling the spring behavior.

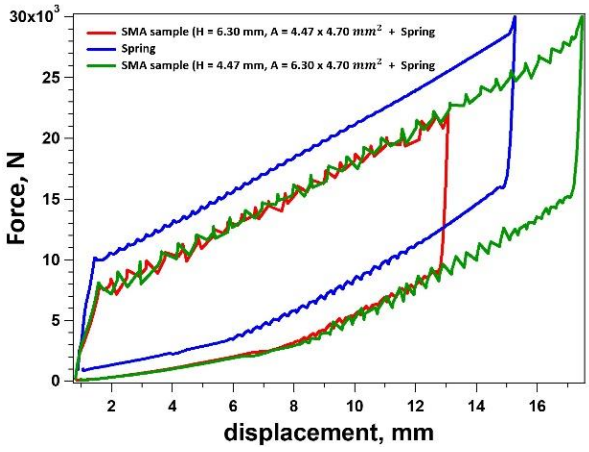

(a)

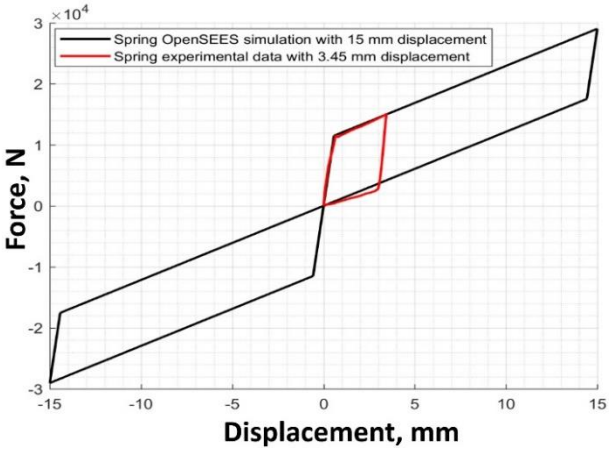

(b)

Figure 3-39 Comparison of the SMA sample and friction spring loaded up to 30 kN (c) OpenSees simulation of friction spring sample

3.9 OpenSees simulations of SMA and Friction Spring samples in series assembly

In order to investigate the behavior of the SMA sample in series with friction spring sample, some additional OpenSees simulations were run. It can be seen from Figure 3-40 that altering the properties of SMA samples will have enormous effect on the loop shape of the whole system which consequently could change mechanical behavior of the system. For instance, energy dissipation and equivalent viscous damping vary with using different properties for the SMA bars. This indicates that in order to design a proper dissipating system considering properties of materials is of more important tasks.

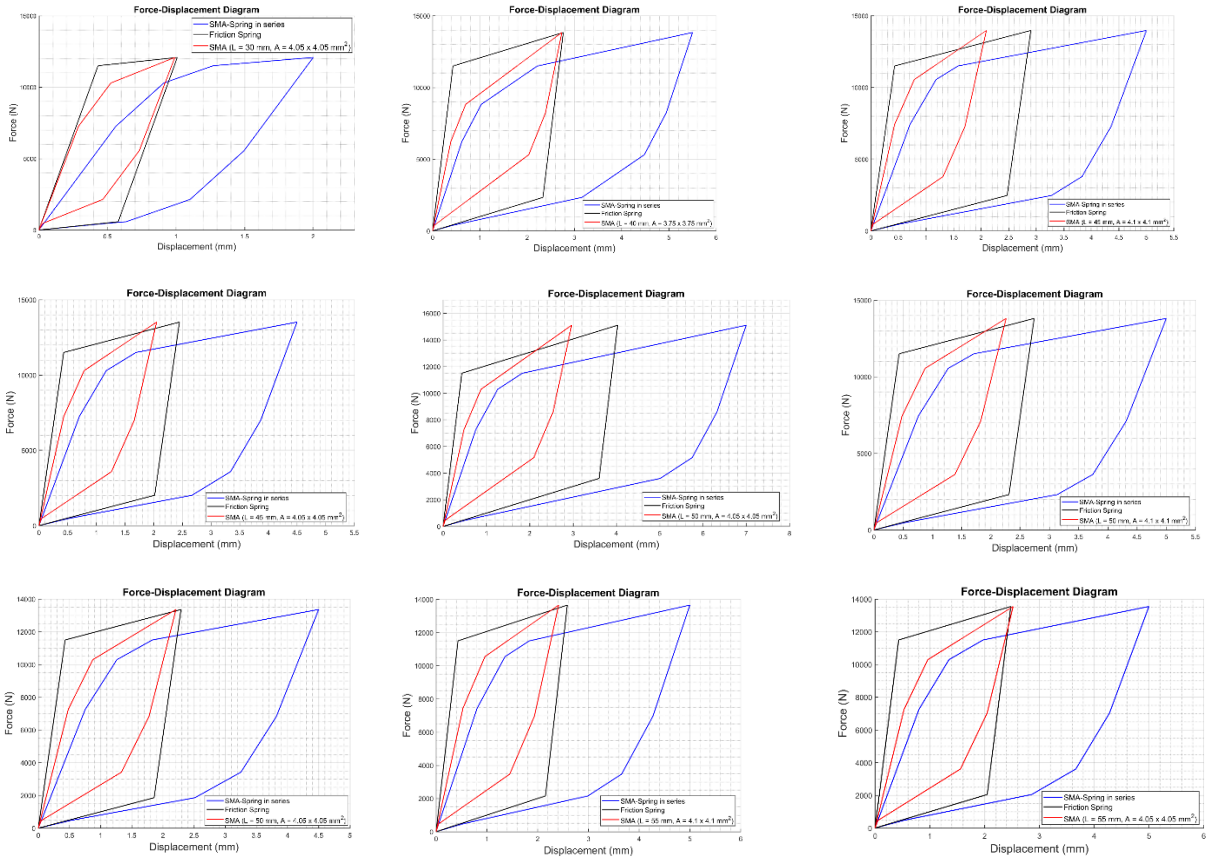

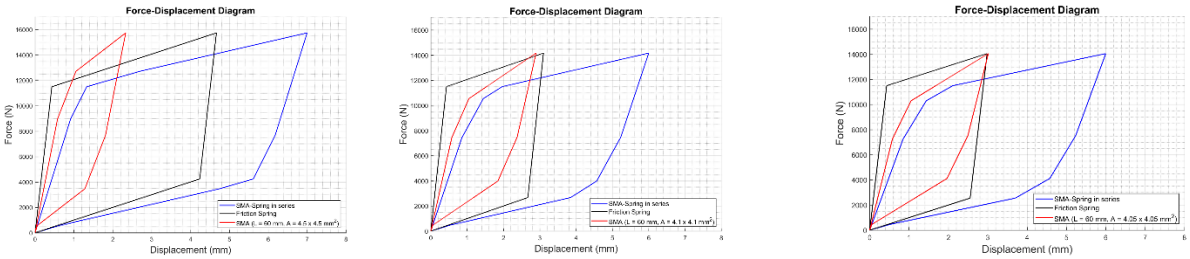

Figure 3-40 OpenSees simulations of SMA samples in series with Friction Spring sample applying various properties for the SMA bar specimens

3.10 Closure

In order to create a finite element OpenSees model of SMA bars and friction spring sample that is capable of simulating hysteretic behavior of SMAs at different conditions, a set of experimental data that is representative of SMA and spring behavior at these conditions is needed. Therefore, uniaxial tensile tests are performed on NiTiHfPd shape memory alloy bars and friction spring using an MTS servo-hydraulic load frame. Also, the effects of temperature, strain rate and strain amplitude on the mechanical response of superelastic SMAs were evaluated. The results show that the loading frequency and temperature considerably affect the behavior of superelastic SMAs. In particular, an increase in either temperature or loading frequency shifts the hysteresis loop upward. It is noted that the effect of the temperature is more pronounced than the influence of loading frequency. The area of the hysteresis loop, which represents the energy dissipation of superelastic SMAs, narrows with increasing temperature or loading frequency. As a consequence, as the temperature increases there is a decrease in the equivalent viscous damping for slowest (0.05 Hz) and highest (1.0 Hz) loading rates, respectively. Similarly, the equivalent viscous damping decreases for different test temperatures as the frequency increases from 0.05H to 1.0H. The results indicate that the effects of temperature and strain rate on the superelastic behavior of NiTiHfPd bars are significant.

What's more, experimental tests are conducted for friction spring. The results of the tests show that friction spring is a promising choice for using in passive structural dissipation systems. It can be seen that friction spring has very high force capacity as well as large deformation capacity which are very essential in structural applications.

At the end of the chapter OpenSees simulations are run for each of the SMA and spring samples as well as assembly of SMA bar samples and friction spring samples. We can confer from the simulation results that, first, OpenSees can properly simulate friction spring strain stress curve as well. Second, selecting good properties for the SMA and friction spring samples can tremendously effect mechanical behavior of the whole system.

4 Performance assessment of steel frame building with NiTiHfPd SMA Braces

4.1 Introduction

In addition to the immediate structural response to a dynamic event, the amount of residual deformation, once motion has stopped, is an important metric to evaluate building post-event performance. There are several different mechanisms for creating a restoring force to return a building structure to plumb after an earthquake. One approach is to allow structure to undergo controlled rocking at discrete locations such as column-base joint or beam-column joints. Another approach is to employ braces or seismic control devices with self-centering capabilities. Due to its inherent nonlinear elastic behavior, shape memory alloys (SMAs) have been considered to develop self-centering braces or devices. Recently, NiTiHfPd alloys that have very high strength (up to 2000 MPa), high dissipation/damping capacity, good cyclic stability and large operating temperature have been developed. A numerical model that reliably simulates the response of NiTiHfPd SMAs is developed. Then, a four-story moment resisting frame with and without supplementary SMA damping elements is designed and modeled. Nonlinear response history analyses are conducted to assess the performance of NiTiHfPd SMAs in mitigating seismic response and limiting residual drifts of steel frames subjected to strong ground motions. This chapter explores the seismic performance of steel frame buildings designed with a NiTiHfPd SMA-based bracing system. In particular, the response of SMA-braced frame at different seismic intensity levels are evaluated and compared with a traditionally designed steel moment resisting frame (SMRF). The effect of temperature on the seismic performance of the SMA-braced frame is also analyzed.

4.2 Modeling of NiTiHfPd SMAs

To model hysteretic response of NiTiHfPd SMAs at different temperatures, a mechanical model is proposed in Open System for Earthquake Engineering Simulation (OpenSees) [115]. The model consists of two self-centering materials placed in parallel as shown in Figure 4-1 is proposed. The use of two self-centering element instead of one provides more accurate modeling of the material response, especially for inner loops. Since the SMAs will be subjected to dynamic loading during an earthquake, the experimental responses of SMAs at 1 Hz are used for the numerical modeling.

The selected parameters of the proposed model under the three different temperature of 25℃, 5℃ and -35℃ are given in Table 4-1. Figure 4-2 shows the hysteretic curves predicted by the proposed model and experimental response at each temperature. It can be seen that the proposed model can predict the response of NiTiHfPd SMA material very well.

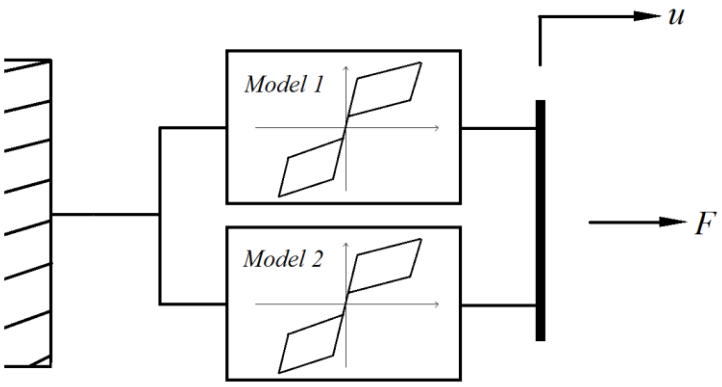

Figure 4-1 Proposed SMA model

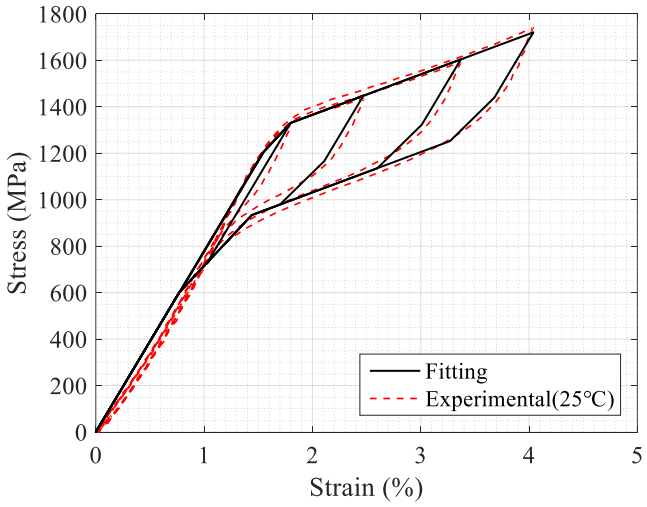

(a)

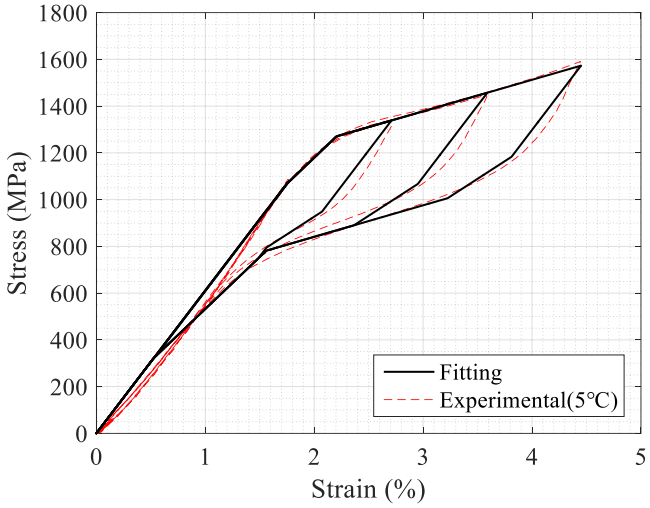

(b)

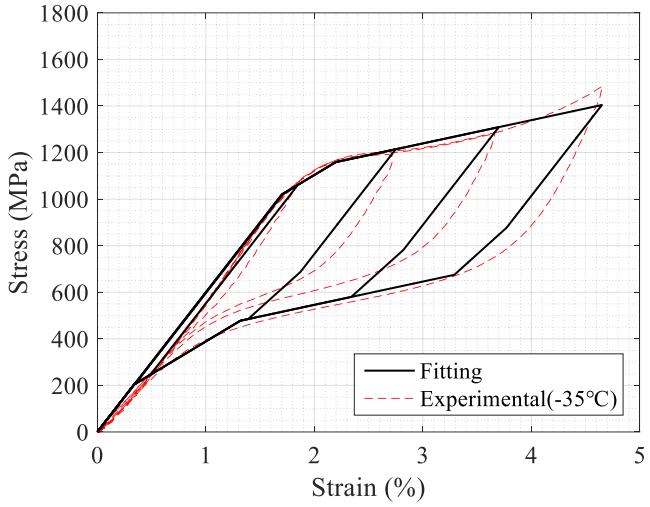

(c)

Figure 4-2 Experimental stress-strain curves and model predictions at temperature of (a) +25℃, (a) +5℃ and (c) -35℃

Table 4-1 Parameters of proposed SMA model

Temperature	25℃		5℃		-35℃	
Model	1	2	1	2	1	2
Initial stiffness (MPa/%)	370	410	234.4	377	370	230
Post-transformation stiffness (MPa/%)	87	87	67.4	67.4	50	50
Forward transformation stress (MPa)	570	738	410.2	829.4	629	505
Ratio of forward to reverse activation stress (β)	0.50	0.20	0.70	0.29	0.80	0.40

4.3 Building Models

4.3.1 Case-Study Building

The prototype steel frame building selected for numerical simulations is designed as an office building located on soil type D in Los Angeles. The structural system consists of steel special moment resisting frame (MRF) designed with fully restrained reduced beam sections and connected with partial restrained gravity frame, which is designed in accordance with LRFD specifications, IBC (2003), SEI/ASCE-02 and ASIC (2002) design provisions. The plan and elevation of the East-West direction of the building are shown in Figure 4-4. The structure is classified as Category II and the Maximum Considered Earthquake spectral response acceleration is 1.5g at short periods (S_S) and 0.9g at 1 second period (S_1). The design spectral acceleration parameters S_{MS} and S_{M1} are 1.0g and 0.6g. More details of the prototype frame can be found in [116].

Two special MRF bays and two additional gravity frame bays on the perimeter as shown in Figure 4-4 (b) is modeled using the OpenSees platform [115]. The lateral stiffness and strength of gravity system are generally not included when assessing the seismic performance of steel special moment resisting frame [117]. However, the gravity framing system can profoundly affect the computed response [118]. Therefore, two exterior gravity frame bays are incorporated as a part of the lateral

load resisting frame in this study. The steel moment resisting frame is modeled as two-dimensional centerline model with elastic beam-column elements connected by plastic hinge rotational springs. The inelastic hysteretic behavior of rotational spring is based on the modified Ibarra-Medina Krawinkler (IMK) model, which has the ability to capture the structural cyclic strength and stiffness deterioration associated with structural damage Figure 4-3.

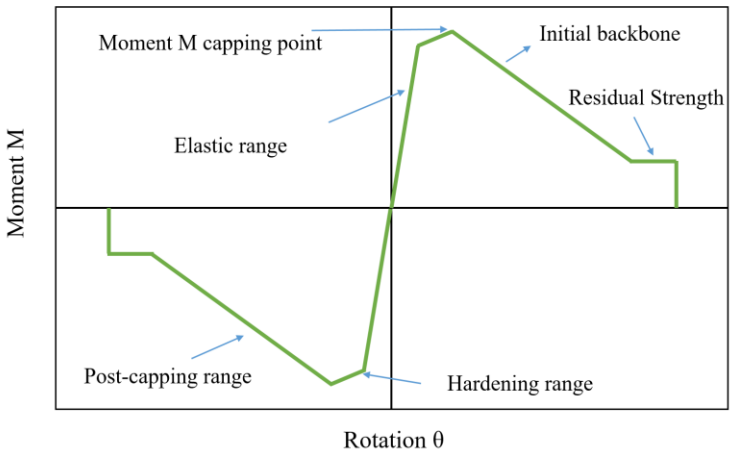

(a)

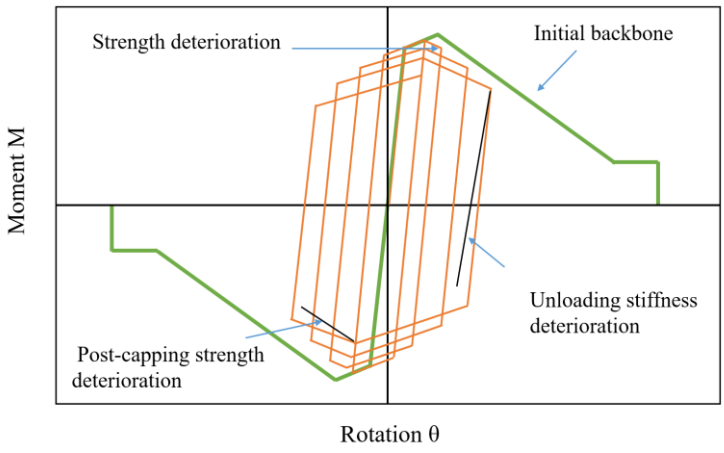

(b)

Figure 4-3 Modified Ibarra-Krawinkler Hysteretic Model: (a) monotonic (b) cyclic

The model parameters of backbone curves in IMK model for steel components can be obtained from empirical equations based on calibration of experimental data [116]. The panel zone is explicitly modeled using the approach of Gupta and Krawinkler [119] as a rectangle composed of eight stiff elastic beam-column elements with one zero-length element which serves as rotational

spring to represent its nonlinear shear behavior. A tri-linear backbone curve without stiffness and strength deterioration is assigned to the rotational spring to account for the deformation of panel zone. The columns of the gravity frame are considered to be oriented in weak axis and pinned to the base. The connections in the gravity frame are taken into account in the analysis by modeling them as partially restrained (PR) connection. The flexural strength of gravity connections is considered to be 25% of plastic moment strength of the beam and the hysteretic behavior curve are based on the parameters given in Table 9-6 of ASCE 41-13 [120]. The leaning columns carry the gravity loads applied to interior gravity frame and are linked to the main frame to account for the P-delta effects. However, the leaning column is modeled as elastic beam-column elements connected to main frame by very small stiffness hinges and does not provide additional lateral stiffness and strength from gravity frame.

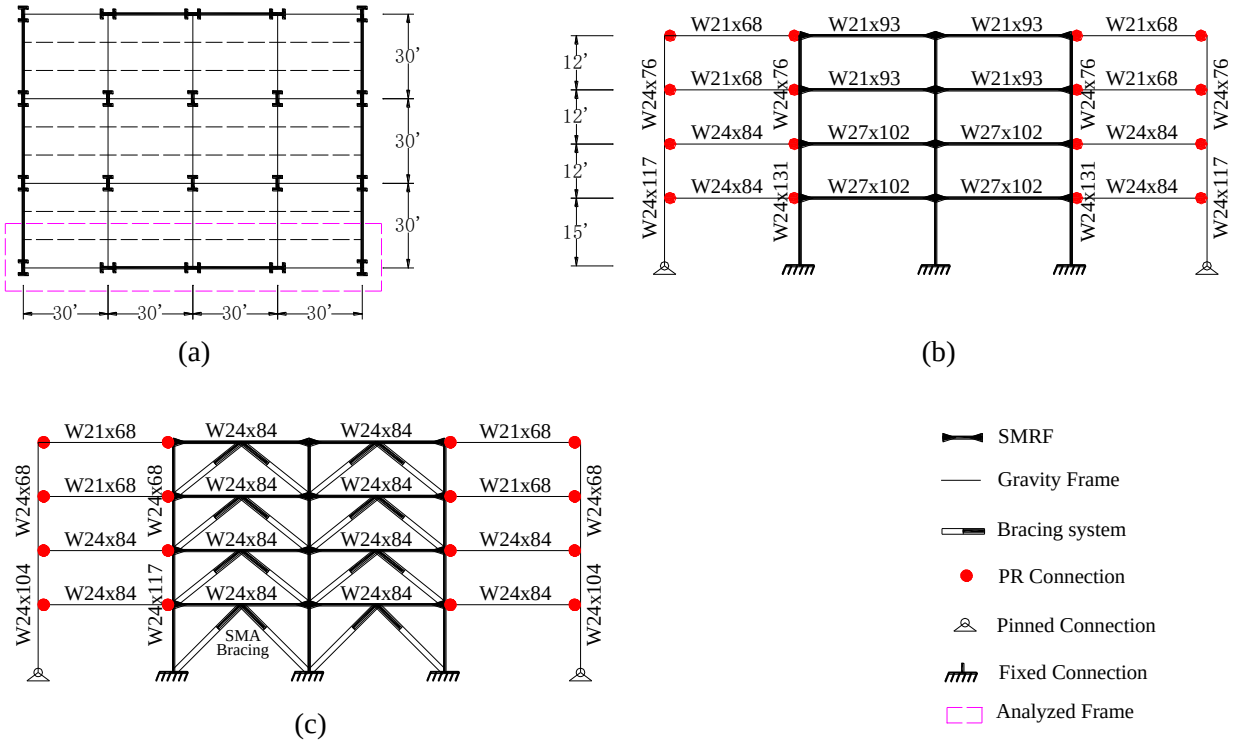

Figure 4-4 Structural model illustration: (a) Plan view, (b) SMRF Frame and (c) SMA Braced Frame

4.3.2 SMA-braced Frame

In this section, the design of steel frames with SMA bracing systems is discussed. First, an SMA-braced frame is designed assuming the room temperature (25°C) properties of SMAs such that it

has comparable strength and stiffness with the original SMRF. To achieve this, the strength of the SMRF is reduced by selecting smaller beam and column section sizes for the frame system such that the reduced strength frame has a base shear capacity equal to about 75% of the base shear capacity of the original SMRF and the selected frame sections satisfy the strength requirements of ASCE 7-10 and ANSI/AISC 360-10 [121-122]. Then, the chevron bracing configuration for SMA braces is adopted and SMA braces are installed at each bay at each story of moment resisting frame as shown in Figure 4-4 (c) to satisfy the drift requirements, which is confirmed from through nonlinear response history analyses method.

To investigate the effect of the ambient temperature on seismic performance of SMA braced frames, two additional sets of the brace properties under the temperature of 5℃ and -35℃ have been derived. Note that the geometric dimensions of SMA braces remain the same at each temperature but the structural properties such as initial stiffness and yield force of the bracing system varies for different temperatures as shown in Table 4-2 since the mechanical response of the SMAs changes with temperature as discussed earlier. A total of three sets of SMA brace parameters under the temperature of 25℃, 5℃ and -35℃ are considered. Note that the geometric properties of the SMA braces installed at the 1st and 2nd floors are the same but they are different than those at the 3rd and 4th floors.

Table 4-2 SMA brace properties

Temperature	SMA brace	Story	SMA Length (mm)	SMA Area (mm^2)	Initial Stiffness (kN/mm)	Post-yield Stiffness (kN/mm)	Yield Displacement (mm)	Yield Force (kN)	β
25°C	Brace-I	1-2	3300	150	3.55	0.8	50.82	180	0.33
	Brace-II	3-4	2900	150	4.04	0.9	44.66	180	0.33
5°C	Brace-I	1-2	3300	150	2.78	0.61	57.75	160	0.41
	Brace-II	3-4	2900	150	3.16	0.7	50.75	160	0.41
-35°C	Brace-I	1-2	3300	150	2.73	0.45	56.10	153	0.64
	Brace-II	3-4	2900	150	3.10	0.52	49.30	153	0.64

4.4 Ground Motions

Three sets of SAC ground motions for Los Angeles are used in the numerical simulations. The selected ground motion records are representative of three different hazard levels with a probability of exceedance of 50%, 10% and 2% in 50 years, corresponding to return periods of 72, 475, and 2475 years, respectively. Each set of the ground motions consist of 10 pairs of orthogonal records (i.e. 20 ground motion records). More details concerning individual component information and scaling of the records can be found in FEMA-355C [123].

4.4.1 Comparative Seismic Performance Assessment for SMA-braced Frame

Nonlinear response history analyses are carried out for SMRF and SMA-braced Frame (assuming design temperature of 25℃) under a total of 20 ground motions scaled to three different seismic intensity levels. Figure 4-5 compares the maximum inter-story drift ratio (IDR), maximum floor absolute acceleration (FAA) and maximum residual inter-story drift ratio (RIDR) for SMRF and SMA-braced Frame at different seismic intensity levels. In addition, Table 4-3 shows the median values of IDR, FAA and RIDR under 20 ground motions at each intensity level. The results reveal that the SMA-braced frame shows similar seismic performance in terms of IDR and FAA under three different levels intensities. However, the SMA-braced Frame effectively reduces the residual drifts at the seismic intensity levels of 10/50 and 2/50. In particular, the SMRF exhibit a median RIDR above 4% under ground motion records with a probability of exceedance of 2% in 50 years, while the median RIDR is only 0.69% for the SMA-braced frame.

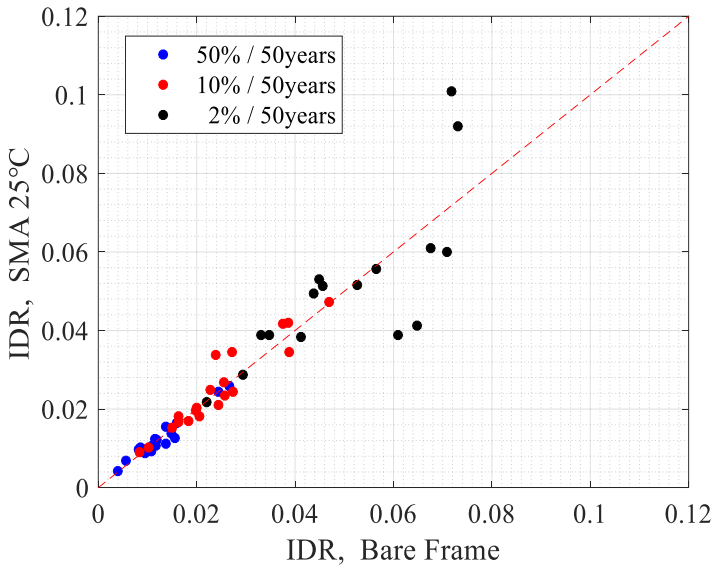

(a)

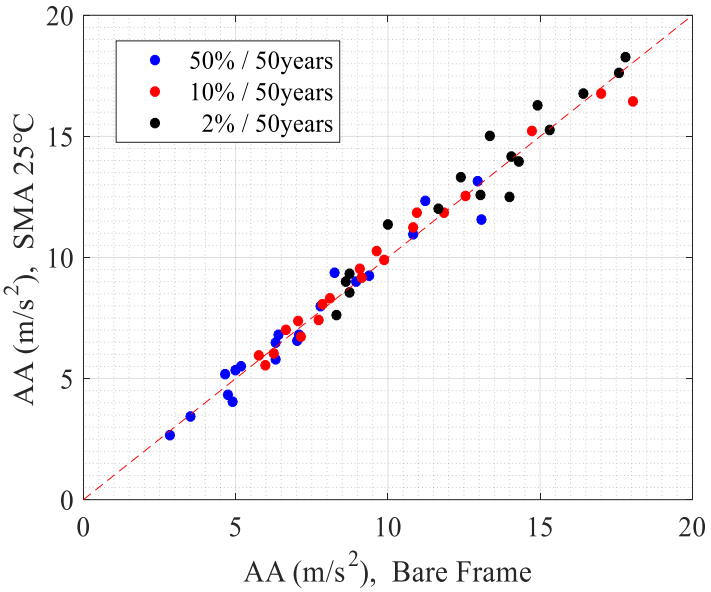

(b)

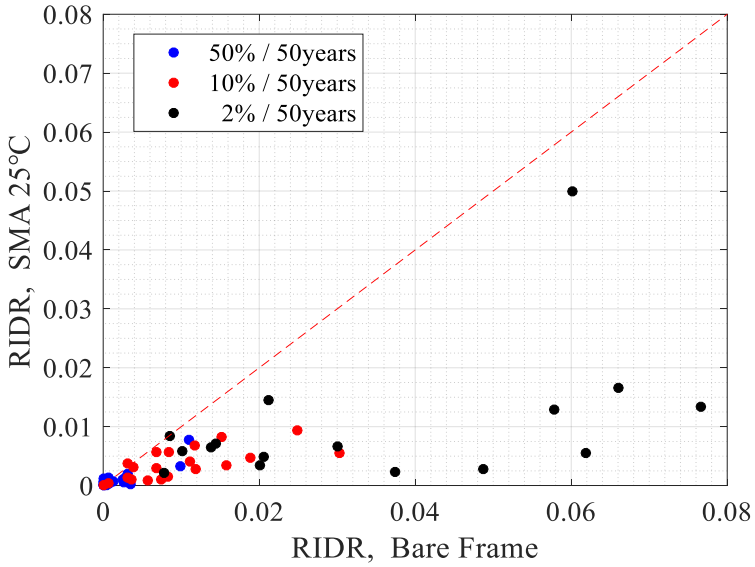

(c)

Figure 4-5 Values of the maximum (a) IDR, (b) AA and (c) RIDR obtained from SMRF Frame versus SMA Frame under +25 ℃

Table 4-3 Median value of structural demand parameters

GM	Median IDR (%)		Median AA (m/s^2)		Median RIDR (%)	
Intensity	SMRF	SMA-braced Frame	SMRF	SMA-braced Frame	SMRF	SMA-braced Frame
50% /50	1.13	1.07	6.72	6.68	0.09	0.06
10% /50	2.34	2.23	9.12	9.35	0.79	0.33
2% /50	5.88	5.23	14.03	13.14	4.31	0.69

4.5 Effect of Temperature on Seismic Performance of SMA-braced Frame

4.5.1 Static pushover analysis (POA)

To investigate the effect of temperature on the response of SMA-braced frame buildings, static pushover analyses at three different temperatures are conducted first. The pushover load pattern forces are distributed in proportion to the lateral force prescribed in ASCE 7-10 [121]. Table 4-4 presents the related dynamic and mechanical properties of the SMA-braced frame buildings at different ambient temperature. In table, T_1 is the fundamental period of vibration, θ_y is the roof drift at frame yielding, C_{max} is maximum frame strength coefficient (peak base shear force normalized by weight), α is post-yield stiffness ratio and μ_T is period-based ductility. The pushover curves of the frame at different temperatures are shown in Figure 4-6. It can be seen that the strength and initial stiffness of SMA-braced frames decrease with a decrease in ambient temperature. However, the variation in these properties is more prominent when the temperature reduces from +25 ℃ to +5 ℃ compared to those observed for a temperature change from +5 ℃ to -35 ℃.

Table 4-4 Dynamic and mechanical properties of the building models

Frame	T_1	θ_y	C_{max}	α	μ_T
SMA_25℃	1.265	0.078	0.259	0.237	4.51
SMA_5℃	1.289	0.083	0.251	0.198	4.11
SMA_-35℃	1.290	0.083	0.247	0.198	4.07

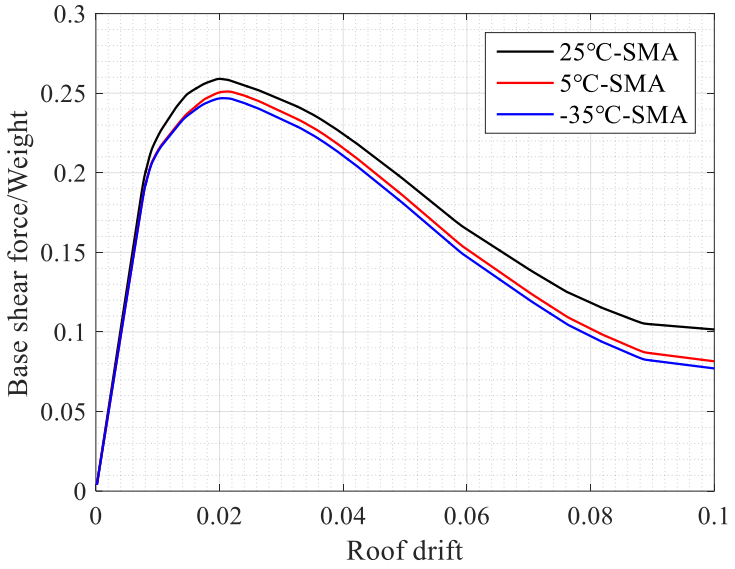

Figure 4-6 Pushover curves of the building models

4.5.2 Nonlinear Dynamic Analysis (NDA)

Additional nonlinear dynamic analysis are carried out on the SMA-braced frame assuming an outdoor (and bracing) temperature of 5℃ and -35℃ under each of 20 ground motions scaled to three different intensity levels. The median values of IDR, FAA and RIDR at different temperatures under seismic intensity levels of 50/50, 10/50 and 2/50 are summarized in Table 4-5. Figure 4-7 (a)-(c) plots the structural demand parameters distribution under 20 ground motions at different temperatures and seismic intensity levels. The results illustrate that the temperature have a very small influence on the median structural demand parameters. The largest variation in the response with temperature is observed for the RIDR at intensity level of 2/50, resulting in an increase from 0.69% at 25 ℃to 0.95% at -35℃.

Table 4-5 Median value of structural demand parameters

GMs Intensity	Median IDR (%)			Median FAA (m/s^2)			Median RIDR (%)		
	25℃	5℃	-35℃	25℃	5℃	-35℃	25℃	5℃	-35℃
50% /50	1.068	1.073	1.225	6.678	6.574	6.573	0.064	0.065	0.061
10% /50	2.229	2.312	2.329	9.35	9.15	9.144	0.328	0.369	0.391
2% /50	5.227	5.251	5.118	13.14	13.33	13.15	0.689	0.829	0.950

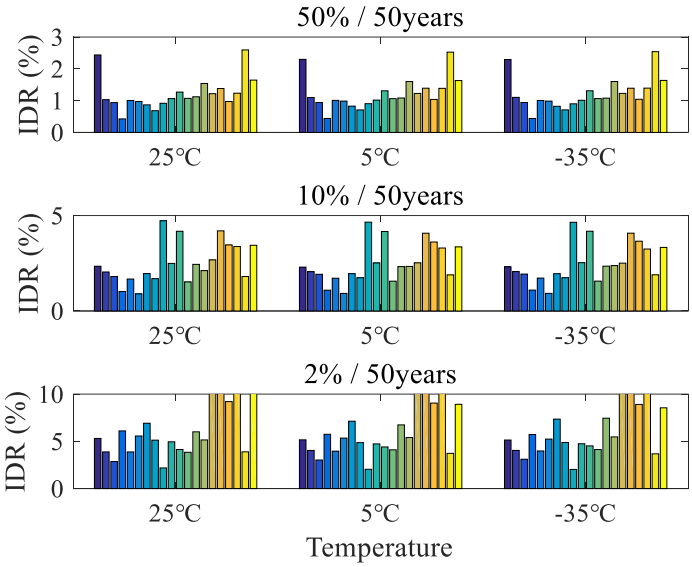
50% / 50years
IDR (%)
3
2
1
0
25°C
5°C
-35°C
10% / 50years
IDR (%)
5
0
25°C
5°C
-35°C
2% / 50years
IDR (%)
10
5
0
25°C
5°C
-35°C
Temperature

(a)

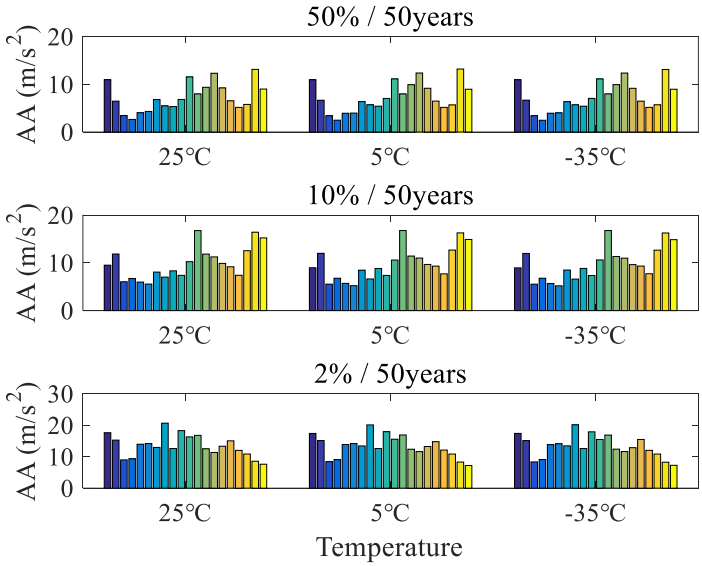
50% / 50years
AA (m/s2)
20
10
0
25°C
5°C
-35°C
10% / 50years
AA (m/s2)
20
10
0
25°C
5°C
-35°C
2% / 50years
AA (m/s2)
30
20
10
0
25°C
5°C
-35°C
Temperature

(b)

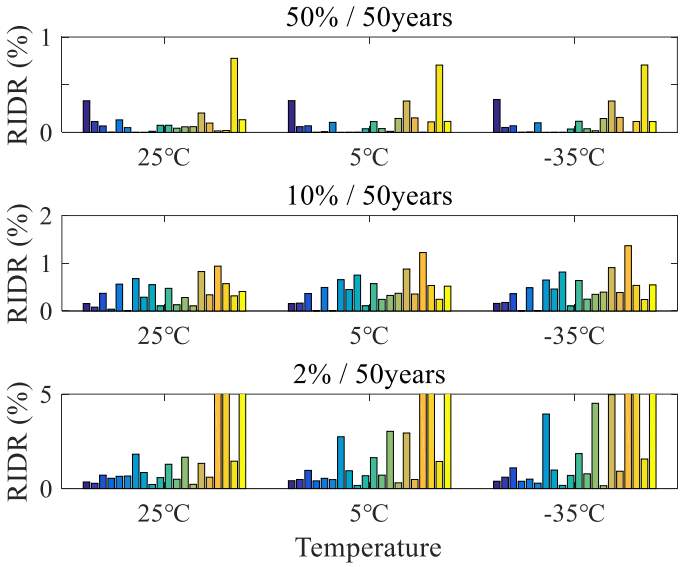

(c)

Figure 4-7 Distribution of (a) IDR, (b) AA and (c) RIDR under 20 ground motions at different temperatures and seismic intensity levels

4.6 Closure

In this chapter, NiTiHfPd alloy system are employed as a bracing system in a steel frame building to provide re-centering and energy-dissipating capabilities. First, experimental tests on NiTiHfPd alloys that have ultra-high strength, large damping capacity, and wide operating temperature range are discussed. Then, a case-study steel building is selected and modeled for numerical investigations. The selected steel moment resisting frame building is also designed and modeled with SMA bracing system such that the SMA-braced frame has comparable strength and stiffness with the original SMRF. Nonlinear response history analyses on conventional SMRF and SMA-braced frame are conducted at different seismic intensity levels using a set of 20 ground motion records. The results indicate that the residual story drifts can significantly be reduced when the steel building are designed with SMA-bracing systems. It is also explored that changing temperature between -35℃ and 25℃ does not affect the performance of NiTiHfPd SMA bracing systems.

5 Superelastic Memory Alloy Re-centering Damper (SMARD)

5.1 Introduction

This chapter presents the description of a new passive structural control device named as a superelastic memory alloy re-centering damper. The proposed superelastic memory alloy re-centering damper (SMARD) relies on shape memory alloy bars for re-centering capability and employs a friction spring that has both high energy dissipating and large deformation capacity. For SMA bars new kind of shape memory alloy material named as NiTiHfPd is utilized. The experimental studies on the individual components of the new damper, namely SMA bars and friction spring, were described in chapter 3. Then, the design and the behavior of the proposed superelastic memory alloy re-centering damper are introduced.

5.2 Description of superelastic memory alloy re-centering damper (SMARD)

By exploiting the advantageous characteristics of NiTiHfPd SMAs, a new passive vibration device is proposed in this study. The device is named as Shape Memory Alloy-based Re-centering Damper or SMARD. Figure 5-1 shows plan and longitudinal view of the SMARD at its original and displaced positions to describe its operating principle. A three-dimensional rendering of the device is also shown in the Figure 5-2. The SMARD comprises a SMA-Spring assembly (rendered in yellow), a piston (gray), and an enclosure (black) with rigidly attached baffle plates. The high force steel springs between SMA groups ensure large displacements under load while simultaneously transmitting the force between SMA groups. Voids in the centers of the baffle plates allow the piston to pass through freely while arresting the otherwise free-traveling SMA-Spring assembly. Note that NiTiHfPd SMAs exhibit better super-elastic response under compression. Therefore, the device is designed such that whether the piston is drawn out of or forced into the device, the SMA-Spring assembly will undergo compression. Due to the inherent super-elastic behavior of NiTiHfPd SMAs and friction spring, the SMARD can exhibit excellent re-centering ability with enhanced energy dissipation capacity.

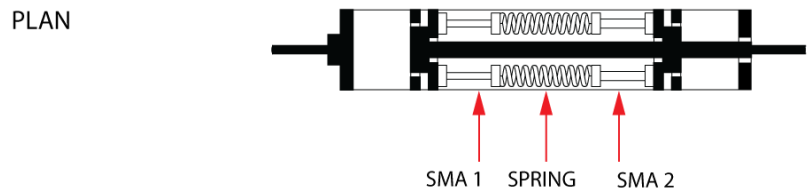

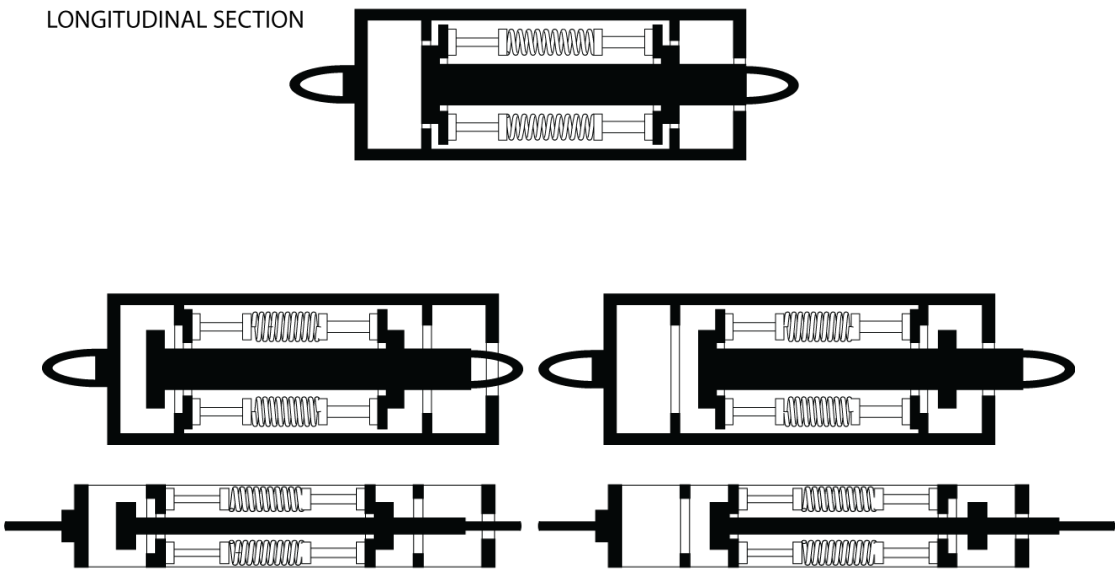

Figure 5-1 Plan view of SMARD at its original and displaced positions

In addition, SMA bars with up to four different diameters can be incorporated to the device. That will enable device to produce a damping force that ensures sufficient energy dissipation for various levels of excitation. The SMARD is illustrated with two different diameter bars (SMA1 and SMA2) in Figure 5-1. As a result of arrangement of SMA bars in the device and inherent re-centering behavior of SMAs, a properly designed SMARD will exhibit a re-centering and energy dissipating behavior during all modes of vibrations under both wind and earthquake excitations. During a weak to moderate event, the SMA bars with lower stiffness will experience relatively larger compressive strains and dissipate the energy while the stiffer SMA bars will undergo small strains. During a moderate to strong event, both SMA groups will engage and dissipate large amounts of energy, and the device will provide a larger damping force. During an extreme event, the SMARD will stiffen due to second stiffening of SMA bars under large strains. This additional stiffening will avoid potentially catastrophic structural displacements even under unforeseen strong ground motions.

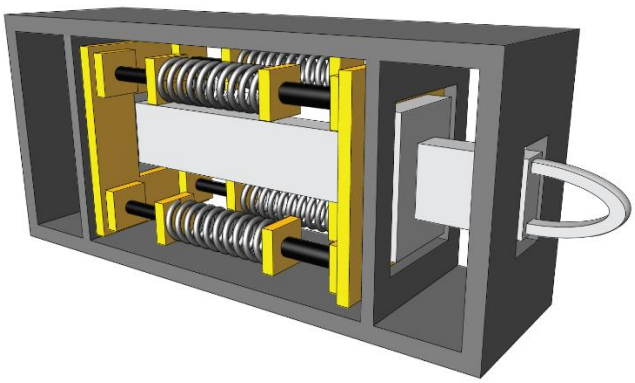

Figure 5-2 Three-dimensional rendering of SMARD

Compared with conventional structural control devices, the proposed SMARD is an attractive alternative in both performance and design efficiency.

5.2.1 Design of superelastic memory alloy re-centering damper (SMARD)

Due to the high strength of NiTiHfPd SMAs, a compact SMARD device with large force capacities can be easily designed by adjusting the total area of SMA bars used in the device. Here, the prototype SMARD will be designed to have a maximum force capacity of 3600 kN, a stroke of 150 mm and a loss factor of over 0.30. The loss factor, which is associated with energy dissipation of the device, is computed as dissipated energy per cycle (the area inside the hysteresis loop) divided by the product of 2π and maximum strain energy (the area under a complete cycle). The target design force can be achieved using four 25-mm diameter and four 25-mm diameter NiTiHfPd SMA bars in a single device, assuming the developed alloys will show super-elastic response up to a stress level of 2000 MPa. It should be noted that a SMARD with different diameters and length of SMA bars could be used to modify the damping, force and stroke capacities of the device. Thus, it provides an ability to tailor properties of SMARD for specific applications.

5.2.1.1 Design of SMA bars

Here, the SMARD is designed for a force and displacement capacity of 3600 kN and 150 mm respectively. According to the formula 5-1, to achieve these design objectives, the cross sectional area of the SMA bar is set to be:

$$A_{SingleSMA} = \frac{F}{\sigma} = \frac{900000}{1800} \approx 500\ mm^2 \quad (5\text{-}1)$$

Then SMA bar with the diameter of $D = 25\ mm$ is selected. The length of the SMA bars should be designed as well. Since all parts of the SMARD device, two groups of SMAs plus one group of friction springs, will be under compression, the possibility of the buckling for SMA bars should be considered in design using formula 5-2. The length of the SMA bar is selected to be $L = 200\ mm$ in order to avoid buckling.

$$P_{cr} = \frac{\pi^2 .\ E\ .\ I}{(k\ .\ L)^2} \quad (5\text{-}2)$$

Where P_{cr} stands for buckling force, E is the module of elasticity for the SMA bar, I is moment of inertia for the circle area of the SMA bar, $k\ .\ L$ is the effective length of the SMA sample bar. After calculating the critical loading, we concluded that with the selected length for the SMA bars bulking will be avoided. (See the formula 5-3)

$$P_{cr} = \frac{\pi^2 \times (78000) \times 19165}{(0.5 \times 200)^2} = 1473\ kN > 900\ kN \quad (5\text{-}3)$$

Therefore, the selected cross-sectional area corresponds to 2 group of 4 collection SMA bars with a diameter of 25 mm for each device.

5.2.1.2 Design of friction spring

Since the device will have force capacity of 3600 kN, 4 friction springs, with force capacity of 900 kN each, will be assembled in parallel with each other in the middle part of the device. Also, the required length of the friction spring in order to achieve maximum stroke capacity is 400 mm. The mechanical characteristics of the spring can be obtain accordingly. The spring used in this study consists of 12 elements type 24301 [124]. The deformation capacity of the single spring will be:

12.0 x 8.0 (S_e) = 96.0 mm, spring work (absorbed energy) will be: W_e = 3708.0 x 12 = 44,496 J, spring length will be: 12 x 33.3 (h_e) = 400 mm. By adding additional elements, the length of the spring, the absorbed energy (spring work) will be increased consequently but the end force will remain the same which is 900 kN for selected friction spring.

5.3 Steel moment frames with installed SMARD

5.3.1 Buildings description

5.3.1.1 A six-story building frame

In order to evaluate the performance of the proposed damper in mitigating seismic response of structures, 2 steel special moment resisting frames are chosen for this purpose. A six-story steel buildings illustrated in the FEMA P-751, NEHRP Recommended Seismic Provisions: Design Examples [125] is selected for numerical analyses. The building is designed as an office building located in Seattle, Washington on class C soil. The special steel moment-resisting frames on the perimeter of the building provide the lateral load resistance for the structure. The building consists of five bays at 8.53 m (28 feet) in the north–south (N–S) direction and six bays at 9.14 m (30 feet) in the east–west (E–W) direction. A plan and elevation of the building in the N–S direction are shown in Figure 5-3. All the analyses in this study are for lateral loads acting in the N–S direction. The story height is 3.81 m (12 feet-6 in.) at each floor except the first floor, which has a height of 4.57 m (15 feet). One of the perimeter steel special moment frames that serves as the seismic-force-resisting system of the structure is analyzed. All the columns in the N–S direction bend about their strong axis and the girders are attached with fully welded moment-resisting connections. The building is designed with Reduced Beam Section (RBS) connection details in accordance with design standards, ASCE/SEI 7-10 [121] and ANSI/AISC 360-10 [122]. The building is assigned to Seismic Design Category (SDC) D.

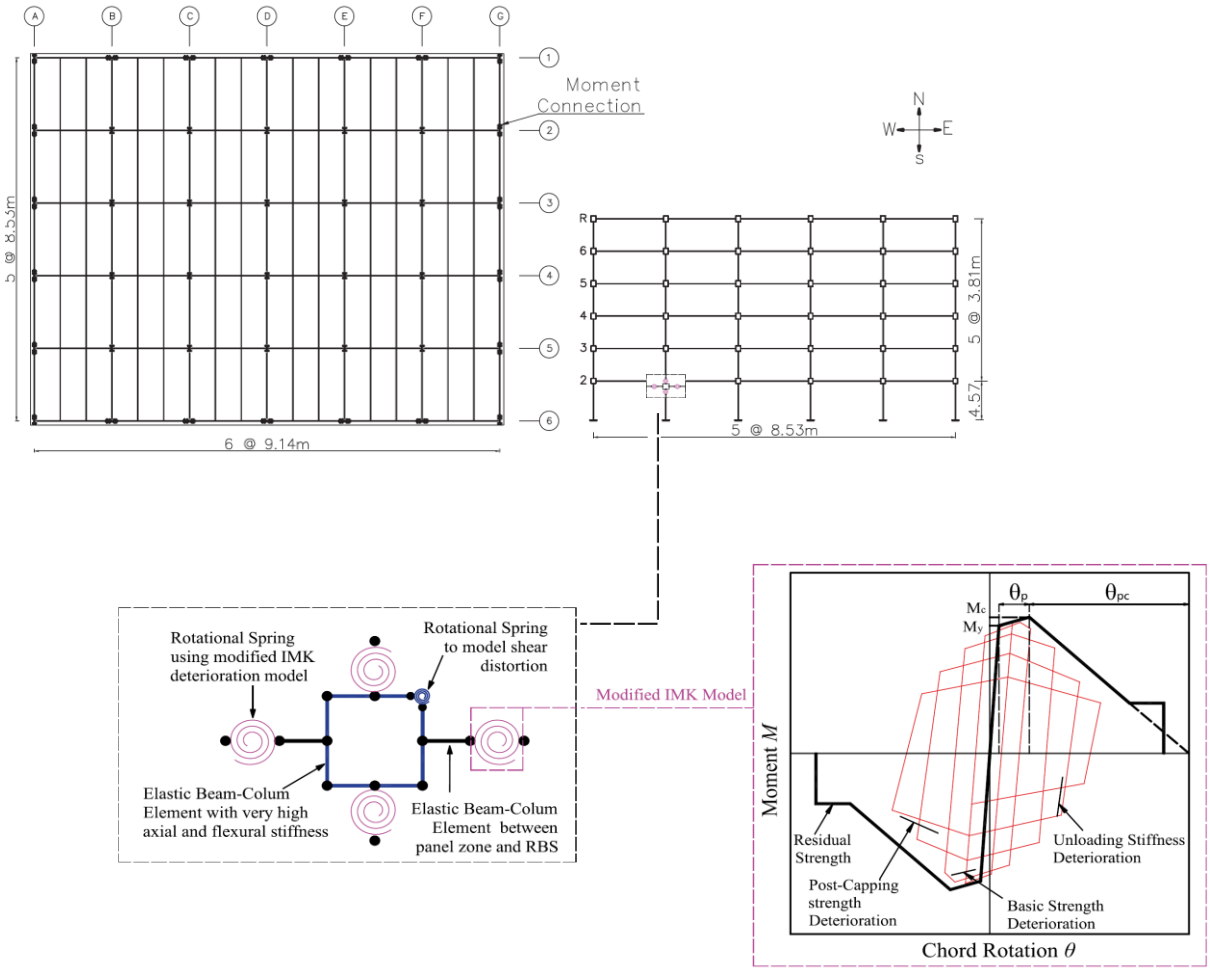

Figure 5-3 Six-story steel special moment resisting frame: (a) Plan (b) elevation of nine-story steel special moment resisting frame (c) modeling details.

The design spectral acceleration parameters are S_{DS} = 0.912 g and S_{D1} = 0.459 g, while the maximum considered spectral acceleration values are S_{MS} = 1.368 g and S_{M1} = 0.689 g. The seismic mass of the second level is 1.248 x 10^6 kg, the mass of the third level through sixth level is 1.242 x 10^6 kg and the mass of the roof level is 1.237 x 10^6 kg. The fundamental period of the structure is 2.04 s. The building was analyzed in FEMA P-751 through a nonlinear response history analysis and excessive story drifts were identified, especially at lower floor levels. A damping system was suggested to upgrade the performance of structure. In this study, the super-elastic memory alloy dampers will be installed to enhance the seismic response of the selected building.

5.3.1.2 A nine-story building frame

Also, a nine-story steel building [126] is selected from the SAC steel project for numerical analyses. The selected building includes a basement level in addition to the nine stories above the ground level and was originally designed as an office building located on a stiff soil site (Site Class D) in Seattle, Washington. A floor plan and elevation of the nine-story building are shown in Figure 5-4. The building has five bays at 9.15 m (30 ft) in each direction. The story height is 3.96 m (13 ft) at each floor except the first floor, which has a height of 5.49 m (18 ft) and the basement, which has a height of 3.65 m (12 ft). The lateral load resisting system in both directions consists of two special moment resisting frames on the perimeter of the building.

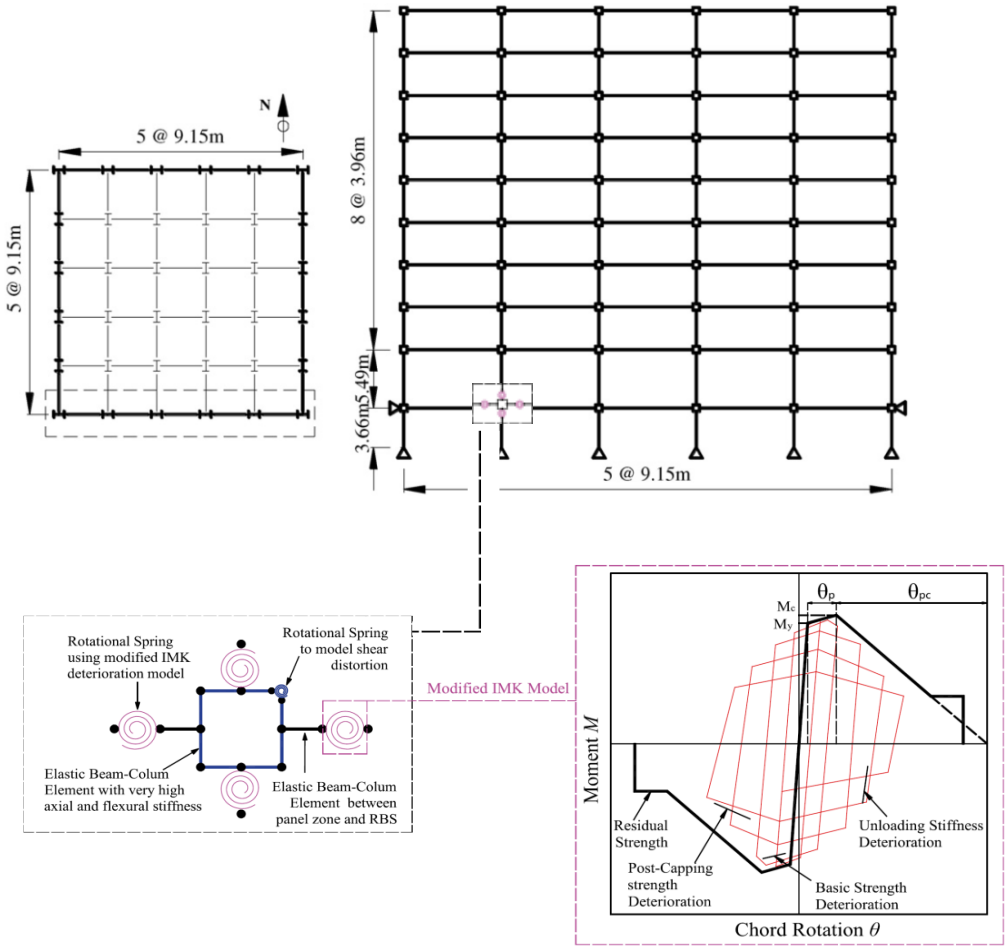

Figure 5-4 Nine-story steel special moment resisting frame: (a) Plan (b) elevation of nine-story steel special moment resisting frame (c) modeling details.

This study analyzes one of the moment frames in the E-W direction. The seismic masses are assigned as 1.01×10^6 kg for floor level 2, 9.89×10^5 kg for floor levels 3–9, and 1.07×10^6 kg for roof level. All the columns are assumed to be pinned at the base. The exterior columns at the ground level are also restrained laterally. The building is designed according to ASCE 7-10 [121] as a Risk Category II building by using nonlinear response history procedure. Based on the Seismic Design Category (SDC) D, the following design response spectral values are assigned to the site: S_{DS} = 0.912 g and S_{D1} = 0.530 g for the design basic earthquake (DBE), and S_{MS} =1. 368 g and S_{M1} = 0.795 g for the maximum considered earthquake (MCE).

The numerical model of the both steel frame buildings are developed in 2D using nonlinear seismic analysis program OpenSees [115]. Based on the concentrated plasticity concept, the beam and column elements are modeled with elastic beam-column elements connected by zero-length inelastic plastic hinges employing the modified Ibarra- Krawinkler deterioration model [127]. The modified Ibarra-Krawinkler deterioration model considers bilinear hysteric response behavior. The cyclic deterioration model parameters of the zero-length rotational springs are assigned based on the model parameters developed by Lignos and Krawinkler [128]. The deterioration characteristics of the rotational springs are indicated by yield strength, post-capping strength, unloading stiffness, and reloading stiffness. The moment-rotation curve is characterized by the elastic stiffness, plastic rotation, a post-capping plastic rotation capacity and the corresponding residual strength. The yield stress of structural steel is assumed to be equal to 375 MPa. To capture the important panel zone deformation modes, the panel zones are modeled considering the shear distortion in beam-column joints using Krawinkler model [129]. The Krawinkler model includes four rigid links and a rotational spring at the upper right corner to represent shear distortion in the panel zone. The nonlinear plastic hinges are created in beams at an offset from the interface of the panel zone and the beam element while the column plastic hinges are assigned at the face of the panel zone and the column element. To account for P-delta effects, a leaning column is linked to each model with elastic beam-column elements and connected to the model with an axially rigid truss element at each story level. The model assumes Rayleigh damping with a 2% damping ratio for the first and third modes.

Using the site's spectral acceleration values, the target spectra for the DBE and MCE levels are developed. A total of 7 ground motions is selected from PEER NGA database [130] as show in

Table 5-1 and scaled according to ASCE 7-10. In particular, the ground motions are scaled such that the average response spectra for the selected records is not less than the target response spectrum for periods ranging between 0.2 and 1.5 times the building fundamental period. The steel members of the nine-story building are selected in accordance with the strength requirements of ANSI/AISC 360–10 [122] under the load combinations provided in ASCE 7-10. The building is also designed to comply with the drift requirements of ASCE 7-10. Since a nonlinear response history is adopted for the design, the allowable story drift is increased by 25% and determined from ASCE 7-10 for Risk Category II buildings as 2.5% under DBE level and as 3.75% under MCE level.

Table 5-1 Seven ground motion records used in the design

No.	Earthquake	Station name	Magnitude (M_w)	Distance (km)	Peak ground acceleration (g)
1	Northridge (1994)	Canyon Country	6.7	12.4	0.40
2	Kocaeli, Turkey (1999)	Bolu	7.5	15.4	0.36
3	Superstition Hills-02 (1987)	El Centro Imp.	6.5	18.2	0.26
4	San Fernando (1971)	LA-Hollywood	6.6	22.8	0.19
5	Duzce, Turkey (1999)	Duzce	7.1	12.0	0.81
6	Loma Prieta (1989)	Gilroy Array	6.9	12.2	0.37
7	Imperial valley-06 (1979)	El Centro array	6.5	12.6	0.37

The selected column and beam sections for the nine-story frame are shown in Table 5-2. The building satisfies the drift requirements under both DBE and MCE levels as will be illustrated below. The first mode period of the six and nine story special moment resisting frames are 2.04s and 2.37 s respectively.

Table 5-2 Members of nine story steel moment resisting frames

	SMRF		SMRF with SMARD	
Story	Exterior/Interior Columns	Girders	Exterior/Interior Columns	Girders
1	W18x311	W21x201	W18x311	W21x201
2	W18x311	W21x201	W18x311	W21x201
3	W18x311	W21x201	W18x283	W21x182
4	W18x311	W21x201	W18x283	W21x182
5	W18x283	W21x182	W18x234	W18x192
6	W18x283	W21x182	W18x234	W18x192
7	W18x234	W18x192	W18x192	W18x143
8	W18x234	W18x192	W18x192	W18x143
9	W18x192	W18x175	W18x143	W18x130
R	W18x192	W18x175	W18x143	W18x130

5.3.2 Steel moment frames with SMARDs

In order to design the six-story and nine-story frame with damping systems, a reduced strength version of the fully code compliant frame is developed first. In particular, the beam and column member sizes are reduced such that the steel frame satisfies the strength requirements of the design codes but does not meet the drift limits. In this more flexible frame, the added dampers will carry a larger portion of the seismic loads and will be mainly responsible to control the story drifts. Table 5-2 provides the selected member sizes for the reduced strength frame. The reduced strength steel frame is first upgraded with SMARDs to comply with the story drift requirements of ASCE 7-10. In particular, the steel frame with SMARDs is designed using the nonlinear response history procedure and following the seismic design requirements for structures with damping systems described in Chapter 18 of ASCE 7-10.

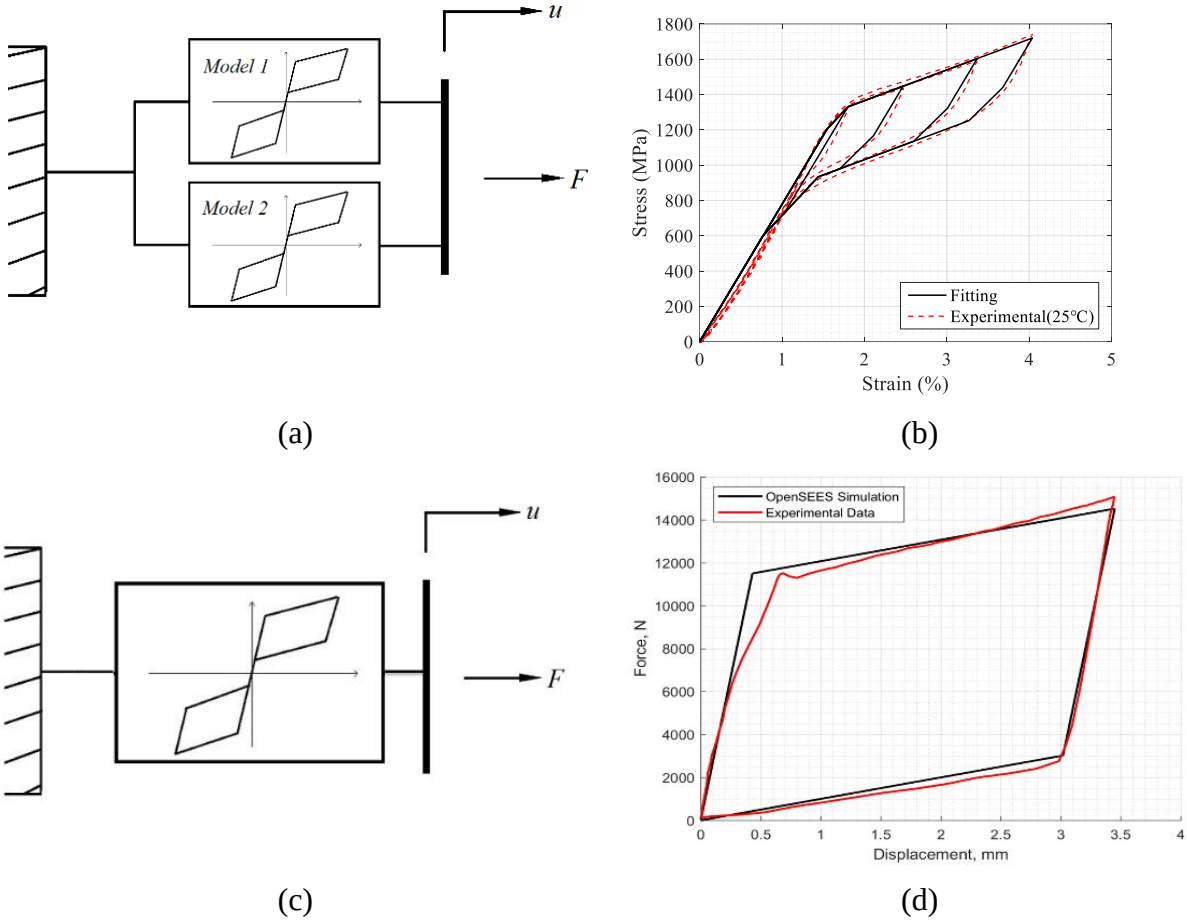

Figure 5-5 (a) A schematic representation for SMA bar model and (b) experimental stress–strain curve and model prediction at the temperature of +25°C for SMA (c) A schematic representation for friction spring model and (d) experimental force-deformation curve and model prediction for friction damper

To model hysteretic response of NiTiHfPd SMAs at different temperatures and friction spring a mechanical model is proposed in Open System for Earthquake Engineering Simulation (OpenSees) [115]. The model consists of two self-centering materials placed in parallel for the SMAs as shown in Figure 5-5 (a) is proposed. The use of two self-centering element instead of one for the SMAs provides more accurate modeling of the material response, especially for inner loops. Since the SMAs will be subjected to dynamic loading during an earthquake, the experimental responses of SMAs at 1 Hz are used for the numerical modeling. The selected parameters of the proposed model under the three temperatures of 25°C, 5°C and -35°C are given in Table 5-3. Figure 5-5 (b) shows the hysteretic curves predicted by the proposed model and experimental response at the temperature of 25°C for the SMAS. Figure 5-5 (c-d) also shows the proposed model and

experimental response for friction spring. The model consists of one self-centering material for friction spring. It can be seen that two proposed model can predict the response of NiTiHfPd SMA Material very well.

Table 5-3 Parameters of proposed SMA model

Temperature	25°C		5°C		-35°C	
Model	1	2	1	2	1	2
Initial stiffness (MPa/%)	370	410	234.4	377	370	230
Post-transformation stiffness (MPa/%)	87	87	67.4	67.4	50	50
Forward transformation stress (MPa)	570	738	410.2	829.4	629	505
Ratio of forward to reverse activation stress (β)	0.50	0.20	0.70	0.29	0.80	0.40

The model of the shape memory alloy-based re-centering damper is developed in OpenSees by combining two finite length elements with uniaxial self- centering material property to represent the SMAs and one finite length element with uniaxial self-centering material property to model the friction spring compound. The self-centering material exhibits flag-shaped hysteric response and captures the post-transformation hardening behavior with a post-hardening stiffness equals to the initial stiffness. The experimental test results of SMAs and friction spring compound are used to develop model parameters (see Figure 5-5) for the SMA and friction spring compound. The selected parameters for the self-centering material model of the SMAs are as follows: initial stiffness k_1 = 61.23 kN/mm, post-activation stiffness k_2 = 13.80 kN/mm, ratio of post-transformation hardening stiffness to initial stiffness γ =1.0, forward activation force Fa=104.01 kN and ratio of forward to reverse activation force β=0.35. The selected parameters for the self-centering material model of the friction springs are as follows: initial stiffness k_1 = 28.75 kN/mm, post-activation stiffness k_2 = 0.9677 kN/mm, ratio of post-transformation hardening stiffness to initial stiffness γ =1.0, forward activation force Fa=11.50 kN and ratio of forward to reverse activation force β=1.0.

For the six story building, the SMARDs are installed at two bay at each story level. The design parameters described in Section 6 are used for the SMARDs and these properties are set to be fixed for each device. The same numbers of dampers are assumed to be installed at each bay of a given floor. According to the Figure 5-6 the SMARDs are installed at the second and fourth bay of each story level using a chevron brace configuration. Because the SMARD device has high force capacity, the number of damper for each story is selected to be 2 to satisfy the drift requirement. The average response of the building with the installed dampers under the selected 7 ground motions satisfies the member strength criteria and 2% drift requirements of the ASCE SEI 7-10. The fundamental period of the six story steel frame with the installed damper is 1.29 s.

For the nine story building the SMARDs are installed at the second and fourth bay of each story level, Figure 5-7, using a chevron brace configuration as well. From the nonlinear time history analyses, the number of dampers for each story is selected to be 2 to meet the drift requirements. The fundamental period of the nine-story frame with the installed SMARDs is 2.19 s.

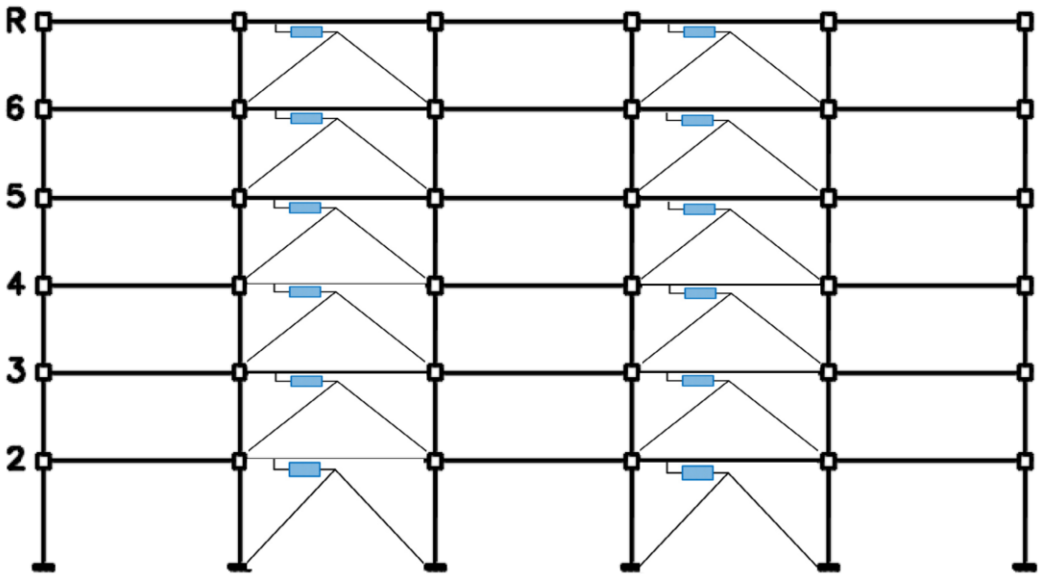

Figure 5-6 SMARD device installed into six-story steel frame

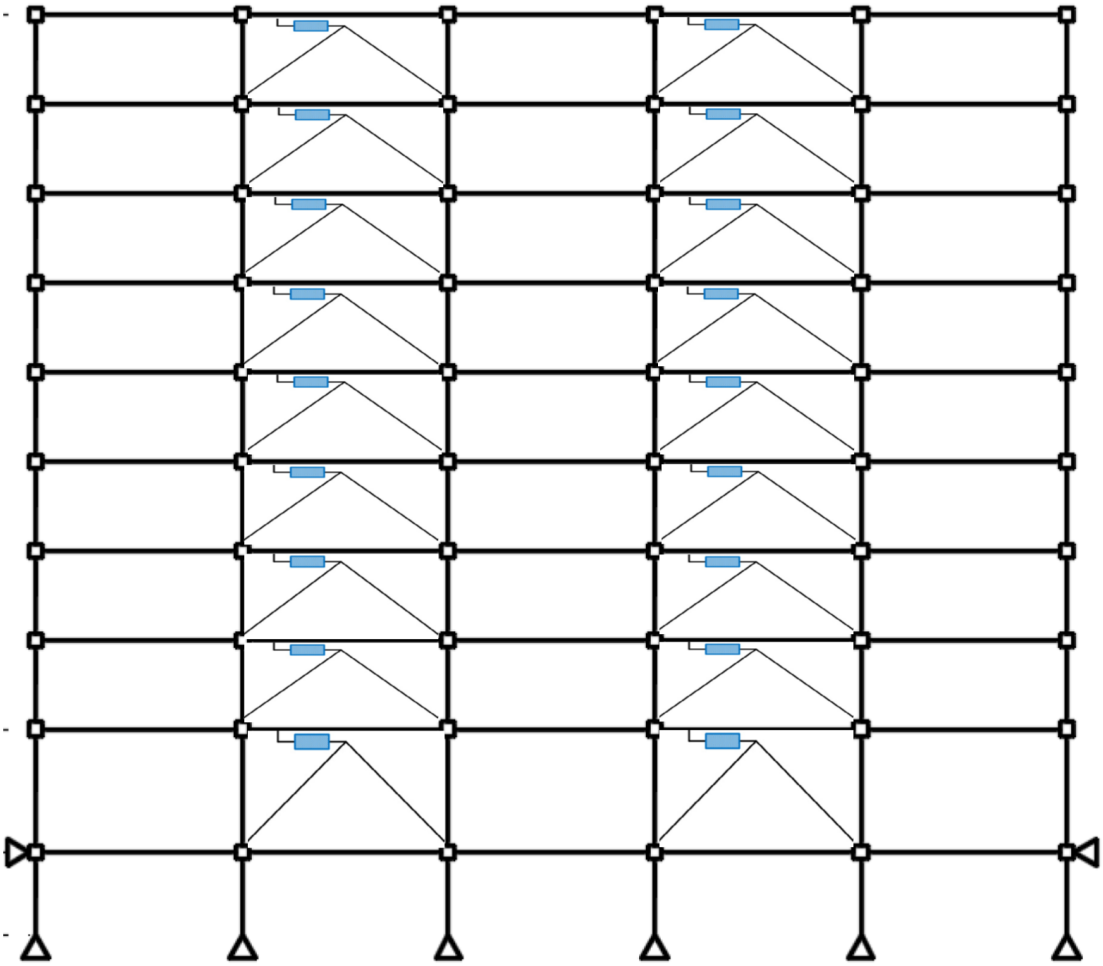

Figure 5-7 SMARD device installed into nine-story steel frame

The mean story drifts for the SMRF and the steel frame with SMARDs under 7 design ground motions are provided in Table 5-4 for the DBE and MCE levels. Note that each frame is designed such that the peak inter-story drift obtained from nonlinear response history procedure meets the code drift requirements without aiming to achieve any higher seismic performance objective.

Table 5-4 Drift response of developed frames under design earthquake records

Model	T_1 (s)	Mean inter-story drift			
		DBE		MCE	
		Design (%)	Limit (%)	Limit (%)	Limit (%)
SMRF (6-story)	2.04	2.38	2.5	3.21	3.75
SMRF (9-story)	2.37	2.44		3.25	
6-story SMARDs	1.29	2.34		3.19	
9-story SMARDs	2.19	2.39		3.51	

5.4 Performance assessment of steel frame buildings

In this study, a set of 22 far-field ground motion pairs used in the FEMA P695 methodology [118] is employed in this study for extensive nonlinear time history analyses for both buildings. The set represents strong ground motions with PGA N 0.2 g and PGV N 15 cm/s that range in event magnitude from M6.5 to M7.6 and from stiff soils (site Class D) and very stiff soil sites (site Class C). The ground motions are normalized to eliminate unwarranted variability between records. The ground motion records are collectively scaled to selected hazard level, as defined in ASCE/SEI 7-05, such that the median spectral acceleration of the record set matches with those of the design spectra at the fundamental period of each six and nine story frame (i.e. at 2.04 s for the uncontrolled six story frame and 1.29 s for the controlled six story frame. Also, at 2.37 s for the uncontrolled nine story frame and 2.19 s for the controlled nine story frame). Peak inter-story drift ratio, which is correlated with damage in structural elements; peak absolute floor acceleration, which is correlated with damage in non-structural components; and peak residual story drift ratio, which is related to the post-earthquake functionality of the structure are selected as the desired response quantities. Residual story drifts are calculated by continuing the analyses for at least 20 s after the end of the seismic event. As previous probability based studies suggested 10% inter-story drift ratio is considered to define the collapse in numerical simulations [127].

5.4.1 Six-story steel building frame

Structural responses of the uncontrolled building and the building with installed SMAs based dampers are computed under each ground motion record at two seismic hazard levels. Figures 5-

8 and 5-9 illustrate the peak inter-story drift ratio, peak residual inter-story drift ratio, and peak floor absolute acceleration for the uncontrolled and controlled buildings under DBE and MCE level ground motion records, respectively. It can be seen that the installed SMARDs reduces the drift demand of the six-story building under all DBE level earthquakes. For uncontrolled structure, the failure of the building is observed under nine ground motion records at the DBE level.

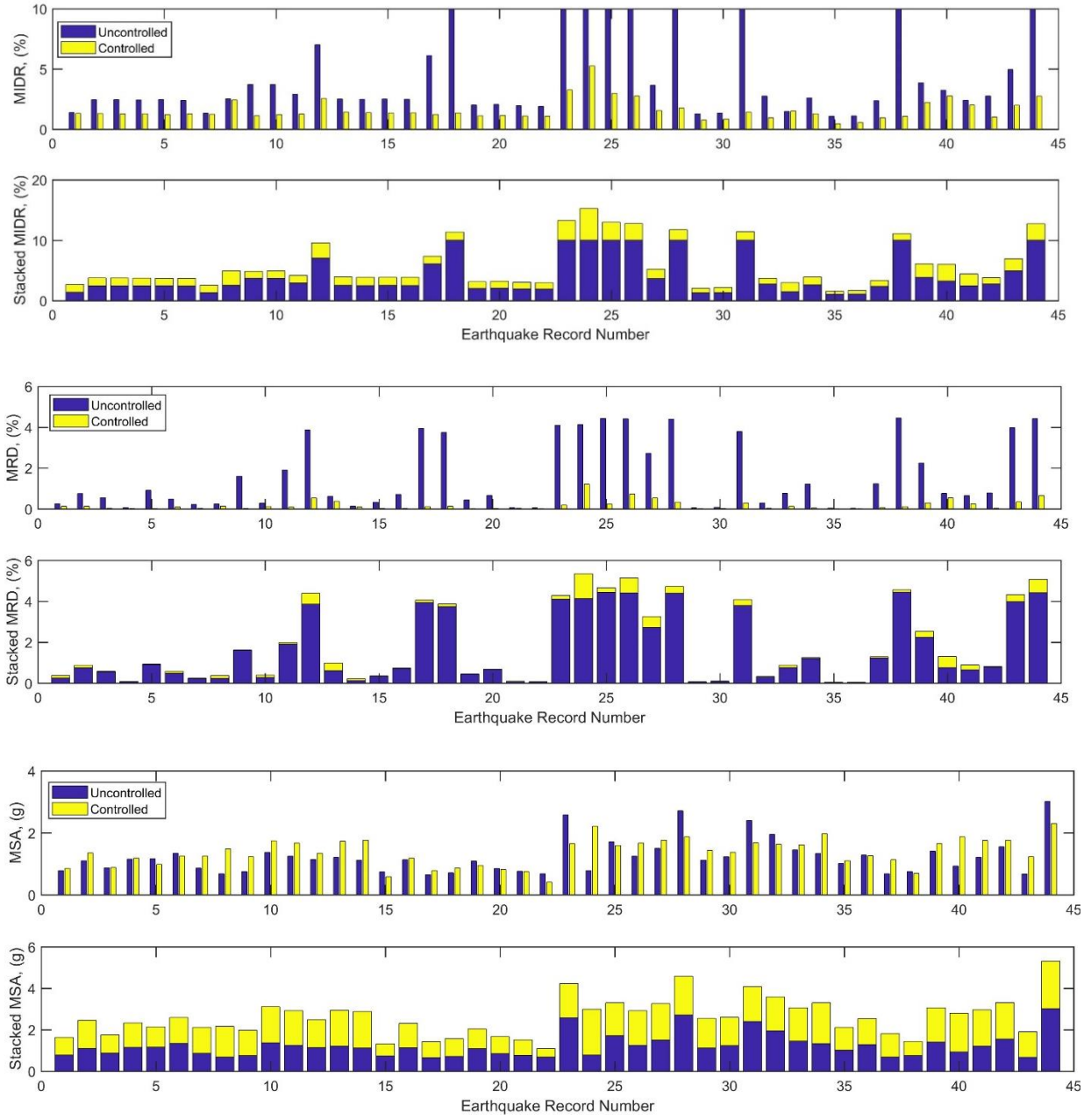

Figure 5-8 Peak inter-story drift, peak residual story drift, and peak story acceleration for individual DBE level ground motions.

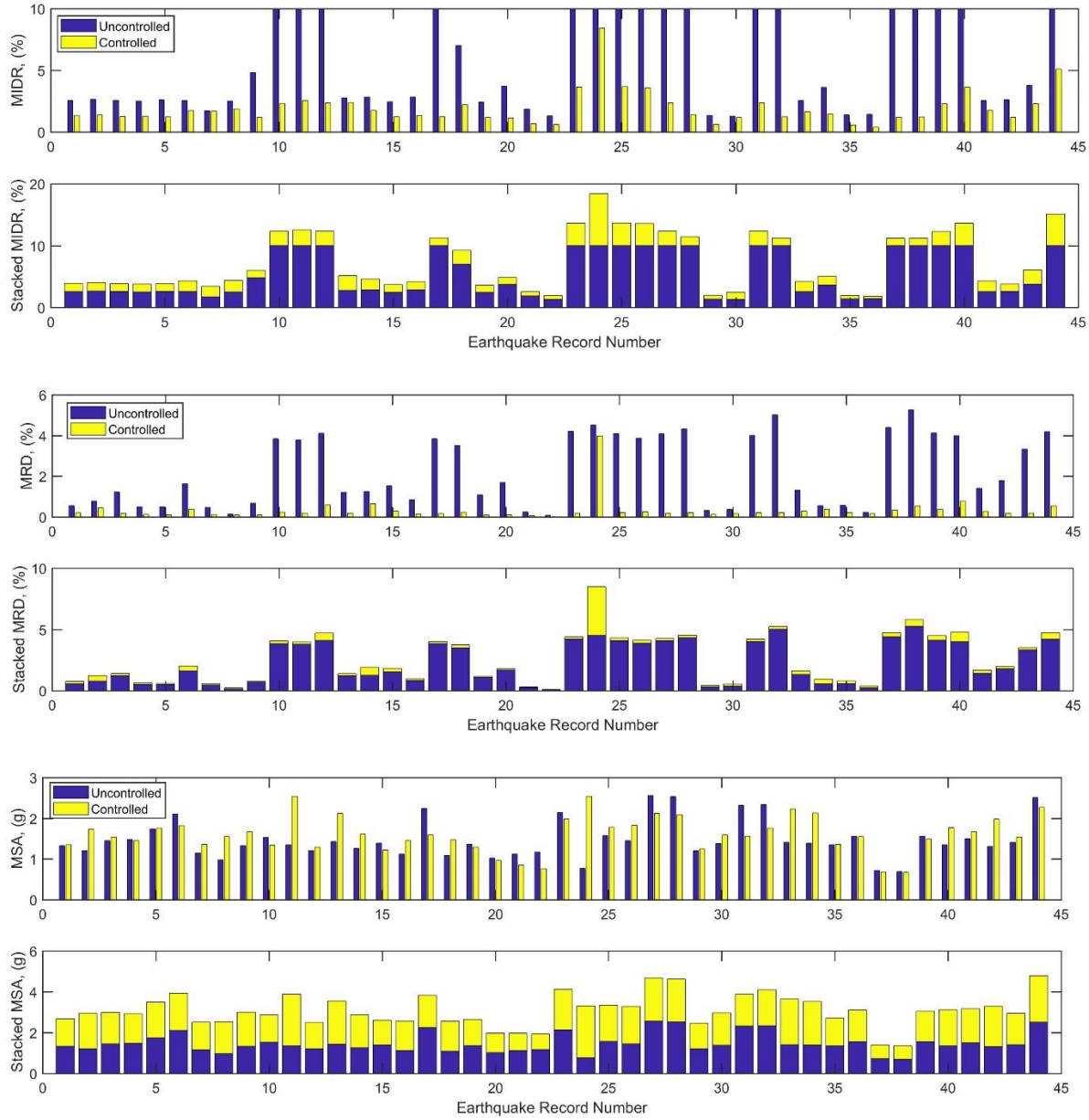

Figure 5-9 Peak inter-story drift, peak residual story drift, and peak story acceleration for individual MCE level ground motions.

Based on the formula 5-4, as the distribution of seismic response is typically assumed to follow a lognormal distribution, the statistics of the peak inter-story drift ratio and peak story absolute acceleration response under 44 ground motion records are provided in terms of median (50 percentile) and 84 percentile response and calculated as formula 5-5:

$$\widehat{X} = \exp\left(\frac{\sum_{i=1}^{n} \ln x_i}{n}\right) \qquad (5-4)$$

$$x^{84} = \widehat{X} \exp(\sigma_{lnX}) \qquad (5-5)$$

Where n is the number of response data points and σ_{lnX} is the standard deviation of the logarithm of response X. Figure 5-10 shows the median and 84-percentile values of the peak inter-story drift ratio and peak story absolute acceleration at each floor level for the uncontrolled and controlled buildings to the DBE and MCE levels.

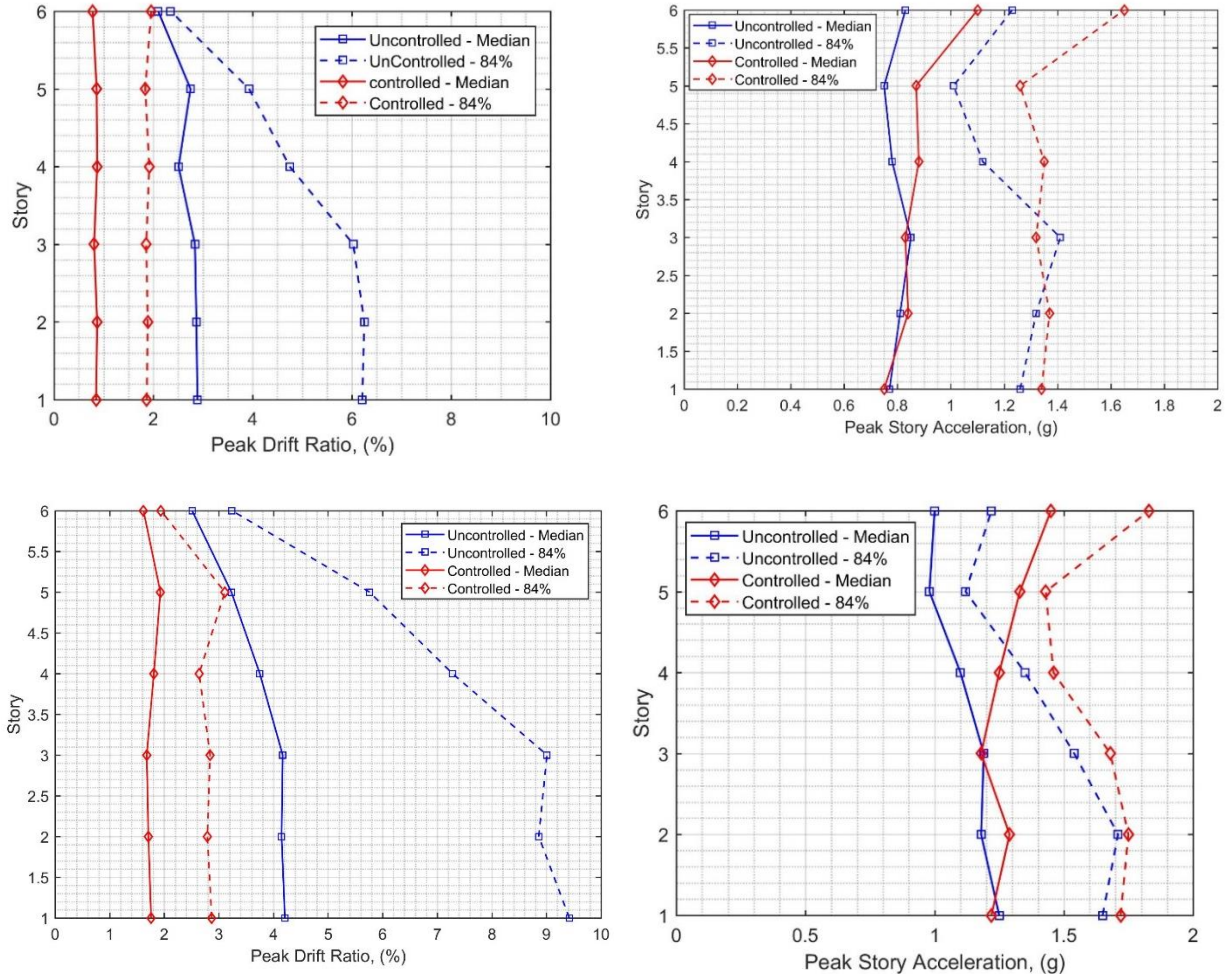

Figure 5-10 Statistics of peak inter-story drift ratio and peak story absolute acceleration for uncontrolled and controlled buildings subjected to 44 ground motions at (a) DBE level and (b) MCE level.

It can be discerned that peak inter-story drift attain smaller values for the controlled structure at all the floors for both DBE and MCE hazard levels. The peak median peak inter-story drift ratio

reaches about 2.89% and 4.21% for the uncontrolled structure for the DBE and MCE levels, respectively. On the other hand, the median peak inter-story drift ratio is uniformly distributed along the height of the structure for the controlled frame with a maximum of 0.87% and 1.93% for the DBE and MCE levels, respectively. That clearly shows the effectiveness of SMARDs in reducing the displacement response of the steel building, especially at high seismic hazard levels. Moreover, the maximum 84-percentile inter-story drift ratios for the conventional frame are 6.25% and 9.42% for the DBE and MCE, respectively. The corresponding values are only 1.92% and 3.11% for the steel frame with SVDs.

The peak acceleration response moderately goes up for the steel frame with the installed SMARD dampers. The peak median accelerations for the uncontrolled frame are 0.85 g and 1.25 g and the peak 84-percentile acceleration values are 1.32 g and 1.71 g for the DBE and MCE, respectively. For the controlled frame, the median values are 0.88 g and 1.45 g at DBE and the peak 84-percentile acceleration values are 1.65 g and 1.83 g at MCE.

5.4.2 Nine-story steel building frame

For the nine-story building again structural responses of the uncontrolled building and the building with installed SMAs based dampers are calculated under each ground motion record at one seismic hazard level. To facilitate performance assessment of SMRF and SMARD systems comparatively, the envelopes for the median of peak response quantities under 44 ground-motion records for each system are also provided in Figure 5-11. It can be seen that each frame satisfactorily limits the peak inter story drift response under various MCE level ground motions. The SMRF frame typically has larger record-to-record variability in structural response, while the use of SMARDs reduces the scatter in response. The peak median responses are 2.32% and 1.92% for the SMRF and SMARD frames, respectively. The maximum values of the peak floor absolute acceleration responses are 1.09 g and 1.15 g for the SMRF and SMARD frames, respectively. The SMARD frame also has minimal residual drifts over the height of the 9-story frame, whereas the SMRF system has considerable residual deformations.

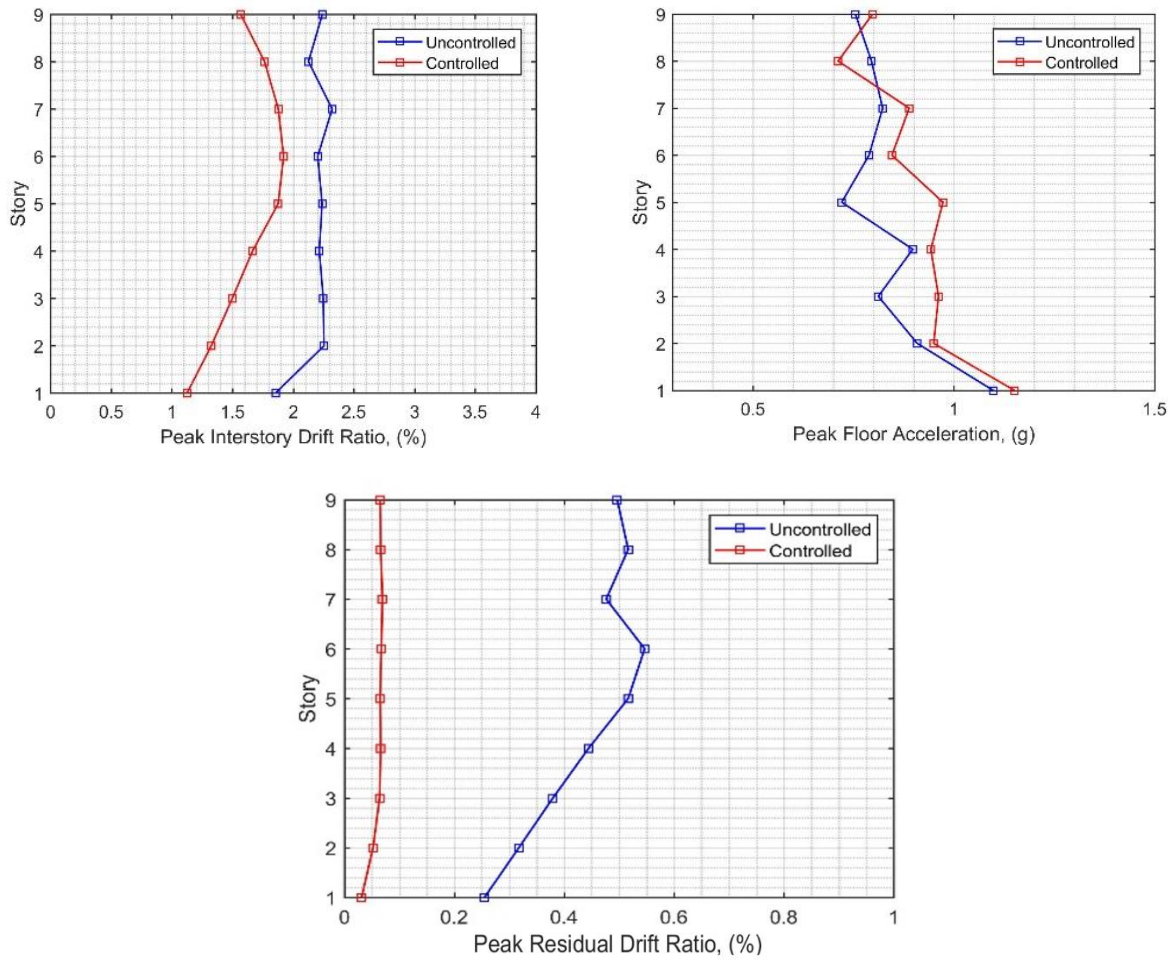

Figure 5-11 Envelopes for median of peak response quantities for SMRF and SMARD, frames at MCE level.

5.5 Closure

In this chapter, NiTiHfPd alloy plus friction spring are employed, as two essential compounds of a structural passive control system, into two steel frame buildings to provide re-centering and energy-dissipating capabilities. First, experimental tests on NiTiHfPd alloys that have ultra-high strength, large damping capacity, and wide operating temperature range are discussed. Impact of different range of temperatures on Mechanical behavior of the SMA bars are explored. Also, experimental tests on friction springs that have high force and large deformation capacity are discussed. A super-elastic memory alloy re-centering damper device, which advantages the inherent re-centering capability of high performance SMA bars and high energy dissipation ability of friction spring compound for superior seismic performance, is proposed in this study. A high damped friction spring compound, which provides high damping as well as high deformation capability, is considered for the re-centering and energy dissipation component of the hybrid damper, named as super-elastic memory alloy re-centering damper. Experimental tests on the subcomponents of the SMARD device, i.e. friction spring compound and high performance SMA bars, are carried out to characterize their mechanical response. Performance and effectiveness of the proposed damper in mitigating response of steel frame buildings under DBE and MCE level seismic loads are assessed through numerical studies. A six-story and nine-story special steel moment frame structure is modeled as conventional moment resisting frame and the frame with installed as super-elastic memory alloy re-centering dampers. A suite of 44 strong ground motion records are normalized and scaled as described in FEMA P695. Nonlinear response history analyses are conducted and the peak response quantities are evaluated. Results show that the inter-story drift demands and residual drifts of the buildings subjected to DBE and MCE level earthquakes can significantly be reduced with installed SMARDs without a considerable increase in peak acceleration demand. However, future studies are needed to experimentally verify the response of the proposed device and study the effect of temperature on the response of the new passive control device.

6 Conclusions and Recommendations

6.1 Conclusions

This thesis presents experimental and analytical studies that explored the feasibility of using new type of shape memory alloy material, namely NiTiHfPd alloys, in passive structural control systems as well as bracing systems, for improving the response of structures especially buildings during earthquakes.

First of all, experimental tests are conducted to characterize the behavior of NiTiHfPd SMA bars at various temperatures and loading frequencies. The results indicate that the temperature and loading rate have significant effects on the behavior of NiTiHfPd bars. Experimental tests also carried out to characterize the behavior of friction springs. The results show that friction spring own high energy dissipation capability as well as large deformation and force capacity which makes it promising component in passive structural control systems.

Second, In order to evaluate the performance of new SMA material in bracing systems, NiTiHfPd alloy is employed as a bracing system in a steel frame building to provide re-centering and energy-dissipating capabilities. A case-study steel building is selected and modeled for numerical investigations. The selected steel moment resisting frame building is also designed and modeled with SMA bracing system such that the SMA-braced frame has comparable strength and stiffness with the original SMRF. Nonlinear response history analyses on conventional SMRF and SMA-braced frame are conducted at different seismic intensity levels using a set of ground motion records. The results indicate that the residual story drifts can significantly be reduced when the steel building are designed with SMA-bracing systems. It is also found that changing temperature between -35°C and +25°C does not affect the performance of NiTiHfPd SMA bracing systems.

Third, an investigations of a shape memory alloy-based self-centering system, termed as a superelastic memory alloy re-centering damper (SMARD), to mitigate the structural responses of steel building structures subjected to multi-level seismic hazards. The superelastic memory alloy re-centering dampers leverage the inherent re-centering capability of shape memory alloy bars, using new kind of SMA material named as NiTiHfPd, and the energy dissipation, re-centering capability and deformation ability of a friction spring compound, which provides high damping and large deformation, for superior seismic performance. The SMA bars recently developed as a new structural element exploit the excellent mechanical properties in order to resist large axial

loads. They possess advantageous characteristics, such as large compression strength, ability to fully recover deformations up to 6% strain. A set of numerical studies is conducted to evaluate the efficiency of the SMARDs in controlling the response of steel frame buildings. All numerical models are developed using the nonlinear seismic analysis program OpenSees. All building models capture the degradation of structural strength and stiffness of the steel frame elements associated with structural damage. The model parameters for the SMA bars and the friction spring compound are selected based on the experimental test results on the NiTiHfPd SMAs and friction spring compound. A six-story and a nine-story special steel moment frame structure, which exhibits excessive story drifts, is designed using SMARDs. Nonlinear response history analyses are conducted, and the peak response quantities of both the initial frames and upgraded frames with installed SMARDs are evaluated under a suite of 44 far-field strong ground motion records.

The results from these investigations revealed that steel frame buildings designed with SMARD systems can considerably improve structural performance, especially at high seismic hazard levels. Residual drifts are significantly reduced for the frames with SMARDs. Thus, the application of SMARDs in building structures can significantly reduce aftermath post-earthquake losses and buildings can operate after even high seismic hazard levels.

6.2 Recommendations for future studies

The last part of the current study investigates the seismic performance of a superelastic memory alloy re-centering damper through numerical simulations in steel building structures. Future studies of the proposed device need to conduct experimental investigations to strengthen further understanding of the behavior and performance by testing a prototype device in the laboratory. Furthermore, additional analytical studies can be conducted to evaluate the performance of the proposed device installed in steel building structures having different story configurations.

Considering the effect of degradation in SMARD response under cyclic loading in addition to the inclusion of strength and stiffness degradation of beam and column elements needed to be investigated. Also, the proposed study is focused on the seismic performance evaluation of steel frame structures. Hence, future study can also be extended to evaluate the performance of reinforced concrete frame structures with installed SMARD devices. Furthermore, future research work can be extended to evaluate the performance of SMARD devices installed in buildings subjected to near field-ground motions. Finally, a 3D analysis can provide more accurate insight

into understanding of the behavior and performance of the buildings with and without installed SMARD devices. Therefore, the 3D analyses under bi-axial ground motion records must be considered in future studies.

REFERENCES

1. Symans, M.D., Charney, F. A., Whittaker, A.S., Constantinou, M.C., Kircher, C.A., Johnson, M.W., and McNamara, R.J. Energy dissipation systems for seismic applications: current practice and recent developments. Journal of Structural Engineering, 134(1), 3-21, 2008.
2. Soong, T.T., and Dargush, G.F. Passive energy dissipation system structural engineering. Wiley, Chichester, 1997.
3. Marshall, J. D., and Charney, F. A. Seismic response of steel frame structures with hybrid passive control systems. Earthquake Engineering & Structural Dynamics, 41(4), 715-733, 2012.
4. Chancellor, N.B., Eatherton, M.R., Roke, D.A. and Akbaş, T. Self-centering seismic lateral force resisting systems: high performance structures for the city of tomorrow. Buildings, 4(3), 520-548, 2014.
5. Ozbulut, O. E., Mir C., Moroni, M. O., Sarrazin, M., and Roschke, P. N. A fuzzy model of superelastic shape memory alloys for vibration control in civil engineering applications. Smart Materials and Structures, 16, 818-829, 2007.
6. Qiu CX, Zhu S. Performance-based seismic design of self-centering steel frames with SMA-based braces. Engineering Structures, 130, 67-82, 2017.
7. Gao, N., Jeon, J.S., Hodgson, D.E. and DesRoches, R. An innovative seismic bracing system based on a superelastic shape memory alloy ring. Smart Materials and Structures, 25(5), p.055030, 2016.
8. Ozbulut, O. E., Roschke, P.N., Lin, P.Y., and Loh, C.H. GA-based optimum design of a shape memory alloy device for seismic response mitigation. Smart Materials and Structures, 19, 065004, 1-14, 2010.
9. Ozbulut, O. E., and Hurlebaus, S. Application of an SMA-based hybrid control device to 20-story nonlinear benchmark building. Earthquake Engineering & Structural Dynamics, 41, 1831-1843, 2012.
10. Mishra, S.K., Gur, S. and Chakraborty, S. An improved tuned mass damper (SMA-TMD) assisted by a shape memory alloy spring. Smart Materials and Structures, 22(9), p.095016, 2013.
11. Parulekar, Y.M., Kiran, A.R., Reddy, G.R., Singh, R.K. and Vaze, K.K. Shake table tests and analytical simulations of a steel structure with shape memory alloy dampers. Smart Materials and Structures, 23(12), p.125002, 2014.
12. Ozbulut, O. E., and Hurlebaus, S. A comparative study on seismic performance of superelastic-friction base isolators against near-field earthquakes. Earthquake Spectra, 28, 1147-1163, 2012.
13. Ozbulut, O. E., and Hurlebaus, S. Energy-balance assessment of shape memory alloy-based seismic isolation devices." Smart Structures and Systems, 8, 399-412, 2011.
14. Ozbulut, O. E., and Hurlebaus, S. Seismic assessment of bridge structures isolated by a shape memory alloy/rubberbased isolation system." Smart Materials and Structures, 20, 015003, 1-12, 2011.
15. Dezfuli, F.H. and Alam, M.S. Shape memory alloy wire-based smart natural rubber bearing. Smart Materials and Structures, 22(4), p.045013, 2013.
16. Ghodke, S. and Jangid, R.S. Influence of high austenite stiffness of shape memory alloy on the response of baseisolated benchmark building. Structural Control and Health Monitoring, doi: 10.1002/stc.1867, 2016.
17. Dolce, M., Cardone, D., and Marnetto, R. Implementation and testing of passive control devices based on shape memory alloys. Earthquake Engineering and Structural Dynamics, 29, 945-968, 2000.
18. Zhu, S., and Zhang Y. Seismic behaviour of self-centring braced frame buildings with reusable hysteretic damping brace. Earthquake Engineering and Structural Dynamics, 36, 1329-1346, 2007.
19. Ozbulut, O. E., and Hurlebaus, S. Re-centering variable friction device for vibration control of structures subjected to near-field earthquakes. Mechanical Systems and Signal Processing, 25, 2849-2862, 2011.

20. Ozbulut, O. E., Bitaraf, M., and Hurlebaus, S. Adaptive control of base-isolated structures against near-field earthquakes using variable friction dampers. Engineering Structures, 33, 3143-3154, 2011.
21. Yang, C.W., DesRoches, R., and Leon, R.T. Design and analysis of braced frames with shape memory alloy and energy-absorbing hybrid devices. Engineering Structures, 32, 498-507, 2010.
22. Silwal, B., Michael, R. J., and Ozbulut, O. E. A superelastic viscous damper for enhanced seismic performance of steel frame structures. Engineering Structures, 105, 152-164, 2015.
23. Silwal, B., and Ozbulut, O. E., and Michael, R. J. Seismic collapse evaluation of steel moment resisting frames with superelastic viscous damper." Journal of Constructional Steel Research, 126, 26-36, 2016.
24. Miller, D.J., Fahnestock, L.A., and Eatherton, M.R. Development and experimental validation of a nickel–titanium shape memory alloy self-centering buckling-restrained brace. Engineering Structure 40, 288-298, 2012.
25. Karaca, H., et al., Superelastic response and damping capacity of ultrahigh-strength [111]-oriented NiTiHfPd single crystals. Scripta Materialia, 2012. 67(5): p. 447-450.
26. Graesser, E. J., Cozzarelli, F. A. (1991). "Shape-memory alloys as new materials for aseismic isolation." Journal of Engineering Mechanics, 117(11), 2590-608.
27. T. Yoneyama, S. Miyazaki, Shape Memory Alloys for Biomedical Applications, Elsevier, 2008.
28. A. Rao, A.R. Srinivasa, J.N. Reddy, Design of Shape Memory alloy (SMA) Actuators, Springer, 2015.
29. Toker, Guher P., et al. "Shape memory behavior of Ni40. 3Ti39. 7Hf15Pd5 and Ni40. 3Ti44. 7Hf10Pd5 alloys." Journal of Alloys and Compounds (2018).
30. E. Acar, O.E. Ozbulut, H.E. Karaca, Experimental investigation and modeling of the loading rate and temperature dependent superelastic response of a high performance shape-memory alloy, Smart Mater. Struct. 24 (7) (2015) 075020.
31. M. Elahinia, Shape Memory alloy Actuators: Design, Fabrication and Experimental Evaluation, John Wiley & Sons, 2015.
32. Otsuka K and Wayman C M 1998 Shape Memory Materials (Cambridge: Cambridge University Press)
33. Schwartz M 2008 Smart Materials (Boca Raton, FL: CRC Press)
34. Otsuka K and Ren X B 1999 Recent developments in the research of shape memory alloys Intermetallics 7 511–28
35. Bachmann F et al 2012 Passive damping of composite blades using embedded piezoelectric modules or shape memory alloy wires: a comparative study Smart Mater. Struct. 21 075027
36. Ozbulut O E and Hurlebaus S 2011 Seismic assessment of bridge structures isolated by a shape memory alloy/rubberbased isolation system Smart Mater. Struct. 20 015003
37. Ozbulut O E, Roschke P N, Lin P Y and Loh C H 2010 GAbased optimum design of a shape memory alloy device for seismic response mitigation Smart Mater. Struct. 19 065004
38. Ozbulut O E, Hurlebaus S and Desroches R 2011 Seismic response control using shape memory alloys: a review J. Intell. Mater. Sys. Struct. 22 1531–49
39. Yamauchi K, Ohkata I, Tsuchiya K and Miyazaki S 2011 Shape Memory and Superelastic Alloys: Technologies and Applications (Cambridge: Woodhead Publishing)
40. Noebe R D, Tiffany B and Padula S A II 2006 NiTi-Based High-Temperature Shape-Memory Alloys Advanced Structural Materials (Boca Raton, FL: CRC Press) 145–86
41. LeBlanc L 2001 Part I –'Smart metals' providing actuation, sealing, and completion functions downhole Offshore 61 58–9
42. LeBlanc L 2002 Part II -'Smart metals' providing actuation, sealing, and completion functions downhole Offshore 62 54–6
43. Miyazaki S, Mizukoshi K, Ueki T, Sakuma T and Liu Y 1999 Fatigue life of Ti–50 at.% Ni and Ti–40Ni–10Cu (at.%) shape memory alloy wires Mater. Sci. Eng. A 273–5 658–63

44. Otsuka K and Ren X B 2005 Physical metallurgy of Ti-Nibased shape memory alloys Prog. Mater. Sci. 50 511–678
45. Padula S A II et al 2012 Effect of upper-cycle temperature on the load-biased, strain-temperature response of NiTi Metall. Mater. Trans. A 43 4610–21
46. Karaca, H. E., et al. "Shape memory behavior of high strength NiTiHfPd polycrystalline alloys." Acta Materialia 61.13 (2013): 5036-5049.
47. Acar, Emre, Osman E. Ozbulut, and Haluk E. Karaca. "Experimental investigation and modeling of the loading rate and temperature dependent superelastic response of a high performance shape-memory alloy." Smart Materials and Structures 24.7 (2015): 075020.
48. Araki, Y., Maekawa, N, Omori, T., Sutou, Y., Kainuma, R., and Ishida, K. (2012). "Rate-dependent response of superelastic Cu–Al–Mn alloy rods to tensile cyclic loads." Smart Mater. Struct, 21(3), 032002.
49. Tanaka, Y., et al., Ferrous polycrystalline shape-memory alloy showing huge superelasticity. Science, 2010. 327(5972): p. 1488-1490.
50. Otsuka, K. and X. Ren, Physical metallurgy of Ti–Ni-based shape memory alloys. Progress in materials science, 2005. 50(5): p. 511-678.
51. Karaca, H., et al., Compressive response of nickel-rich NiTiHf high-temperature shape memory single crystals along the [111] orientation. Scripta Materialia, 2011. 65(7): p. 577-580. [29]
52. Karaca, H., et al., NiTiHf-based shape memory alloys. Materials Science and Technology, 2014. 30(13a): p. 1530-1544.
53. Karaca, H., et al., Effects of aging on [111] oriented NiTiHfPd single crystals under compression. Scripta Materialia, 2012. 67(7): p. 728-731
54. Billah, A. H. M. M. D. (2015). "Performance-based seismic design and assessment of concrete bridge piers reinforced with shape memory alloy rebar" *Doctoral dissertation*, University of British Columbia).
55. Lin H, He J, Chen K, Liao H, Lin K. Metall Mater Trans A 1997; 28:1871.
56. DellaCorte C, Pepper SV, Noebe R, Hull DR, Glennon G. NASA TM-2009-215646; 2009.
57. Dolce, M., and Cardone, D. (2001). "Mechanical behaviour of shape memory alloys for seismic applications 2. Austenite NiTi wires subjected to tension." International Journal of Mechanical Sciences, 43(11), pp.2657-2677.
58. MANSIDE. (1998). "Memory alloys for new structural vibrations isolating devices," MANSIDE Third Twelve Monthly Progress Report.
59. DesRoches, R., McCormick, J., Delemont, M. (2004). "Cyclic properties of superelastic shape memory alloy wires and bars." Journal of Structural Engineering, 2004 Jan;130(1):38-46.
60. Tyber, J., McCormick, J., Gall, K., DesRoches, R., Maier, H.J. and Abdel Maksoud, A.E. (2007). "Structural engineering with NiTi. I: basic materials characterization." Journal of Engineering Mechanics, 133(9), 1009-1018.
61. McCormick, J., DesRoches, R., Fugazza, D., and Auricchio, F. (2007). "Seismic assessment of concentrically braced steel frames with shape memory alloy braces." Journal of Structural Engineering, 133(6), 862-70.
62. San Juan, J., and Nó, M. L. (2003). "Damping behavior during martensitic transformation in shape memory alloys." Journal of Alloys and Compounds, 355(1), 65-71.
63. Cai, W., Lu, X. L., and Zhao, L. C. (2005). "Damping behavior of TiNi-based shape memory alloys." Materials Science and Engineering, A, 394(1) 78-82.
64. Chen, Y., Jiang, H. C., Liu, S. W., Rong, L. J., and Zhao X. Q. (2009). "Damping capacity of TiNi-based shape memory alloys." Journal of Alloys and Compounds, 482(1), pp.151-154.
65. McCormick, J., DesRoches, R., Fugazza, D., and Auricchio, F. (2006). "Seismic vibration control using superelastic shape memory alloys." J Eng Mater Technol, 128,294–301.
66. Gong, J. M., Tobushi, H., Takata, K., Okumura, K., and Endo, M. (2002). "Cyclic superelastic deformation of TiNi shape-memory alloy." In Materials Science Forum, 394, 245-248). Trans Tech Publications.

67. Wang, Z. G., Zu, X. T., Dai, J. Y., Fu, P., and Feng, X. D. (2003). “Effect of thermomechanical training temperature on the two-way shape memory effect of TiNi and TiNiCu shape memory alloys springs.” Materials Letters, 57(9), pp.1501-1507.
68. MalÃŠcot, P., Lexcellent, C., FoltÃĒte, E., and Collet, M. (2006). “Shape memory alloys cyclic behavior: experimental study and modeling.” Journal of Engineering Materials and Technology, 128(3), 335-345.
69. Wang, W., Fang, C. and Liu, J. (2016). “Large size superelastic SMA bars: heat treatment strategy, mechanical property and seismic application.” Smart Materials and Structures, 25(7), p.075001.
70. Parulekar, Y. M., Kiran, A. R., Reddy, G. R., Singh, R. K., and Vaze, K. K. (2014). “Shake table tests and analytical simulations of a steel structure with shape memory alloy dampers.” Smart Materials and Structures, 23(12), 125002.
71. Zhang, Y., and Zhu, S. (2007). “A shape memory alloy-based reusable hysteretic damper for seismic hazard mitigation.” Smart Mater. Struct. 16(5), 1603.
72. Dezfuli, F.H., and Alam, M.S. (2013). “Shape memory alloy wire-based smart natural rubber bearing.” Smart Materials and Structures, 22(4), p.045013.
73. Azadi, B., Rajapakse, R. K. N. D., and Maijer, D. M. (2006). “One-dimensional thermomechanical model for dynamic pseudoelastic response of shape memory alloys.” Smart Materials and Structures, 15, 996-1008.
74. Wu, K., Yang, F., Pu, Z., and Shi, J. (1996). “The effect of strain rate on detwinning and superelastic behavior of Ni Ti shape memory alloys.” Journal of intelligent material systems and structures, 7(2), pp.138-144.
75. Wolons, D., Gandhi, F., and Malovrh, B. (1998). “Experimental investigation of the pseudoelastic hysteresis damping characteristics of shape memory alloy wires.” Journal of Intelligent Material Systems and Structures, 9(2), pp.116-126.
76. Ren, W., Li, H., and Song, G. (2007). “A one-dimensional strain-rate-dependent constitutive model for superelastic shape memory alloys.” Smart Materials and Structures, 16(1), p191.
77. Tobushi, Hisaaki, et al. "Influence of strain rate on superelastic properties of TiNi shape memory alloy." Mechanics of Materials 30.2 (1998): 141-150.
78. Chen, W., and Bo, S. (2006). “Temperature dependence of a NiTi shape memory alloy's superelastic behavior at a high strain rate.” Journal of Mechanics of Materials and Structures, 1(2), pp.339-356.
79. Churchill, C.B., Shaw, J.A. and Iadicola, M.A. (2009). “Tips and tricks for characterizing shape memory alloy wire: part 2 - fundamental isothermal responses.” Experimental Techniques, 33(1), pp.51-62.
80. Yin, H., and Sun, Q. (2012). “Temperature variation in NiTi shape memory alloy during cyclic phase transition.” Journal of materials engineering and performance, 21(12), pp.2505-2508.
81. Chang, B. C., Shaw, J. A., and Iadicola, M. A. (2006). “Thermodynamics of shape memory alloy wire: modeling, experiments, and application.” Continuum Mechanics and Thermodynamics, 18(1), 83-118.
82. Leon, R. T., DesRoches, R., Ocel, J., and Hess G. (2001). “Innovative beam column connections using shape memory alloys.” InSPIE's 8th Annual International Symposium on Smart Structures and Materials, 227-237. International Society for Optics and Photonics.
83. Ma, H, Wilkinson T, Cho C. Feasibility study on a self-centering beam-to-column connection by using the superelastic behavior of SMAs. Smart Materials and Structures. 2007 Jul 27; 16(5):1555.
84. Rofooei, F. R., Farhidzadeh, A. (2011). “Investigation on the seismic behavior of steel MRF with shape memory alloy equipped connections.” Procedia Engineering, 14, 3325-30.
85. Sepúlveda, J., Boroschek, R., Herrera, R., Moroni, O., and Sarrazin, M. (2008). “Steel beam–column connection using copper-based shape memory alloy dampers.” Journal of Constructional Steel Research, 64(4), 429-35.

86. Speicher, M. S., DesRoches, R., Leon, R. T. (2011). “Experimental results of a NiTi shape memory alloy (SMA)-based re-centering beam-column connection.” Engineering structures, 33(9), 2448-57.
87. Yam, M. C., Fang, C., Lam, A. C., Zhang, Y. (2015). “Numerical study and practical design of beam-to-column connections with shape memory alloys.” Journal of Constructional Steel Research, 104,177-92.
88. McCormick, J., DesRoches, R., Fugazza, D., and Auricchio, F. (2007). “Seismic assessment of concentrically braced steel frames with shape memory alloy braces.” Journal of Structural Engineering, 133(6), 862-70.
89. Asgarian, B., Moradi, S. (2011). “Seismic response of steel braced frames with shape memory alloy braces.” Journal of Constructional Steel Research, 67(1), 65-74.
90. D. J., Fahnestock, L. A., Eatherton, M. R. (2012). “Development and experimental validation of a nickel–titanium shape memory alloy self-centering buckling-restrained brace.” Engineering Structures, 40, 288-98.
91. Y., Shrestha, K. C., Maekawa, N., Koetaka, Y., Omori, T. and Kainuma, R., (2016). “Shaking table tests of steel frame with superelastic Cu–Al–Mn SMA tension braces.” Earthquake Engineering & Structural Dynamics, 45(2),.297-314.
92. Gao, Nan, et al. "An innovative seismic bracing system based on a superelastic shape memory alloy ring." Smart Materials and Structures 25.5 (2016): 055030.
93. Shi, Fei, Gokhan Saygili, and Osman E. Ozbulut. "Probabilistic seismic performance evaluation of SMA-braced steel frames considering SMA brace failure." Bulletin of Earthquake Engineering 16.12 (2018): 5937-5962.
94. Ozbulut, O. E., and Hurlebaus, S. (2010). “Evaluation of the performance of a sliding-type base isolation system with a NiTi shape memory alloy device considering temperature effects.” Engineering Structures, 32(1), 238-49.
95. Bhuiyan, A. R., Alam, M. S. (2013). “Seismic performance assessment of highway bridges equipped with superelastic shape memory alloy-based laminated rubber isolation bearing.” Engineering structures, 49, 396-407.
96. Gur, S., Mishr, S. K., Chakraborty, S. (2014). “Performance assessment of buildings isolated by shape-memory-alloy rubber bearing: Comparison with elastomeric bearing under near-fault earthquakes.” Structural Control and Health Monitoring, 21(4):449-65.
97. Shinozuka, M., Chaudhuri, S. R., Mishra, S. K. (2015). “Shape-Memory-Alloy supplemented Lead Rubber Bearing (SMA-LRB) for seismic isolation.” Probabilistic Engineering Mechanics, 41, 34-45.
98. Ghodke, S., Jangid, R.S. (2016). “Influence of high austenite stiffness of shape memory alloy on the response of base-isolated benchmark building.” Structural Control and Health Monitoring.
99. Zhang, Y., and Zhu, S. (2007). “A shape memory alloy-based reusable hysteretic damper for seismic hazard mitigation.” Smart Mater. Struct. 16(5), 1603.
100. Zhu, S., and Zhang, Y. (2008). “Seismic analysis of concentrically braced frame systems with self-centering friction damping braces.” Journal of Structural Engineering, 134(1), 121-31.
101. Ma, H., and Cho, C. (2008). “Feasibility study on a superelastic SMA damper with re-centring capability.” Materials Science and Engineering: A., 473(1), 290-6.
102. Qian, H, Li, H, Song, G., Guo, W. (2013). “Re-centering shape memory alloy passive damper for structural vibration control.” Mathematical Problems in Engineering, Nov 28, 2013.
103. Yang, C. S., DesRoches, R., Leon, R. T. (2010). “Design and analysis of braced frames with shape memory alloy and energy-absorbing hybrid devices.” Engineering Structures, 32(2), 498-507.
104. Qian, H., Li, H., and Song, G. (2016). “Experimental investigations of building structure with a superelastic shape memory alloy friction damper subject to seismic loads.” Smart Materials and Structures, 25(12), 125026.

105. Bhowmick, S., Mishra, S. K. (2016). “FNCATB Superelastic damper for seismic vibration mitigation.” Journal of Intelligent Material Systems and Structures, 27(15), 2062-77.
106. Silwal, Baikuntha, Robert J. Michael, and Osman E. Ozbulut. "A superelastic viscous damper for enhanced seismic performance of steel moment frames." Engineering Structures105 (2015): 152-164.
107. Alam, M.S., Youssef, M.A. and Nehdi, M. Utilizing shape memory alloys to enhance the performance and safety of civil infrastructure: a review. Canadian Journal of Civil Engineering 2007; 34 (9): 1075-1086.
108. Cortés-Puentes WL, Palermo D. SMA tension brace for retrofitting concrete shear walls. Engineering Structures 2017; 140:177-88. 3.
109. Ozbulut OE, Silwal B. Performance assessment of buildings isolated with S-FBI system under near-fault earthquakes. Smart Structures and Systems 2016;17(5):709-24. 4.
110. Speicher MS, DesRoches R, Leon RT. Investigation of an articulated quadrilateral bracing system utilizing shape memory alloys. Journal of Constructional Steel Research 2017; 130:65-78.
111. Liang, X., et al., Thermal cycling stability and two-way shape memory effect of Ni–Cu–Ti–Hf alloys. Solid state communications, 2001. 119(6): p. 381-385. [31]
112. Meng, X.L., et al., Martensite structure in Ti–Ni–Hf–Cu quaternary alloy ribbons containing (Ti,Hf)2Ni precipitates. Acta Materialia, 2010. 58(10): p. 3751-3763.
113. Karaca, H., et al., Effects of aging on [111] oriented NiTiHfPd single crystals under compression. Scripta Materialia, 2012. 67(7): p. 728-731
114. Saedi, S., et al., The influence of heat treatment on the thermomechanical response of Ni-rich NiTi alloys manufactured by selective laser melting. Journal of Alloys and Compounds, 2016. 677: p. 204-210.
115. OpenSees. Open System for Earthquake Engineering Simulation - Home Page. April 1, 2014, http://OpenSees. berkeley.edu/.
116. Lignos, Dimitrios G., Helmut Krawinkler, and Andrew S. Whittaker. "Collapse assessment of a 4-story steel moment resisting frame." Proceedings of COMPDYN 2009: ECCOMAS Thematic Conference on Computational Methods in Structural Dynamics and Earthquake Engineering. 2009.
117. Lignos, D.G. and Krawinkler, H. Sidesway collapse of deteriorating structural systems under seismic excitations, Rep.No.TB 177. The John A. Blume Earthquake Engineering Research Center. Stanford University: CA, 2012.
118. FEMA P695. Quantification of Building Seismic Performance Factors. Washington, D.C: Federal Emergency Management Agency, 2009.
119. Ibarra, Luis F., Ricardo A. Medina, and Helmut Krawinkler. "Hysteretic models that incorporate strength and stiffness deterioration." Earthquake engineering & structural dynamics34.12 (2005): 1489-1511.
120. ASCE. “Seismic Rehabilitation of Existing Buildings (41-13).” American Society of Civil Engineers, Reston VA.
121. ASCE. “Minimum Design Loads for Buildings and Other Structures.” ASCE 7-10. American Society of Civil Engineers, Reston, Virginia.
122. AISC Committee (2010). “Specification for Structural Steel Buildings (ANSI/AISC 360-10.” American Institute of Steel Construction, Chicago-Illinois.
123. FEMA. (2000). “State of the Art Report on Systems Performance of Steel Moment Frames Subject to Earthquake Ground Shaking (FEMA 355C).” Federal Emergency Management Agency, Washington DC.
124. AXTON Railway Components (www.axtone.eu).
125. FEMA, P-751. 2009. “NEHRP recommended seismic provisions: design examples.” Federal Emergency Management Agency, Washington, DC; 2012.
126. SAC Joint Venture (Ed.), State of the Art Report on Systems Performance of Steel Moment Frames Subject to Earthquake Ground Shaking, 2000.

127. L.F. Ibarra, R.A. Medina, H. Krawinkler, Hysteretic models that incorporate strength and stiffness deterioration, Int. J. Earthq. Eng. Struct. Dyn. 34 (12) (2005) 1489–1511.
128. D.G. Lignos, H. Krawinkler, A Database in Support of Modeling of Component Deterioration for Collapse Prediction of Steel Frame Structures, Proc. ASCE Structures Congress, Long Beach, California, May 18–20; 2007.
129. A. Gupta, H. Krawinkler, Seismic demands for performance evaluation of steel moment resisting frame structures, Technical Report 132, The John A. Blume Earthquake Engineering Research Center, Department of Civil Engineering, Stanford University, Stanford, CA, 1999.
130. PEER NGA database, The Pacific Earthquake Engineering Research Center, http:// ngawest2.berkeley.eduPacific Earthquake Engineering Research Center (PEER), 2014.
131. Filiatrault, André, Robert Tremblay, and Ramapada Kar. "Performance evaluation of friction spring seismic damper." *Journal of Structural Engineering* 126.4 (2000): 491-499.